First-Principles Multiscale Investigation of Structural and Chemical Defects in Metals

A dissertation presented

by

Georg Schusteritsch

to

The School of Engineering and Applied Sciences

in partial fulfillment of the requirements

for the degree of

Doctor of Philosophy

in the subject of

Applied Physics

Harvard University

Cambridge, Massachusetts

September 2012

Thesis advisor

Efthimios Kaxiras

Author

Georg Schusteritsch

First-Principles Multiscale Investigation of Structural and Chemical Defects in Metals

Abstract

This thesis explores multiscale approaches to describe structural and chemical defects in metals. Particular emphasis is placed on investigating processes involving grain boundaries (GBs) in combination with impurity and vacancy defects. The defects and their interactions are calculated to very high accuracy using density functional theory (DFT) and connected to the macroscopic behavior within the two multiscale formalisms presented here.

We begin with a sequential approach to address chemical embrittlement of nickel by sulfur impurities. Effects at both a $\Sigma 5\,(012)$ symmetric tilt GB and in the bulk are studied by considering competing mechanisms for ductile and brittle behavior. For the bulk, this takes the form of Rice's theory, where the ratio of the surface and unstable stacking energy is used as a measure of ductility. This is generalized to the GB by considering GB sliding (GBS) and intergranular decohesion. Clear evidence that chemical embrittlement of nickel by sulfur is a GB driven effect is found.

Next, the concurrent multiscale approach is described. A small region, containing

the defects, is treated with Kohn-Sham DFT and coupled to the bulk, described with the embedded atom method. We apply this novel method to elucidate the chemical embrittlement of a copper $\Sigma5\,(012)$ symmetric tilt GB. Intergranular decohesion for three substitutional impurities, bismuth, lead and silver, is investigated by considering the work of separation (W_s) and the tensile strength (σ_t). Bismuth and lead show a significant decrease in W_s and σ_t, consistent with embrittlement, whilst silver has only a minor effect.

Then, the concurrent multiscale method is applied to the process of GBS in copper. It is found that the resistance against sliding increases significantly for bismuth, lead and silver impurities. The underlying mechanisms for this increase are found to be dominated by mechanical effects for bismuth and lead. For silver chemical effects are of greater importance. Similar results are found for the underlying mechanisms of intergranular decohesion.

The effect of a mono-vacancy on GBS is studied for copper. The multiscale approach enables improved decoupling of the mono-vacancy. It is found that the mono-vacancy enhances GBS by 22%.

Contents

List of Figures

List of Tables

Citations to Previously Published Work

Chapter 3 has been published as the following paper:

> "Sulfur induced embrittlement of nickel: a first principles study", Georg Schusteritsch and Efthimios Kaxiras, Modelling Simul. Mater. Sci. Eng. **20** 065007 (2012)

Chapter 4 appears as the following paper:

> "An ab-initio multiscale method for modeling chemical embrittlement of metals", Georg Schusteritsch, Thomas D. Kühne, Z. Xiao Guo and Efthimios Kaxiras, submitted to Phys. Rev. B.

Dedicated to my wife Hsiang-Han

Chapter 1

Introduction

There is no doubt that over the last few decades computational methods, and in particular atomistics approaches, have become of great importance in understanding the underlying physics of many materials systems. Important contributions have been made by computational research both in the context of supplementing experimental work in its understanding but also as predictive approaches in their own right. The latter is particularly relevant to the many systems that are inherently difficult or impossible, or simply too expensive to be treated experimentally. Of all computational approaches, density functional theory (DFT), with its beginning in the 1960's by the work of Hohenberg, Kohn and Sham [1, 2], takes a special place. It is a first-principles or *ab-initio* method, meaning that it is purely based on the fundamental laws of physics, rather than being an empirical model that requires fitting or other input in the form of assumptions of the system. This lends the approach a particular beauty

from a physics perspective. At the same time, from a practical point of view DFT has established itself as a successful method in the form of several excellent software packages such as CP2K [3], VASP [4] and Siesta [5], to name but a few. These are now routinely used by many researchers worldwide.

One of the challenges researchers in the field of DFT face is the large computational cost associated with performing realistic calculations. Although the computational power and resources available have steadily increased since its introduction almost 50 years ago, DFT is realistically limited to hundreds of atoms for most applications. This can sometimes limit the conclusions that can be drawn about the macroscopic behavior of materials. Increasing the system sizes that are possible to be addressed is an area of ongoing research and one possible approach are multiscale methods [6, 7, 8, 9, 10, 11, 12]. In general, multiscale methods can be split into sequential and concurrent approaches. In the former the link to the macroscopic behavior is made after performing DFT calculations. This often takes the form of using DFT to determine important quantities for continuum methods. In the latter the DFT region is concurrently coupled to a more macroscopic model, allowing an increase of the system size thereby capturing the long-range physics. There is a clear need to further develop first-principles based multiscale methods to efficiently treat many long-range systems in materials science and physics. A major part of this thesis tries to address this issue. Both types of multiscale approaches will be explored and used in this work, with a particular emphasis on the concurrent multiscale scheme and

its applications. The specific problem we address in this work within the multiscale formalism is the mechanical behavior of metals and the effect different defects can have. These are to a large extent multiscale problems, making a treatment that can account for different length-scales important.

From a practical point of view, metals are one of the oldest yet still one of the most important materials for technologies. Metals have been used and studied from the beginning of human-kind and their use is still ubiquitous in modern-day technologies. It is reasonable to say that virtually any modern industry and technology relies in some way or another on metals, ranging from the transport industry, to production industry, to the high-tech industry. A deep understanding of the physical and mechanical properties of metals is crucial, both in terms of the potential financial cost involved and in the case of material failure the cost of human life.

The properties and behavior of metals, and for that matter materials in general, are to a large extent determined by the defects they contain. To understand the mechanical behavior of metals, defects and defect interactions have to be studied. Which particular type of defect is of greatest importance strongly depends on the particular system and phenomenon that is being addressed. In this work, we will concentrate on grain boundaries and how other defects such as impurities and vacancies can interact with grain boundaries and thereby change the overall mechanical behavior.

Grain boundaries play an important role in metals. It is for instance believed that some impurities segregate to grain boundaries [13], weaken the cohesion of the grain

boundary (GB) and result in brittle intergranular fracture. This process of chemical embrittlement has been known for over a hundred years in some metals [14], but the underlying mechanisms responsible for this phenomenon are still under investigation. Another process of importance is that of grain boundary sliding (GBS). This is known to be of importance for high temperature flow in metals [15, 16, 17]. More recently, the influence of grain boundaries has also received attention in the context of nanocrystalline metals [19, 20, 21, 22, 23, 24]. The small grain sizes in nanocrystalline metals result in a high number of grain boundaries in comparison to the volume of the grains and different deformation mechanisms involving the grain boundaries more directly are thought to become more dominant. This is in contrast to coarse-grained metals for which grain boundaries are traditionally viewed as static barriers to dislocation motion. Although nanocrystalline metals have been proposed already in the late 1980's by Gleiter [18], the mechanisms involved in their deformation are to date not fully understood. Recent molecular dynamics simulations suggest that GBS plays an important role as a plastic deformation mechanism [19, 20, 21, 22, 23, 24]. The study of grain boundaries and gaining a deeper understanding of the physics of particular types of grain boundaries has increased in importance in the context of grain boundary engineering (GBE). This technique was proposed to improve the mechanical properties of metals [25] and has seen renewed interest in recent years [26]. GBE allows for fabricating different types of grain boundaries, including special grain boundaries, often with the aim of enhancing the resistance against corrosion, cracking

or embrittlement. A deeper insight of the atomistic processes of grain boundaries can help in guiding experiments.

The particular metals that will be considered here are nickel (Ni) and copper (Cu), both metals of great importance in industry. Ni is for instance used in the aeronautics industry and oil and gas industry, mostly because of its excellent high temperature properties. Cu is also found in many technologies, most recently in particular in the high-tech industry, where it is now the metal of choice for interconnects in state of the art intergrated circuits. In principle, grain boundaries in such metal systems can be described with empirical models and there are several excellent embedded atom method (EAM) studies dealing with Ni and Cu [19, 20, 27]. These studies exclusively deal with pure metal systems. A treatment of a system with impurities based on empirical models has several complications associated with it. First, there is the issue of reliability. Although several very good potentials for pure metals exist, implementing interactions with other elements is first of all more complicated and also gives less reliable results. The more important point from a practical point of view is that every new impurity needs a new potential. This is therefore an issue of transferability and versatility. Basing the impurities on quantum mechanics in the form of DFT, circumvents both these issues. At the same time, the multiscale approach can capture the long-range description that may otherwise be lost. The aim here is therefore to investigate and establish multiscale approaches in the field of defects.

Structure of this thesis

Chapter 2 provides an overview of the relevant theoretical background for DFT and the EAM. Two different implementations of DFT will be employed in this work. The methodology and theoretical basis for both will be discussed and differences in the approaches will be highlighted.

In chapter 3 the effect of sulfur impurities on the mechanical properties of Ni will be studied in the context of a sequential multiscale method. This will be treated both in the context of coarse-grained materials and nanocrystalline materials. The decohesion energy and unstable stacking energy will be calculated for bulk Ni and compared to the decohesion and shear behavior of Ni with a GB. The influence of the S impurities will be assessed. Ideas from Rice's theory of dislocation nucleation are employed and generalized for GB shear in the form of a ductility parameter describing the competition between GBS and intergranular decohesion. We find clear evidence that chemical embrittlement of Ni by S is a GB driven effect.

In chapter 4 the concurrent multiscale method will be introduced and described. The methodology of how coupling between the DFT and EAM region is achieved will be discussed in detail. This also includes several test calculations for Ni and Cu showing evidence of the validity of the method. A $\Sigma 5\,(012)$ symmetrical tilt GB in Cu is being studied and the behavior of the strain field surrounding it is being investigated with and without impurities. Evidence for embrittlement in the form of a decrease of the work of separation for bismuth (Bi) and lead (Pb) impurities is

found. The tensile strength of the Cu GB is also investigated and found to decrease as well, giving rise to enhanced crack initiation. As a comparison silver (Ag) impurities are considered; they have little effect on the decohesion properties of the Cu GB.

Chapter 5 extends the application of chapter 4 by including shear effects in the form of GBS for the Cu GB. We find that the energy barrier for GBS increases significantly for Bi, Pb and Ag inclusion at the GB. This implies that plastic deformation in the form of GBS is suppressed. The particular underlying physical mechanisms for the changes in the GBS energy landscape are being investigated and found to differ for Bi and Pb in comparison to Ag. The latter has strong chemical interactions, whereas the former two are dominated by mechanical size effects. The underlying mechanisms for the changes in the work of separation of chapter 4 are being investigated in the same manner. Again, Bi and Pb have a strong size effect component associated with their decohesion behavior, whereas chemical interactions become very important for Ag.

Chapter 6 deals with the interactions of the Cu GB and vacancies. The vacancy formation energy in the vicinity of the GB is investigated and the effect they have on GBS is studied in detail. This work takes advantage of the large supercells we are able to employ within our multiscale approach, allowing us to appropriately decouple the vacancy from its periodic images. Traditionally small supercells have been used for other first-principles studies, leading to effective vacancy lines or vacancies separated by only a very small distance. It is found that GBS is enhanced by a mono-vacancy.

Chapter 2

Computational method and theoretical background

2.1 Overview

This chapter gives a general overview of the relevant theoretical background for the work presented in this thesis. The chapter begins in section 2.2.1 with a discussion of the many-body Schrödinger equation and the complications involved in finding a solution for any but the simplest systems. This is followed by a discussion of the initial approaches to the many-body Schrödinger equation in the form of the Hartree and Hartree-Fock approximation in section 2.2.2. This leads to the density functional theory, as proposed in a series of seminal papers by Hohenberg, Kohn and Sham [1, 2]. All aspects necessary to understand modern day density functional

theory will be discussed in the remainder of section 2.2. Particular emphasis will be given to the implementations of DFT used throughout this work. As discussed in chapter 1, two different approaches will be taken in the context of multiscale modeling of materials. In chapter 3 we employ a combination of DFT calculations with results from continuum theory in the context of sequential multiscale modeling. The DFT calculations are performed using the Vienna *Ab-initio* Simulation Package (VASP) [4], an implementation based on a plane wave (PW) basis. This type of basis will be discussed in section 2.2.6. The particular calculations of chapter 3 use the generalized gradient approximation (GGA) [28] with projector-augmented plane wave (PAW) potentials [29], covered in sections 2.2.4 and 2.2.5, respectively.

In chapters 4, 5 and 6 a concurrent multiscale method is presented and used that couples DFT to the embedded atom method (EAM). This method was chosen to be implemented using CP2K [3], a suite of programs employing Quickstep (QS) to perform DFT calculations. QS employs a Gaussian Plane Wave (GPW) basis, a combination of the PW approach described in section 2.2.6 and the Gaussian-type orbital (GTO) approach described in section 2.2.6; this mixed basis will be introduced in section 2.2.6. The calculations using CP2K will be based on separable and norm-conserving pseudopotentials by Goedecker-Teter-Hutter (GTH) [30, 31]; this will be reviewed in section 2.2.5 and contrasted to the PAW method. The necessary fundamentals for the embedded atom method (EAM) will be introduced in section 2.3 to give a complete overview of the theoretical basis for the concurrent multiscale method.

2.2 Density Functional Theory

2.2.1 The many-body Schrödinger equation

A full quantum mechanical treatment of the electrons and the nuclei of a piece of matter would involve solving the time independent Schrödinger equation,

$$H\Psi\left(\{\mathbf{R}_I;\mathbf{r}_i\}\right) = E\Psi\left(\{\mathbf{R}_I;\mathbf{r}_i\}\right), \tag{2.1}$$

with the Hamiltonian given by

$$\begin{aligned} H = & -\sum_I \frac{\hbar^2}{2M_I}\nabla_I^2 - \sum_i \frac{\hbar^2}{2m_e}\nabla_i^2 + \frac{e^2}{2}\sum_I \sum_{J(J\neq I)} \frac{Z_I Z_J}{|\mathbf{R}_I - \mathbf{R}_J|} \\ & + \frac{e^2}{2}\sum_i \sum_{j(j\neq i)} \frac{1}{|\mathbf{r}_i - \mathbf{r}_j|} + e^2 \sum_I \sum_i \frac{Z_I}{|\mathbf{R}_I - \mathbf{r}_i|}, \end{aligned} \tag{2.2}$$

where $\{\mathbf{R}_I\}$ are the set of nuclear coordinates, $\{\mathbf{r}_i\}$ is the set of coordinates of the electrons, M_I the mass of the nuclei, m_e the mass of an electron, Z_I the nuclear charge, e the charge of an electron and $\hbar$ given Planck's constant is $\hbar = h/2\pi$. The five different terms in eq. 2.2 correspond to the following physical quantities and interactions: the first and second term are the kinetic energy operators for the nuclei and electrons, respectively. This is followed by the potential energy interaction of individually the ionic system and the electrons in terms three and four, respectively. Finally, the last term is the interaction energy between the electrons and the ions. In its most general form as given in eq. 2.1, the full many-body Schrödinger equation involves all interactions of electrons and nuclei. To make headway in finding a solution, at this point it is useful to notice that the motion of electrons and nuclei

occur on a very different time-scale, with the nuclei being much slower. The mass of an electron is significantly smaller than the mass of a typical nuclei considered in this work. Taking this into consideration, it is possible to make the approximation that the wavefunction Ψ is dependent only on the electronic degrees of freedom and the nuclei are treated classically. This is known as the Born-Oppenheimer approximation [32, 33]. This approximation amounts to the assumption that the electrons remain in a given state while they instantaneously follow the motion of the nuclei. Within the Born-Oppenheimer approximation the velocities and the history of the nuclei hence have no effect on the total energy.

2.2.2 Hartree and Hartree-Fock approximation

Despite the significant simplification provided by the Born-Oppenheimer approximation, finding solutions of the full many-body Schrödinger equation of the electrons is still a formidable challenge. A solution exists only for a few special cases, and even then only numerical approaches tend to exist. The main problem that has to be overcome is the many-body nature of the hamiltonian. This clearly has to be addressed with further approximations. One such approximation was proposed early on by Hartree in 1928 [34]. This approach involves treating the electrons as independent particles and taking the Ansatz for the many-body wavefunction as a product of one electron wavefunctions ϕ_i,

$$\Psi^H\left(\{\mathbf{r}_i\}\right) = \prod_i^N \phi_i\left(\mathbf{r}_i\right). \tag{2.3}$$

By employing the method of Lagrange multipliers one can then show that the Hartree single-particle equation takes the form,

$$\left[-\frac{\hbar^2\nabla_r^2}{2m_e} + V_{ion}\left(\mathbf{r}\right) + e^2\sum_{j\neq i}\langle\phi_j\left|\frac{1}{|\mathbf{r}-\mathbf{r}'|}\right|\phi_j\rangle\right]\phi_i\left(\mathbf{r}\right) = \epsilon_i\phi_i\left(\mathbf{r}\right). \tag{2.4}$$

The Hartree term,

$$V^H = e^2\sum_{j\neq i}\langle\phi_j\left|\frac{1}{|\mathbf{r}-\mathbf{r}'|}\right|\phi_j\rangle. \tag{2.5}$$

only includes the repulsive Coulomb interactions of the electrons. The Hartree equation can be solved iteratively, that is assuming a given initial set of $\{|\phi_i\rangle\}$, the density ρ and hence the hamiltonian can be calculated, which in turn gives a new set of $\{|\phi_i\rangle\}$. Based on this new set of wavefunctions, usually determined by combining it with the old input wavefunctions, yet a new set of $\{|\phi_i\rangle\}$ can be constructed. This is iterated until the output equals the input, up to some accuracy. This self-consistency approach will be of importance for later methods as well. Although eq. 2.3 is numerically solvable, there are significant issues with the Hartree approximation. These can be traced to the inappropriate Ansatz in eq. 2.3, namely that the wavefunction neglects any exchange effects. The electrons, being fermions, have to satisfy Pauli's principle and hence under exchange the wavefunction has to change sign. This is not satisfied by the Hartree approximation but can be addressed by ensuring that the Ansatz taken leads to an antisymmetric wavefunction. This is the basis of the Hartree-Fock approximation [35, 36], where now the Ansatz for the wavefunction takes the form of a

Slater determinant,

$$\Psi^{HF}\left(\{\mathbf{r}_i\}\right) = \frac{1}{\sqrt{N!}} \begin{vmatrix} \phi_1\left(\mathbf{r}_1\right) & \phi_1\left(\mathbf{r}_2\right) & \dots & \phi_1\left(\mathbf{r}_N\right) \\ \phi_2\left(\mathbf{r}_1\right) & \phi_2\left(\mathbf{r}_2\right) & \dots & \phi_2\left(\mathbf{r}_N\right) \\ \vdots & \vdots & \vdots & \vdots \\ \phi_N\left(\mathbf{r}_1\right) & \phi_N\left(\mathbf{r}_2\right) & \dots & \phi_N\left(\mathbf{r}_N\right) \end{vmatrix}. \tag{2.6}$$

This ensures that on exchange of two electrons the wavefunction behaves appropriately. By variational treatment, this leads to the single-particle Hartree-Fock equations of the form,

$$\left[-\frac{\hbar^2\nabla_r^2}{2m_e} + V_{ion}\left(\mathbf{r}\right) + V_i^H\left(\mathbf{r}\right) + V_i^X\left(\mathbf{r}\right)\right]\phi_i\left(\mathbf{r}\right) = \epsilon_i\phi_i\left(\mathbf{r}\right), \tag{2.7}$$

which again can be solved iteratively. In comparison to the Hartree approximation, this was a major step forward, as it adds the exchange term,

$$V_i^X\left(\mathbf{r}\right) = -e^2\int \frac{\sum_{j\neq i}\frac{\phi_i(\mathbf{r}')\phi_i^*(\mathbf{r})\phi_j(\mathbf{r})\phi_j^*(\mathbf{r}')}{\phi_i(\mathbf{r})\phi_i^*(\mathbf{r})}}{\left|\mathbf{r}-\mathbf{r}'\right|}. \tag{2.8}$$

Although this method improves the Hartree approximation, it still leaves the problem of including correlations between electrons unresolved.

2.2.3 Modern density functional theory

Density functional theory tries to approach the problem of the many-body Schrödinger equation in a different manner altogether. Whereas for the Hartree and Hartree-Fock approximation, the approach is to try to get an approximate expression of the many-body wavefunction, the main underlying idea of DFT is that any property of the

interacting system can be solely described by its ground state density. Thus the difficulty of finding a very complicated many-body wavefunction to the Schrödinger equation is altogether circumvented.

The main underlying ideas of DFT were proposed as early as in 1927 and 1928 by Thomas [37] and Fermi [38], later extended by Dirac [39, 40] in 1930. In their theory, they intuitively formulated the functional relationship between the energy and the ground state density. They proposed functionals for each term of the Schrödinger equation, neglecting correlations, and then used the density of the uniform electron gas of non-interacting electrons. This clearly simplifies the many-body Schödinger equation tremendously in comparison to the approaches taken in the previous sections. However, the approximations for the functionals turn out to be too crude and are therefore not able to give accurate enough results for most systems.

The major breakthrough came with the ground-breaking work of Hohenberg and Kohn [1] in 1964 and the work by Kohn and Sham [2] in 1965. The work by Hohenberg and Kohn rigorously established the functional relationship between the density and energy in what is now known as the Hohenberg-Kohn theorems. The work by Kohn-Sham was equally important in that it allowed for practical calculations. Both will be outlined briefly in what follows.

Hohenberg-Kohn theorems

A more complete discussion including the proofs of the Hohenberg-Kohn theorems can be found in any number of books on DFT ([41, 42, 43, 44]) and is only summarized as follows:

Theorem 1: For any system of interacting particles, the ground state particle density $n(\mathbf{r})$ uniquely determines the external potential V, apart from a constant. A uniquely determined external potential in turn implies that the Hamiltonian and hence the set of ground state wavefunctions are determined, meaning that the ground state density uniquely determines all properties of the system.

Theorem 2: Based on the previous theorem, the energy can now be defined to be a universal functional of the ground state density. Minimizing this functional for a given external potential then gives the ground state energy. The associated density at the minimum gives the ground state density.

Although, the work by Hohenberg and Kohn rigorously proofed the intuitive assumptions of Thomas and Fermi and as such lay the ground-works for modern-day DFT, it made no attempt at formulating the exact functional form of the energies. Although the problem of having to find the full many-body wavefunctions has been circumvented it seems at first glance that no headway was made, as the exact functional form of the energy is not known. This was addressed by Kohn and Sham.

Kohn-Sham equations

The approach taken by Kohn and Sham is to introduce a fictitious reference system that consists of non-interacting electrons, with the condition that this system has to have the same ground state density as the system of interacting electrons we are trying to solve. The second part of their Ansatz is that the reference Hamiltonian is to have the usual kinetic operator and an effective local potential V_{KS}. An essential ingredient in their treatment is that the orbital wavefunctions are (re-)introduced. This allows for exact evaluation of the kinetic energy term, which does not explicitly depend on the density. To be precise the specific form of the wavefunctions of the fictitious electrons are that of the Slater determinants introduced earlier for the HF approximation (eq. 2.6). Within the Kohn-Sham Ansatz it is then possible to write the ground state energy functional as,

$$E_{KS} = T_s[n] + \int \mathrm{d}\mathbf{r} V_{ext}(\mathbf{r})\, n(\mathbf{r}) + E_{Hartree}[n] + E_{II} + E_{xc}[n], \tag{2.9}$$

where the independent particle kinetic energy is given by,

$$T_s[n] = -\frac{\hbar^2}{m}\sum_{i=1}^{N_s}\langle\phi_i\left|\nabla^2\right|\phi_i\rangle. \tag{2.10}$$

The Hartree energy is given by

$$E_{Hartree}[n] = \frac{1}{2}\int \mathrm{d}^3r\mathrm{d}^3r' \frac{n(\mathbf{r})\, n(\mathbf{r}')}{|\mathbf{r}-\mathbf{r}'|}. \tag{2.11}$$

E_{II} is the energy due to the interacting nuclei, which can be evaluated using the Ewald method, and V_{ext} is the external potential due to the nuclei. Finally, E_{xc}

includes all the many-body effects that were neglected for the fictitious system. This can be realized by comparing to the interacting system,

$$E_{xc}[n] = \langle T \rangle - T_s[n] + \langle V_{int} \rangle - E_{Hartree}[n], \tag{2.12}$$

where $\langle T \rangle$ and $\langle V_{int} \rangle$ are the kinetic and interaction energies of the interacting system. The 'mistake' one makes by assuming non-interacting particles for the kinetic term, is essentially added to the other interactions into the correlation term. If the functional $E_{xc}[n]$ was known, then one could easily calculate the ground state energy. However, this universal functional is not known and has to be approximated. To proceed in finding a solution to the many-body Schrödinger equation by employing the Kohn-Shan Ansatz it is therefore necessary to find the Kohn-Sham Schrödinger-like equations via variational treatment of the Kohn-Sham energy functional. This gives,

$$(H_{KS} - \epsilon_i)\,\phi_i(\mathbf{r}) = 0, \tag{2.13}$$

where the Hamiltonian is given by,

$$H_{KS} = -\frac{1}{2}\nabla^2 + V_{KS}(\mathbf{r}). \tag{2.14}$$

with,

$$V_{KS} = V_{ext}(\mathbf{r}) + V_{Hartree}(\mathbf{r}) + \frac{\delta E_{xc}}{\delta n(\mathbf{r})}. \tag{2.15}$$

Up to this point no approximations have been made and the equations are exact.

2.2.4 Exchange Correlation Potential

For practical calculations one has to approximate the exchange-correlation functional $E_{xc}[n]$. Since most long-range effects are already in the kinetic and Hartree terms above, it is reasonable to assume a local approximation, where one can then write,

$$E_{xc}[n] = \int \mathrm{d}\mathbf{r} n(r)\, \epsilon_{xc}([n], \mathbf{r}). \tag{2.16}$$

This becomes the basis for the local density approximation and its extension the generalized gradient approximation.

Local density approximation

In order to proceed in the discussion of the LDA it is helpful to consider that the exchange correlation in eq. 2.16 can be split up into two separate parts for the exchange and the correlation energy,

$$E_{xc}[n] = E_X[n] + E_C[n]. \tag{2.17}$$

In principle the exchange part is known exactly as a function of single-electron orbitals, but these calculations are exceedingly expensive. In addition, the functional of the correlation energy is impossible to determine exactly, and it was found that it is beneficial to treat the exchange and correlation part to the same level of approximation. If this is not done, beneficial cancelation terms do not naturally evolve. The next step in finding an approximate expression for the exchange correlation energy

is to consider the results from the homogeneous electron gas. Since eq. 2.16 already assumes only a local dependence, it is logical to use the homogeneous electron gas. This should give good results for any system that does not have a density that is too inhomogeneous. The exchange part is known exactly from the extension of the Thomas-Fermi theory by Dirac [39, 40],

$$\epsilon_x[n] = -\frac{3}{4}\left(\frac{3}{\pi}\rho\right)^{\frac{1}{3}} = -\frac{3}{4}\left(\frac{9}{4\pi^2}\right)^{\frac{1}{3}}\frac{1}{r_s}, \tag{2.18}$$

where $r_s = \left(\frac{3}{4}\pi\rho\right)^{\frac{1}{3}}$ is the Wigner-Seitz radius defining the mean interelectronic distance.

The correlation energy for the homogeneous electron gas cannot be determined exactly. However, it was shown that very accurate Quantum Monte Carlo (QMC) calculations of the homogeneous electron gas can be used instead [45, 46]. A popular parametrization used for instance in VASP is that by Perdew and Zunger [46] based on the QMC calculations by Ceperley and Alder [45], which for a spin unpolarized system takes the form,

$$\epsilon_c[n] = \begin{cases} 0.0311\ln r_s - 0.048 + 0.0020 r_s - 0.0116 r_s, & r_s \leq 1 \\ -0.1423/\left(1 + 1.0529\sqrt{r_s} + 0.3334 r_s\right) & r_s > 1. \end{cases} \tag{2.19}$$

Spin polarized systems are parametrized in the same way resulting in a relation which takes the same form but has different parameter values [46].

Despite the approximations involved in the LDA, it performs remarkably well. Not surprisingly the best correspondence with experiments can be found for systems

that are highly homogeneous, such as metals. Insulators and semiconductors are also described well. The reason why the LDA works so surprisingly well is that the exchange correlation hole fulfills all the sum rules and that for accurate results the exact shape of the exchange correlation hole is not required, only its average is of importance. In general one finds that the LDA tends to overestimate the cohesive or binding energies. As a results it tends to underestimate bond lengths and overestimate the bulk modulus. One main source of errors comes from the fact that in the LDA the self-interaction energy does not cancel completely due to the locality approximation. This can result in large error in strongly localized states. In general since the main approximation for the LDA is that we assume a local behavior that can be well described by the uniform electron gas, we cannot expect it to work that well for molecules and for surfaces as these have density distributions that involve areas of significant inhomogeneity.

Generalized gradient approximation

The generalized gradient approximation aims to address the short-comings of the LDA of not being able to appropriately treat highly inhomogeneous system. This is achieved by including terms of both the density and its gradient into the exchange correlation energy functional,

$$E_{xc}^{GGA}[n] = \int \mathrm{d}r^3 n(r)\, \epsilon_{xc}(n, |\nabla n|)\,. \tag{2.20}$$

Initial extensions of the LDA suffered from the problem that the exchange hole was not described correctly. This has been addressed in several different functional forms for the GGA [47, 48, 49, 28]. All of these have in common that the behavior for the exchange hole is appropriate as was the case for the LDA. This means that the exchange hole has to be normalized to -1 and is negative definite. The particular GGA functional used both for the calculations presented in Chapter 3 with VASP and those presented in chapters 4, 5 and 6 with CP2K are performed using the form of Perdew, Burke and Erznerhof (PBE) [28]. This particular approach will be outlined here for completeness with the relevant publications cited for further information. As for the LDA, the correlation and exchange energy functionals are considered separately. The correlation energy takes the form,

$$E_c^{GGA}\left[n^{\uparrow}, n^{\downarrow}\right] = \int \mathrm{d}r^3 n\left(r\right)\left[\epsilon_c^{\text{unif.}}\left(r_s,\zeta\right) + H\left(r_s,\zeta,t\right)\right]. \tag{2.21}$$

By considering the relevant limiting cases of the density PBE proposed the Ansatz,

$$H = \left(\frac{e^2}{a_0}\right)\gamma\phi^3 \ln\left\{1 + \frac{\beta}{\gamma}t^2\left[\frac{1+At^2}{1+At^2+A^2t^4}\right]\right\}, \tag{2.22}$$

where,

$$A = \frac{\beta}{\gamma}\left[\exp\left\{-\epsilon_c^{\text{unif.}}/\left(\gamma\phi^3 e^2/a_0\right)\right\} - 1\right]^{-1}, \tag{2.23}$$

and $\zeta = \left(n^{\uparrow} - n^{\downarrow}\right)/n$ is the relative spin polarization and t is proportional to the density gradient (a detailed description of each parameter can be found in the original work by PBE [28]). The exchange term for GGA functionals is usually defined by,

$$E_x^{GGA} = \int \mathrm{d}r^3 n\left(r\right)\epsilon_x^{\text{unif.}}\left(n\right)F_x\left(s\right). \tag{2.24}$$

For the particular form of the exchange energy density term PBE take a functional of the same form as Becke [50],

$$F_x(s) = 1 + \kappa - \kappa / \left(1 + \mu s^2/\kappa\right), \tag{2.25}$$

where $\kappa = 0.804$ and β is chosen to take the same value as for the correlation.

2.2.5 Pseudopotentials and Projector Augmented Waves

The previous sections have shown that DFT can be an alternative to attempting to find direct solutions of the full many-body Schrödinger equation. Although more feasible, finding solutions within the DFT formalism can still be very computationally intensive and further approximations are frequently used to improve the efficiency of practical calculations. Pseudopotentials fall within this category of addressing the efficiency of calculations and therefore the feasibility of being able to study practical systems. The underlying simplification of pseudopotentials is based on the realization that not all electrons are of equal importance when only chemical bonding of atoms is considered. It is primarily the valence electrons that are involved in bond formation and it is therefore often not necessary to treat the core electrons explicitly. Very good results can be obtained by employing pseudopotentials where the core electrons only provide an effective potential and are not explicitly treated in the Kohn-Sham equations. On top of the clear advantage of treating less electrons explicitly in the Kohn-Sham equations, the pseudopotential method offers the advantage that the effective potentials can be constructed to be smoother than originally. This if of

great importance when a plane wave basis is employed as this allows for a description of the states with a smaller energy cutoff (this will be discussed in more detailed in section 2.2.6). The theory of pseudopotentials was established in work by Phillips and Kleinman [51]. They propose a smooth nodeless wavefunction, $\tilde{\phi}_v$ for valence states to take the form,

$$\left|\tilde{\phi}_v\right\rangle = |\phi_v\rangle + \sum_c \alpha_{cv} |\phi_c\rangle \,, \tag{2.26}$$

where $\alpha_{cv} = \left\langle \phi_c \middle| \tilde{\phi}_c \right\rangle$. The wavefunctions ϕ_i are the original wavefunctions and satisfy $H|\phi_i\rangle = \epsilon_i \phi$ where $i = c, v$ corresponds to core and valence states, respectively, and H is the single particle Hamiltonian $H = T + V$. On operating with H on eq. 2.26 and rearranging, one finds,

$$\left[H + (\epsilon_c - \epsilon_v) \sum_c |\phi_c\rangle \langle\phi_c|\right] \tilde{\phi}_v = \epsilon_v \left|\tilde{\phi}_v\right\rangle . \tag{2.27}$$

This takes the form of a Schrödinger equation for the pseudized wavefunctions $\tilde{\phi}_v$. It is therefore possible to construct an effective Hamiltonian that has the same eigenvalues as the original Hamiltonian. At the same time the pseudo-wavefunctions can be constructed to be nodeless and smoother in the core region. Modern day implementations of pseudopotentials often add several important ingredients to the above derivation. First, many pseudopotentials are constructed to satisfy norm-conservation of the pseudized wavefunctions in comparison to the original states. This allows for greater transferability to environments where the energy range of the eigenvalues do not depart too far from the ones used in the construction of the pseudopotential.

Another important consideration are relativistic pseudopotentials. These are constructed by considering Dirac's expression rather than the Schrödinger equation of eq. 2.2. This then allows for relativistic treatment of the core electrons, whereas valence electrons can still be treated non-relativistically with DFT.

There are numerous different recipes and implementations for pseudopotentials. Some of the more popular ones include for instance the pseudopotentials proposed by Troullier Martins (TM) [52] and those by Rappe, Rabe, Kaxiras and Joannopoulos (RRKJ) [53]. The pseudopotentials used in the work presented in chapters 4, 5 and 6 are based on the form by Goedecker, Teter and Hutter (GTH) [30, 54]. These are norm-conserving, relativistic, separable and dual-space pseudopotentials. They can be expressed in terms of a local (V_{loc}^{PP}) and nonlocal (V_{nl}^{PP}) part, where the local part in turn can be separated into a long-range term and a short-range term,

$$V_{loc}^{PP} = -\frac{Z_{ion}}{r}\mathrm{erf}\left(\alpha^{PP}r\right) + \sum_{i=1}^{2} C_i^{PP}\left(\sqrt{2}\alpha^{PP}r\right)^{2i-2} \times \exp\left[-\left(\alpha^{PP}r\right)^2\right], \qquad (2.28)$$

where Z_{ion} is the ionic charge and $\alpha^{PP} = \left(\sqrt{2}r_{loc}\right)^{-1}$. The nonlocal part takes the following form,

$$V_{nl}^{PP}\left(\mathbf{r},\mathbf{r}'\right) = \sum_{lm}\sum ij \left\langle \mathbf{r}\left|p_i^{lm}\right.\right\rangle h_{ij}^{l} \left\langle p_j^{lm}\left|\mathbf{r}'\right.\right\rangle, \qquad (2.29)$$

where the projectors have a Gaussian form,

$$\left\langle \mathbf{r}\left|p_i^{lm}\right.\right\rangle = N_i^l Y^{lm}\left(\hat{r}\right) r^{l+2i-2} \exp\left[-\frac{1}{2}\left(\frac{r}{r_l}\right)^2\right], \qquad (2.30)$$

where Y^{lm} are the spherical harmonics and N are normalization constants. It is important to point out that in contrast to many other pseudopotential approaches

that are based on tabulated values, this implementation is analytic with only a small number of parameters (C_i^{PP}, r_{loc}, r_l and h_{ij}^l). Normally the GTH pseudopotentials are considered too computationally intensive to be used in plane wave methods, but they are well suited for the gaussian plane wave approach. This will be discussed in greater detail in section 2.2.6.

Another commonly used approach based on similar ideas as pseudopotentials is that of projector augmented waves (PAW), first introduced by Blöchl [55]. This method will be used for the calculations performed in section 3. The main difference to the pseudopotential method, where the core electrons only enter through the effective potential of the pseudopotentials, is that within the PAW formalism all-electron wavefunctions are employed. The method relies on rewriting the original all-electron wavefunctions into a set of auxiliary wavefunctions that can be decomposed such that they are smooth everywhere except in well-defined small regions with rapid oscillations. Each part can be treated separately, where the rapidly oscillating part is treated similarly to the muffin-tin approach. A more detailed discussion can be found in the original work by Blöchl [55] and in for instance ref. [42]

2.2.6 Basis Sets

It is computationally advantageous to express the one-electron orbitals in a different mathematical form. This is achieved by expanding the one-electron orbitals,

$\psi_j(\boldsymbol{r})$, in a different basis,

$$\psi_j(\boldsymbol{r}) = \sum_{\alpha=1}^{M} c_{j\alpha}\phi_\alpha(\boldsymbol{r}), \tag{2.31}$$

where $\phi_\alpha(\boldsymbol{r})$ are the new basis set orbitals, M is the size of the basis set and $c_{j\alpha}$ are the expansion coefficients for each electron wavefunction $\psi_j(\boldsymbol{r})$. A wide variety of different types of basis set functions have been proposed. Amongst the most popular ones are plane waves [56], Gaussians [57], Slater functions [58], wavelets [59] and numerical atomic orbitals [60, 5]. The choice of the particular basis historically was mostly divided into two areas, those of the plane wave (PW) approach which was traditionally preferred in the physics community, and those of atom centered basis sets such as Gaussians, originally favored by the chemistry community. The difference between these in terms of accuracy for different systems has somewhat diminished today. Other approaches exist that combine different types of basis functions. In this way, parts of the mathematical problem of solving the KS-equations can be selectively addressed with one or the other method, thereby giving the possibility to take advantage of the best of both methods. One such approach is the Gaussian Plane Wave (GPW) approach, which will be used in the work of section 4, 5 and 6. In what follows, we proceed by giving a separate introduction to the different types of basis sets relevant to this work.

Plane waves

The PW approach was originally developed in the physics community and takes advantage of periodicity naturally found in many solid state systems. Considering Bloch's theorem we know that the solution of the Schrödinger equation for a constant potential are plane waves. This makes them natural candidates as a basis set in condensed matter system. It is possible to write the PW basis as,

$$\phi_{\boldsymbol{G}}^{\boldsymbol{k}}(\boldsymbol{r}) = \frac{1}{\sqrt{\Omega}} e^{i(\boldsymbol{k}+\boldsymbol{G})}, \tag{2.32}$$

where $\boldsymbol{k}$ are the wave vectors, $\boldsymbol{G}$ are the reciprocal lattice vectors and the PW basis functions are normalized by the unit cell volume Ω. This results in an expression for the one-electron wavefunctions,

$$\psi_j^{\boldsymbol{k}}(\boldsymbol{r}) = \sum_{\boldsymbol{G}=0}^{\infty} c_{j\boldsymbol{k}}(\boldsymbol{G})\, \phi_{\boldsymbol{G}}^{\boldsymbol{k}}(\boldsymbol{r})\,. \tag{2.33}$$

So far the expression in eq. 2.33 assumes an infinite basis in the sum. This would represent the one-electron wavefunctions to infinite accuracy. In practice one chooses an energy cutoff, thereby limiting the number of plane wave functions,

$$\frac{\hbar^2}{2m} |\boldsymbol{k} + \boldsymbol{G}|^2 < E_{cut}. \tag{2.34}$$

This is possible without significant loss of accuracy as it is found that the coefficients $c_{j\boldsymbol{k}}(\boldsymbol{G})$ become smaller as $|\boldsymbol{k} + \boldsymbol{G}|$ increases. The error that is introduced by ignoring high-energy expansion terms is also manageable in a reasonably straightforward fashion. Increasing the number of plane waves increases the accuracy, thereby allowing

for gradual mathematical convergence of the results. This is an important point and care has to be taken that calculations are appropriately converged.

The importance of introducing pseudopotentials for PW methods becomes more apparent now. Rapidly varying one-electron wavefunctions would require significantly greater energy cut-offs for the PW method, leading to an overall increase in the computational cost required.

Gaussian-type orbitals

Within the chemistry community, another commonly used approach that gives an alternative to PW methods is that of atom-centered basis sets. Of particular importance in this field are Gaussian-type orbitals. This was first introduced in 1950 by Boys [57]. A major advantage of Gaussians is that the integrals involved in solving the KS equations can be performed analytically. This is mathematically possible since the product of two Gaussians is another Gaussian. The form generally used is that of cartesian (primitive) Gaussians,

$$g_{ijk}(\boldsymbol{r}) = \chi_i(x)\,\chi_j(y)\,\chi_k(z)\,, \tag{2.35}$$

where,

$$\chi_i(x) = \left(\frac{2\alpha}{\pi}\right)^{\frac{1}{4}} \sqrt{\frac{(4\alpha)^i}{(2i-1)!!}}\, x^i e^{-\alpha x^2} \tag{2.36}$$

and equivalent expressions for the y and z parts. Most approaches in practice employ contracted Gaussians, $\phi_\mu(\boldsymbol{r})$, based on superpositions of primitive Gaussians, $g_w(\boldsymbol{r})$,

such that,

$$\phi_\mu(\boldsymbol{r}) = \sum_w d_{w\mu} g_w(\boldsymbol{r}), \tag{2.37}$$

where $d_{w\mu}$ are the respective contraction coefficients and the single parameter w is written for convenience and consist of i, j and k as in eq. 2.35. Using contracted Gaussians eliminates the problem that a single Gaussian would have zero derivative at the origin, which is in contrast to the behavior of atomic orbitals that have a cusp at the origin.

Gaussian plane waves

Mixed basis sets are approaches that try to combine the best of two worlds. This is the method used in QUICKSTEP [61] part of CP2K [3]. It combines a Gaussian basis with an auxiliary PW basis. The approach is therefore called Gaussian Plane Wave (GPW) method. Only the main ideas involved in the GPW method will be outlined below and a detailed account of the methodology and implementation can be found in several excellent reviews [61, 62, 63]. The method works by defining two representations of the electronic charge density, the first is based on atom centered contracted Gaussians,

$$n(\boldsymbol{r}) = \sum_{\mu\nu} P^{\mu\nu} \phi_\mu(\boldsymbol{r}) \phi_\nu(\boldsymbol{r}), \tag{2.38}$$

where $P^{\mu\nu}$ are the density matrix elements and the contracted Gaussians are as defined in eq. 2.37. The second auxiliary representation of the electronic density takes

advantage of the PW basis by defining,

$$\tilde{n}\left(\boldsymbol{r}\right)=\frac{1}{\Omega}\sum_{\boldsymbol{G}}\tilde{n}\left(\boldsymbol{G}\right)e^{i\boldsymbol{G}\cdot\boldsymbol{r}}, \tag{2.39}$$

where $\tilde{n}\left(\boldsymbol{G}\right)$ are expansion coefficients that ensure that the electronic density expressed in the PW basis, $\tilde{n}\left(\boldsymbol{r}\right)$, equals the primary electronic density in terms of the Gaussian basis, $n\left(\boldsymbol{r}\right)$. Equality is enforced on a regular grid in the unit cell. To transform between the different representations efficient FFT methods can be used. Within the GPW framework individual KS energy terms are evaluated with either Gaussians or the auxiliary PW basis set. The choice for each term depends on which basis has greater numerical efficiency. The different terms are carefully defined here,

$$E\left[n\right]=E^{T}\left[n\right]+E^{V}\left[n\right]+E^{H}\left[n\right]+E^{XC}\left[n\right]+E^{II}. \tag{2.40}$$

Given the two basis sets as defined in eq. 2.37 and 2.32 the individual terms then take the following form. The kinetic energy is,

$$E^{T}\left[n\right]=\sum_{\mu\nu}P^{\mu\nu}\left\langle\phi_{\mu}\left(\boldsymbol{r}\right)\right|-\frac{1}{2}\nabla^{2}\left|\phi_{\nu}\left(\boldsymbol{r}\right)\right\rangle, \tag{2.41}$$

which in the Gaussian basis is analytic. The electronic interaction with the ions, $E^{V}\left[n\right]$, is described using the GTH pseudopotentials [30, 54] as described in section 2.2.5 and is separated in a local and non-local part,

$$E^{T}\left[n\right]=\sum_{\mu\nu}P^{\mu\nu}\left\langle\phi_{\mu}\left(\boldsymbol{r}\right)\right|V_{loc}^{PP}\left(r\right)\left|\phi_{\nu}\left(\boldsymbol{r}\right)\right\rangle+\sum_{\mu\nu}P^{\mu\nu}\left\langle\phi_{\mu}\left(\boldsymbol{r}\right)\right|V_{nl}^{PP}\left(\boldsymbol{r},\boldsymbol{r'}\right)\left|\phi_{\nu}\left(\boldsymbol{r}\right)\right\rangle, \tag{2.42}$$

with $V_{loc}^{PP}\left(r\right)$ and $V_{nl}^{PP}\left(\boldsymbol{r},\boldsymbol{r'}\right)$ defined in eq. 2.28 and 2.28, respectively. The short range terms are again analytic in the local Gaussian basis and the long-range terms

can be treated as part of the electrostatic terms. The electrostatic interaction term is generally not well handled by Gaussians, but comparatively easily using PW in reciprocal space. The Hartree term, $E^H[n]$, is therefore evaluated using the PW basis,

$$E^H[n] = 2\pi\Omega \sum_{\boldsymbol{G}} \frac{\tilde{n}^*(\boldsymbol{G})\,\tilde{n}(\boldsymbol{G})}{\boldsymbol{G}^2}. \tag{2.43}$$

The exchange correlation energy is similarly evaluated using the PW basis grid,

$$E^{XC}[n] = \int e^{XC}(\boldsymbol{r})\,d\boldsymbol{r}. \tag{2.44}$$

This leaves the last term, the interaction energy of the ionic cores,

$$E^{II}[n] = \frac{1}{2} \sum_{I \neq J} \frac{Z_I Z_J}{|\boldsymbol{R_I} - \boldsymbol{R_J}|}. \tag{2.45}$$

The advantage of using a mixed basis is therefore provided by evaluating individual terms with either Gaussians or plane waves.

2.3 The embedded atom method

So far the discussion in this chapter has solely dealt with first-principles approaches. Although based on ideas from density functional theory, the embedded atom method (EAM), originally proposed and developed by Daw and Baskes [64, 65], instead is an empirical method in its implementation. The method is based on the result from the work of Hohenberg and Kohn that the energy of a system is a functional of the density. This led Daw and Baskes [64, 65] to introduce an embedding

function, $F(\rho)$, that describes the energy change as a single atom is added to the electron background charge. They propose that the total energy takes the form,

$$E_{tot} = \sum_i F(\rho_i) + \sum_{ij} V(r_{ij}), \tag{2.46}$$

where ρ_i is the local electron charge density and $V(r_{ij})$ is a two-body pair potential. The electron charge density is approximated by a linear superposition of the densities of the individual atoms, $\rho(r_{ij})$,

$$\rho_i = \sum_{j \neq i} \rho(r_{ij}). \tag{2.47}$$

The particular mathematical form of the EAM results in a very small computational cost, similar to that of traditional pair potentials. At the same time, the accuracy of the results is dramatically improved over pair potentials. The EAM has been found to give excellent results for many system, especially for metals where directional bonding plays a minor role such as the two metals treated in this work, Cu and Ni. It is important to point out here that although the EAM takes its roots from ideas from DFT by considering the densities of the system, it is by no means a first-principles approach and is inherently an empirical method. The functions in eq. 2.46 are in practice used as fitting functions based on *ab-initio* or experimental work. This makes relating the physical meaning of the individual terms to the quantum system difficult at best.

Despite its success, the EAM has several short-comings. The functions in eq. 2.46 are fitted and tabulated based on experimental or *ab-initio* results. This limits a

particular EAM potential to a specific element and the transferability for the same element to different environments or structures is not guaranteed. There is no *a priori* knowledge that an EAM potential, fitted based on a particular set of conditions will perform well for others. For instance fitting for a bulk material does not mean that one can *a priori* say that this EAM will perform well for materials with defects or under extreme conditions. Being a empirical method, extra attention has to be paid to the particular system that is being studied and whether it is within the limits of the particular EAM potential employed.

Another potential short-coming of the EAM is that it is not necessarily straightforward to identify the underlying physics responsible for a given process, in particular if this is based on understanding the electronic density. Although the EAM is based on the electron density, this has become to all intense and purpose a fitting function that has only a loose connection with the real electron densities. This was addressed in recent work by Mitev *et al.* [66, 67] but commonly used EAM potentials have no direct connection to the electron densities.

Finally, the main disadvantage of the EAM for the particular work undertaken here is the need for potentials for each element in a particular structure. This is a complication for alloy systems but similarly also if one tries to study impurities. The latter is particularly complicated as tabulated EAM potentials would have to be developed for each impurity and the surrounding matrix. This would have to include considerations such as applicability of the potentials for given concentrations, which

coincides with the disadvantage of no *a priori* knowledge of the applicability of given potentials discussed above. In general, developing a new potential is a complicated task and if not done right, can lead to significant errors.

Chapter 3

Sulfur induced embrittlement of Nickel: A first principles study

3.1 Overview

We study the embrittlement of Ni due to the presence of S impurities, considering their effect in the bulk and at grain boundaries. For bulk Ni, we employ Rice's theory based on generalized-stacking-fault energetics and the unstable stacking energy criterion. We use first-principles density-functional-theory calculations to determine the ductility parameter $D = \gamma_s/\gamma_{us}$, the ratio of the surface energy γ_s to the unstable stacking energy γ_{us}, for bulk Ni with substitutional S impurities. Similar arguments based on Rice's theory for the mechanical properties of grain boundaries (GB's) are invoked. We study the $\Sigma5(012)$ GB with interstitial S impurities, in which case

D is defined as the ratio of the work of separation W_s and the unstable stacking energy γ_{us}, to model the competition between grain decohesion and shear-induced plastic deformation due to grain boundary sliding (GBS). The presence of S impurities is found to increase the value of D by $\sim$ 40% in bulk Ni, but reduces it by over 80% for the GB. These results support earlier suggestions that embrittlement of Ni by S impurities is related to their effect on grain boundaries. We further calculate relevant tensile and shear stresses to study the expected fracture mode and find that intergranular crack propagation accommodated by GBS is inhibited in the system considered here.

3.2 Introduction

Embrittlement of ductile metals by chemical impurities is a process of great importance in materials used in a wide range of technologies, ranging from transportation to the energy industry. Although this process has been known in industry for a long time, the fundamental mechanisms underlying chemical embrittlement are not understood at the atomic level. More detailed knowledge of atomistic level processes can lead to improvements in the design and efficiency of many practical applications. In the present study we concentrate on the effects of S impurities on the mechanical properties of Ni. This system is of great industrial interest since nickel-based alloys are widely used, whilst sulfur is a common impurity during processing steps and in many operating environments.

Much experimental effort has been devoted to the study of S impurities in Ni. These impurities segregate at the grain boundaries (GB's) [68, 69, 70, 71, 72, 73, 74, 75, 76] and lead to a transition from ductile transgranular to brittle intergranular fracture at high concentrations in microcrystalline materials [68, 69, 70, 71, 72, 73, 74]. Recent experimental work identified a critical S impurity concentration for this transition, accompanied by amorphization [76]. Theoretical work addressed some of these issues of chemical embrittlement from an atomistic viewpoint. Chen *et al.* [77] performed large-scale Molecular Dynamics (MD) simulations supporting the experimental work by Heuer *et al.* [76]. Yamaguchi *et al.* [78] used first-principles density-functional-theory calculations to provide theoretical evidence for the segregation effect of sulfur near GB's and showed how this effect leads to weakening of the structure by decohesion. Kart *et al.* [79] were able to confirm those results. Similarly, Sanyal *et al.* [80] studied the effects of different impurities on the decohesion of a Ni GB and related this to chemical embrittlement.

Most of these experimental and theoretical studies have addressed the behavior and processes in coarse-grained materials. Recent advances in processing techniques have enabled selective growth of ultrafine crystalline (ufc) and nanocrystalline (nc) materials. GB engineering techniques have enabled control over the grain boundary structure. Manipulating the grain sizes and the grain boundary structure may result in enhancements in the mechanical properties. Kobayashi *et al.* [73], for instance, have shown that special GB's have higher resistance to S embrittlement in ufc Ni.

At the same time, these techniques make a deeper understanding of the underlying atomic-scale processes more important in order to effectively take advantage of the microstructure. For example, different response mechanisms are thought to apply to coarse-grained than nc metals. Several classical MD studies have highlighted the importance of intergranular deformation mechanisms in nc metals [19, 20, 21, 22, 23, 24]. These results were instrumental in showing that in contrast to coarse-grained metals, GB's in nc metals do not merely act as static barriers for crystal dislocations. Instead, as grain sizes become smaller, the GB's themselves play an increasingly important role in plastic deformation and fracture [19, 20, 21, 22, 23, 24]. In this context plastic deformation can be facilitated by GB sliding (GBS). Most theoretical and computational studies to date, that addressed chemical embrittlement of Ni from an atomistic level, have considered the decohesion behavior of GB's [78, 79, 80] but not shear effects, which could be of crucial importance.

The mechanical behavior of solids is inherently connected to the issue of brittle or ductile response. The terms "brittle" and "ductile" refer to macroscopic response, which ultimately is related to the atomic scale structure and nature of bonding between atoms in the solid. The connection between macroscopic behavior and atomic-scale structure is not trivial, and remains the focus of vigorous research in many classes of materials. Armstrong [81] and Kelly *et al.* [82] first suggested that the difference between the two types of responses is due to competition between decohesion (also referred to as "Griffith cleavage") and plastic deformation (or shear) at the tip

of a crack inside the solid; these ideas were subsequently put on a more quantitative basis first by Rice and Thomson [83] and later by Rice [84] who related the decohesion and shear tendencies to specific energy terms that can be ultimately connected to the atomic structure of the solid. This provided a criterion for determining the brittle or ductile response of the solid by calculating the relevant energy terms, from atomic-scale considerations. The approach based on Rice's criterion [84] for brittle versus ductile behavior can give a clear picture of the effect of the chemical composition of the solid and of changes in it, for example, the introduction of impurities on the mechanical properties. We extend the original Rice's theory to study ductile vs. brittle response at GB's of small sized grains, by considering the competition between plastic deformation facilitated by shear in the form of GBS and brittle response induced by grain decohesion. Specifically, we examine whether or not S impurities at GB's in Ni are the dominant mechanism for its embrittlement. To this end, we calculate the decohesion energy and unstable stacking energies both for bulk Ni and for a representative GB in Ni, and compare these values for the pure structures and structures with S impurities at the relevant slip and decohesion planes. Our results show that in bulk Ni, the presence of S impurities leads to an *increase* in ductility. In contrast to this, we find clear evidence of S-induced embrittlement for the case of the Ni GB, introduced by a decrease in the required work of separation and suppression of GBS. This supports the view that S impurity segregation at the Ni GBs is a dominant effect in its embrittlement.

The chapter is organized as follows: in Section 3.3 we present the theoretical framework for interpreting our first principles calculations in the context of macroscopic continuum theory, together with a description of our specific computational model. Section 3.4 presents the results of our calculations for the key quantities that characterize brittle or ductile response for bulk Ni and the Ni GB, with or without the S impurities. Finally, in Section 3.5 we discuss our conclusions.

3.3 Theoretical framework

Macroscopic theories have been used extensively to describe the mechanical behavior of materials. Early work by Rice and Thomson [83], modeled the process of nucleation of dislocations at the tip of a crack as the fundamental mechanism of plastic shear. Subsequently, Rice [84] used the Peierls concept [85] to quantify the competition between cleavage and plastic shear at the tip of a crack, which are related to brittle versus ductile response of a stressed solid, in terms of two key quantities: the surface energy of newly exposed surfaces due to cleavage, γ_s, and the unstable stacking energy, γ_{us}, the lowest energy barrier for sliding two halves of a periodic crystal over a full period across a crystal plane. Using this theoretical framework, studies of representative solids with effective interatomic potentials [86] or first-principles total-energy calculations [87] were carried out to elucidate the nature of brittle or ductile response of various materials. Extensions of these studies to more realistic situations [88, 89, 90] were employed to predict the change in mechanical response

due to impurities [91, 92]. Thus, the combination of Rice's continuum macroscopic theory, coupled with high-accuracy atomistic scale calculations for the values of key quantities like γ_s and γ_{us}, can be useful for addressing qualitatively the complicated issue of brittle versus ductile behavior in the presence of chemical impurities.

In this approach, the main point is that a large value of the ratio $D = \gamma_s/\gamma_{us}$, called the ductility parameter [93], implies ductile behavior because it corresponds either to a large energy cost for cleavage (large γ_s) or to a small energy cost for dislocation nucleation (small γ_{us}); conversely, a small value of D implies brittle behavior due to a small cost of cleavage (small γ_s) or large cost for dislocation nucleation (large γ_{us}). There is however no general rule for what constitutes "large" or "small" values of D in such comparisons; it depends on the specific system under consideration. For example, in what concerns the behavior of fcc metals, Rice [84] previously estimated the critical value of D to lie between 4 and 9 and was able to successfully correlate the values of the ductility parameter D of several metals to the correct experimental behavior. When the interest is specifically focused on the role of chemical impurities, the task is simpler: the values of γ_s and γ_{us} can be calculated with or without impurities, and the resulting comparison can give strong indications about the likely role of the impurities [91, 92]. The use of first-principles quantum mechanical calculations that faithfully represent the chemical character of various species of atoms makes it possible to obtain accurate values for γ_s and γ_{us}, at least in cases where the relevant geometries are simple enough to make such calculations feasible.

For the most part in this study we consider the simple ratio of the unstable stacking energy, γ_{us}, and the surface energy, γ_s, to calculate the ductility parameter D. This is sufficient when the geometries, and in particular the Burgers vectors, of the system of interest do not change significantly when impurities are present or not. When the Burgers vectors change as impurities are introduced, a more careful definition of the ductility parameter $\tilde{D}$ is required. Rice showed that, for mode I loading, the energy release rate for dislocation nucleation is [83],

$$G_d = 8\frac{1+(1-\nu)\tan^2\phi}{(1+\cos\theta)\sin^2\theta}\gamma_{us}, \tag{3.1}$$

where θ is the angle between the slip and decohesion planes (see Fig. 3.1) and ν is the Poisson ratio; the angle ϕ is the one subtended between the normal to the intersection of the slip and decohesion planes which lies on the slip plane and the Burgers vector [84]. The energy release rate for Griffith cleavage is $G_c = 2\gamma_s$. The most general definition for the ductility parameter $\tilde{D}$ is then $\tilde{D} = G_c/G_d$. For situations where θ and ϕ are constant $\tilde{D} = \alpha D = \alpha\,(\gamma_s/\gamma_{us})$, with α being a constant factor determined by geometric considerations.

We extend here the concept of the generalized energy surface, or γ-surface, first discussed by Vitek [94], to the case of a GB. Specifically, we use the work of separation (W_s) and the minimal energy required to shear the GB (γ_{us}), in the same spirit as these are used in relation to decohesion and slip planes in the bulk of a regular crystal. We note that the decohesion (cleavage) and slip planes in a crystal are often different [92]. In the case of a GB it is a reasonable choice to identify both the

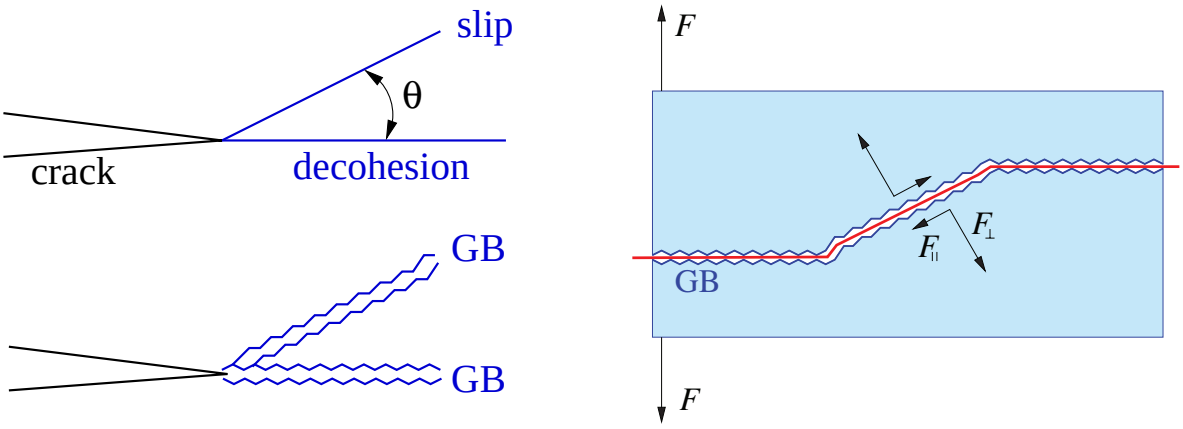

Figure 3.1: Illustration of slip/decohesion planes at a relative angle θ, in the bulk (left panel, straight lines represent bulk planes), in the presence of GB's (represented by jagged lines), and possible inter-granular failure mechanism (right panel, fracture along red boundary between GB's) due to external load, with forces denoted as F and their parallel $F_{||}$ and perpendicular $F_{\perp}$ components on a given GB.

decohesion and slip planes with the GB plane, since this is the weak plane of the system on which either decohesion or slip may occur. In the context of GB's γ_{us} now quantifies the resistance against shear and can therefore still be taken as a measure of ductility. The competing process of greatest importance is that of cleavage, quantified by the work of separation (W_s) for intergranular decohesion along the GB. We can then define in a similar manner as in the original Rice's theory a ductility parameter as the ratio of these two competing processes $D^{GB} = W_s/\gamma_{us}$. We will use the natural cleavage plane of bulk fcc Ni, the (111) plane, and the $\Sigma5(012)$ GB as a prototypical planar defect that has been the subject of detailed studies recently [78, 79, 80].

The total energy of various structures, from which the key quantities discussed above can be directly obtained, are calculated using density-functional-theory as im-

plemented in the VASP code [4]. The generalized gradient approximation (GGA) [28] with projector-augmented plane wave (PAW) potentials [29] was used for all calculations. We elected to perform spin polarized calculations to improve accuracy, since Ni can be a magnetic solid. A kinetic energy cutoff of 330 eV was used after carefully testing for convergence when the geometry of the system is changed during slip calculations and when S impurities were included. The Methfessel-Paxton smearing of second order [95] was used with a smearing width of 0.1 eV. All relaxations were performed using the conjugate-gradient method as implemented in VASP. Finally, a uniform Monkhorst-Pack [96] k-point grid of $15 \times 15 \times 15$ was used for the fcc bulk Ni calculations with 4 atoms in the cubic unit cell and scaled appropriately for larger supercells (for instance, a $2 \times 2 \times 1$ grid was used for the supercell with a GB, as in similar works [78, 79]).

With these computational parameters, we determined the lattice constant for fcc Ni by fitting the Birch-Murnaghan equation of state, which results in a lattice constant of $a = 3.52$ Å and a bulk modulus of $B = 185.8$ GPa which compare well with the experimentally determined values of $a = 3.52$ Å [97] and $B = 186$ GPa [97]. Relaxation of the unit cell volume was explicitly taken into account when impurities are introduced in the host crystal.

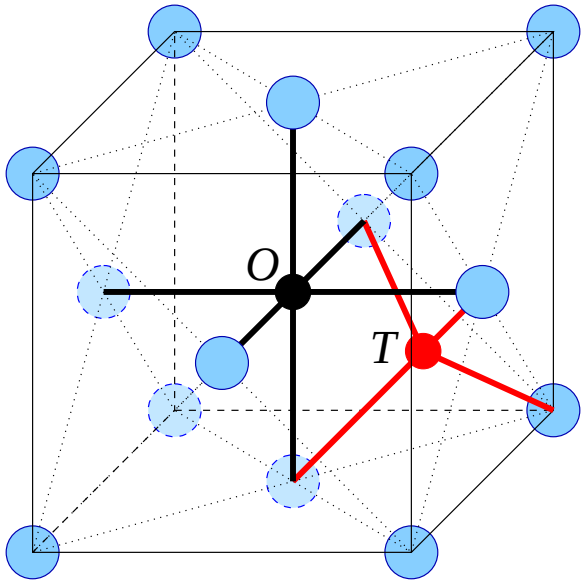

Figure 3.2: Illustration of the two interstitial sites in the fcc lattice: the regular lattice sites are shown as blue circles, the tetrahedral interstitial (T) is shown as a red circle and linked by red lines to its 4 nearest neighbors and the octahedral interstitial (O) is shown as a black circle and linked by black lines to its 6 nearest neighbors.

3.4 Results and Discussion

We address first the question of where the S impurities sit in the case of the fcc bulk structure and the $\Sigma5(012)$ GB. For bulk Ni, in general, impurities can be accommodated at either interstitial or substitutional sites. There are two interstitial positions in the fcc lattice where impurities typically reside [98], the so called "tetrahedral" (T) and "octahedral" (O) sites, named after the coordination of these sites with nearest neighbor regular lattice sites; the position of these defects in the lattice is indicated in Fig. 3.2.

To determine the optimal position for the impurities we calculated the formation

energy ε_f^X per impurity, defined as:

$$\varepsilon_f^X = \frac{1}{n_i}\left[E_{tot}^X(n_i, n_h) - E_{tot}\left(n_h^0\right) - n_i\mu_i - \left(n_h - n_h^0\right)\varepsilon_h\right] \tag{3.2}$$

where $E_{tot}^X(n_i, n_h)$ is the total binding energy of the system containing n_i impurities of type X ($X = I_T$ or I_O for the interstitial tetrahedral and octahedral positions in bulk Ni, and S for the substitutional positions), and n_h atoms of the host crystal, $E_{tot}\left(n_h^0\right)$ is the total binding energy of the system without impurities containing n_h^0 host atoms, μ_i is the chemical potential for the impurities and ε_h is the binding energy per atom of the host crystal in its ideal structure. In this expression, the supercell is chosen so that $n_i \ll n_h$ (ideally, $n_h \to \infty$). We have considered two different reservoirs for S, isolated S atoms (equivalent to the limit of $\mu_S = 0$) and bulk S, which consists of puckered hexagonal or octagonal stacked rings of S [99]. To obtain the bulk S chemical potential, we optimized the structures using the same computational parameter as for bulk Ni and a cubic supercell of large size (with lattice constant up to 28 Å), and found that in the hexagonal rings the S–S bond length is 2.06 Å and the S–S–S bond angle is 102°, whereas for the octagonal rings the bond length is 2.04 Å and the bond angle is 108°. The difference in chemical potential between the hexagonal and octagonal rings is only 0.07 eV in favor of the latter, so we will quote results in the rest of the paper for the octagonal ring structure only, which corresponds to $\mu_S = -3.22$ eV. The results of these calculations for the formation energy of S point defects in bulk Ni are given in Table 3.1. We find that the energy of formation of the S interstitial defect at both the tetrahedral and octahedral positions are $I_T = 3.16$ eV

X	Θ	ε_f^X
I_T	0.92%	3.16
I_O	0.92%	1.96
S_b	0.93%	0.38
I_{GB}	0.25	−0.89
I_{GB}	1.0	−1.21
S_{GB}	0.33	0.35

Table 3.1: Formation energies ε_f^X (in eV) from Eq. (5.1) of the various S point defects in bulk Ni and at the $\Sigma5(012)$ grain boundary, for the S chemical potential $\mu_S = -3.22$ eV (corresponding to bulk S, consisting of stacked octagonal rings). $X = I_T, I_O$ are the bulk interstitial positions (tetrahedral and octahedral, respectively), $X = S_b$ is the bulk substitutional position, I_{GB}, S_{GB} are the grain boundary interstitial and substitutional positions. Bulk concentrations Θ correspond to percentage of impurities in the supercell; GB concentrations correspond to the defect plane ratio for the GB0 plane.

and $I_O = 1.96$ ev, respectively. This is significantly greater than the formation energy of a substitutional S defect, namely $S_b = 0.38$ ev. These results suggest that the only relevant S defect in bulk Ni is the substitutional.

We have performed similar calculations for the formation energy of impurities at the GB plane. The open spaces on the GB plane allow energetically favorable interstitial S impurities (this is explained in more detail in the next subsection, 3.4.2). In the context of the following calculations of the unstable stacking and decohesion energies, it is useful to introduce at this point a convenient measure of the impurity concentration on a defect plane. We follow the literature convention [100] of defining the defect plane impurity concentration Θ as the ratio of the number of S atoms to the number of Ni atoms on the respective defect plane. The planes used throughout will be the cleavage or slip planes. Table 3.1 summarizes the formation energies for

the case of one and four S atoms in a unit cell containing four Ni atoms on each plane parallel to the GB plane, that is, for $\Theta = 0.25$ and 1.0 (see Fig. 3.5). These values include supercell volume relaxation. The unit cell volume for the GB with impurities increases: the lattice constant perpendicular to the GB plane ($a_3 = 16.40$ Å in the pure Ni case) expands by 1% and 3% for $\Theta = 0.25$ and 1.0, respectively; of the other two lattice vectors in the plane parallel to the GB, one ($a_1 = 7.02$ Å in the pure Ni case) contracts by 1% for both S concentrations, and the other ($a_2 = 7.85$ Å in the pure Ni case) expands by 1% and by 2% for $\Theta = 0.25$ and 1.0, respectively. The energy gain due to the volume relaxation is very small and the S inclusion energy dominates. The formation energies in this case are considerably lower than for bulk Ni. This finding indicates that S atoms segregate at the GB's under thermodynamic equilibrium conditions, but it does not address the kinetic issue, that is, how easily S atoms diffuse to the optimal equilibrium sites at the GB. A detailed study explicitly treating S diffusion from first principles is beyond the scope of the present work. Experimentally it is known that S diffuses to the GB [68, 69, 70, 71, 72, 73, 74, 75, 76], which is consistent with our results of low energy positions of S impurities being associated with the GB. The concentrations were chosen with experiments in mind [70, 76]: for $\Theta = 1.0$ in our case, the equivalent concentration to experimental ones would be approximately 9%, taking into account the total amount of Ni atoms that the supercell contains in the neighborhood of the GB.

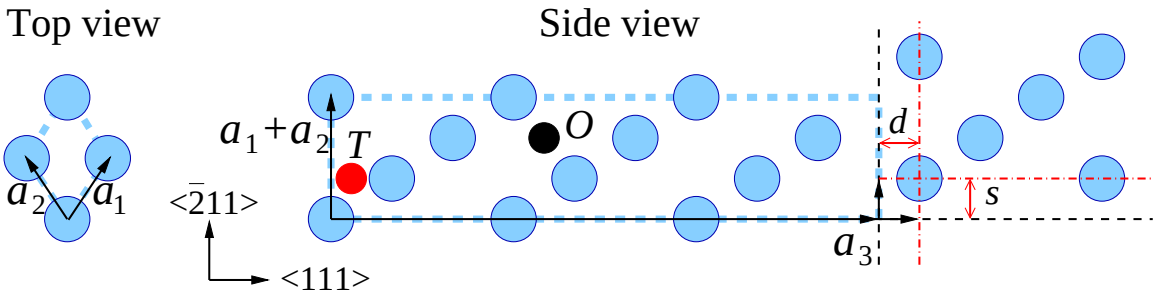

Figure 3.3: Setup for the calculation of γ_s and γ_{us} in bulk fcc Ni: Ni atoms are represented by blue circles. The top view shows the unit cell vectors $\mathbf{a_1}, \mathbf{a_2}$ on the (111) plane. The side view shows the atoms along the $\langle 111 \rangle$ crystal direction, with the corresponding lattice constant a_3. The thick dashed blue line represents the boundary of the supercell in the ideal crystal, which contains 9 (111) planes of atoms. Changes in the supercell lattice constant (indicated by the small vertical and horizontal arrows) define the distortions through which γ_s and γ_{us} are determined: these distortions are shown as double-headed arrows d (for decohesion) and s (for slip), and correspond to a displacement of atomic planes from their positions in the ideal crystal, indicated by black dashed lines, to new positions, indicated by dash-dotted red lines. The red circle labeled T and the black circle labeled O indicate the tetrahedral and octahedral interstitial sites in the bulk.

3.4.1 Decohesion in bulk fcc Ni

We begin with a description of the unit cell for calculating the surface energy, γ_s, and unstable stacking energy, γ_{us}, for bulk Ni. The relevant plane for such calculations, on which both decohesion (cleavage) and slip take place in the fcc crystal is the (111) plane; this is illustrated in Fig. 3.3. The surface energy is determined by increasing the length of the supercell vector $\mathbf{a_3}$ along the $\langle 111 \rangle$ crystallographic direction by d until the energy reaches an asymptotic value which is $2\gamma_s$ higher than the equilibrium energy. For consistency, we use the Universal Binding Energy Relation (UBER) [101] to fit the results of changing the value of d, in order to determine the asymptotic value for $d \to \infty$.

To find the surface energy, γ_s, for bulk fcc Ni decohesion in the $\langle 111 \rangle$ direction, we also need to specify how the atoms relax in the process of separating the two halves of the crystal while exposing two (111) planes. For an unambiguous definition of the decohesion distance d, the atoms on either side of the cut must be at a fixed distance in the $\langle 111 \rangle$ direction. Since for the calculations of the bulk decohesion the periodicity on the (111) plane is that of the bulk structure, the above restriction implies that all atoms on the two planes immediately adjacent to the cut are fixed in all directions, at the required distance d between the planes. All other atoms in the unit cell are allowed to relax fully.

For the decohesion calculation in the presence of S impurities, we used a supercell with 2×2 periodicity in the $\mathbf{a_1}$ and $\mathbf{a_2}$ lateral directions. This allows us to consider different concentrations of S impurities, by replacing one or more of the Ni atoms on the plane next to the cut by S atoms. We have considered two cases for the cleavage plane, $\Theta = 0.33$ (one substitutional S atom in the 2×2 supercell) and $\Theta = 1.0$ (two substitutional S atoms in the 2×2 supercell). These concentrations were chosen primarily in order to be able to have a direct comparison to the concentrations in the case of the GB calculations. The results of the decohesion calculations are shown in Fig. 3.4(a). The surface energy decreases by 27% in the case of $\Theta = 0.33$ on the cleavage plane and by 51% in the case of $\Theta = 1.0$.

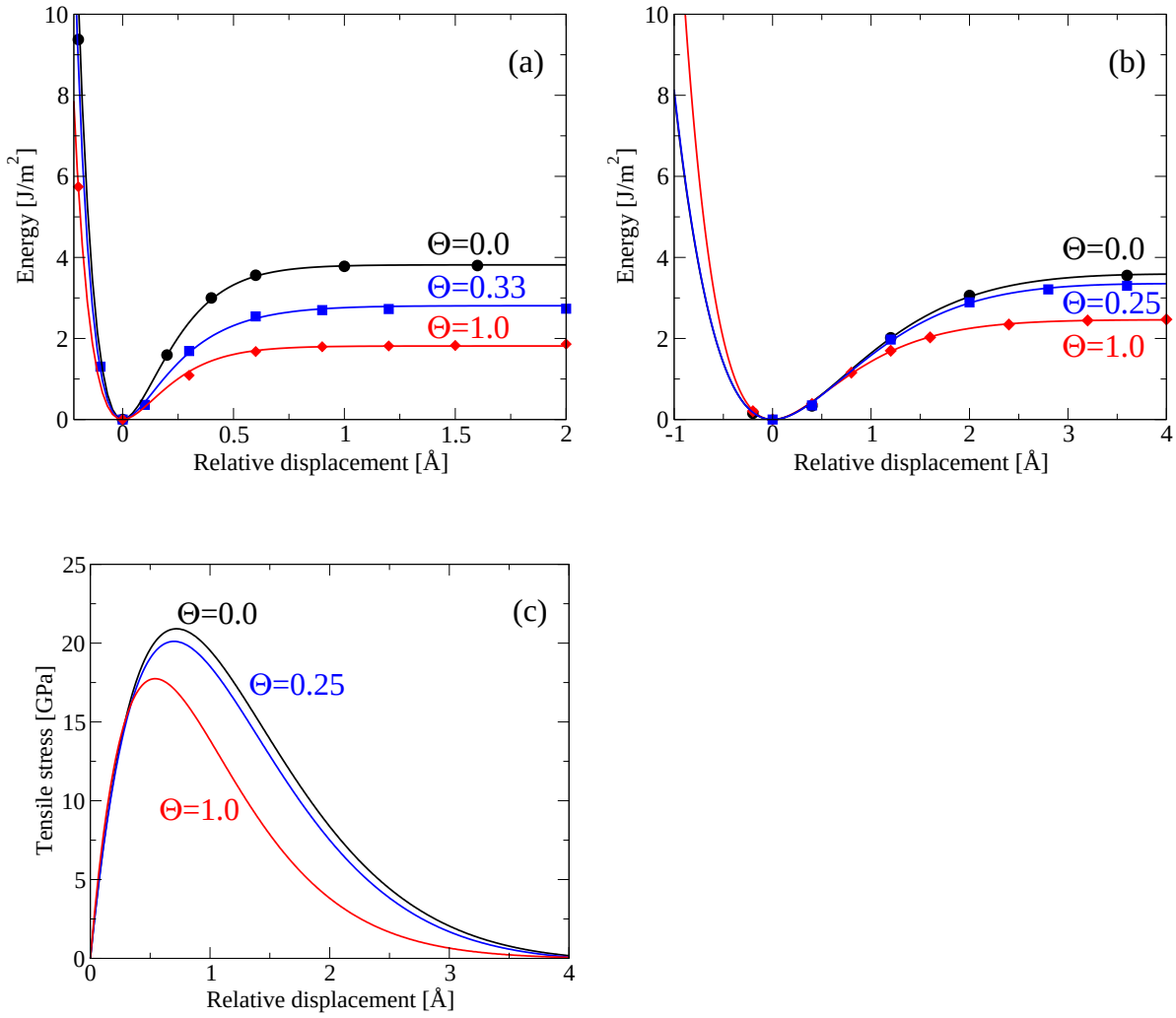

Figure 3.4: (a) Decohesion energy for bulk (111) Ni, without impurities ($\Theta = 0.0$) and at two S impurity concentrations, $\Theta = 0.33, 1.0$ (see text for details). (b) Decohesion energy for the $\Sigma5(012)$ GB without impurities ($\Theta = 0.0$) and at two S impurity concentrations, $\Theta = 0.25, 1.0$ (see text for details). (c) Corresponding tensile stress for the GB, without and with S impurities.

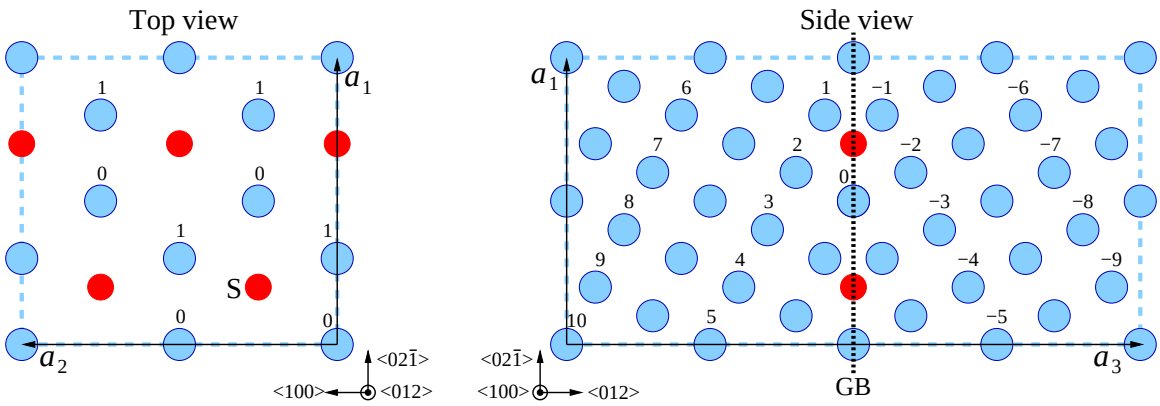

Figure 3.5: Setup for the calculation of the $\Sigma 5(012)$ GB: Ni atoms are represented by blue circles, possible interstitial positions for S atoms are indicated by smaller red circles. The top view shows the unit cell vectors $\mathbf{a_1}, \mathbf{a_2}$ on the (012) plane, parallel to the GB. The side view shows the atoms along the $\langle 012 \rangle$ crystal direction, with the corresponding lattice constant a_3. The thick dashed blue line represents the boundary of the supercell, which contains 20 (012) planes of atoms, labeled $-9, \ldots, 0, \ldots, 10$ (only one atom per plane is labeled). Each plane contains 4 atoms, labeled in the top view for planes 0 and 1. There are two GB's in each unit cell, at planes labeled 0 and 10. Decohesion calculations are performed by increasing the magnitude of $\mathbf{a_3}$ by d and moving all atoms in the top half of the cell by the same amount so that a gap appears at GB0. GSF energy calculations are performed by displacing all the atoms in one half of the cyrstal (defined by a cut between GB0 and GB1) with respect to the other.

Bulk Ni				Σ5(012) GB			
Θ	0.0	0.33	1.0	Θ	0.0	0.25	1.0
γ_s [J/m^2]	1.91	1.40	0.93	$\tilde{W}_s$ [J/m^2]	3.56	3.06	2.24
γ_{us} [J/m^2]	0.29	0.17	0.10	γ_{us} [J/m^2]	0.30	0.63	1.24
$D = \gamma_s/\gamma_{us}$	6.6	8.2	9.3	$D^{GB} = \tilde{W}_s/\gamma_{us}$	11.86	4.86	1.80
				σ_t [GPa]	20.91	20.11	17.74
				σ_s [GPa]	6.41	7.84	15.04

Table 3.2: Surface (γ_s) and unstable stacking (γ_{us}) energies and ductility parameter (D) for the bulk Ni; work of separation (W_s) and unstable stacking (γ_{us}) energies and ductility parameter (D^{GB}) for the Σ5(012) GB, for different concentrations Θ of S impurities. σ_t and σ_s are the corresponding tensile and shear strengths for the GB without or with S impurities.

3.4.2 Decohesion in fcc Ni with a grain boundary

For the GB calculations we consider a Σ5(012) structure, the same as in recent other work [78, 79, 80]. This GB has energetically and structurally advantageous interstitial sites for the incorporation of S impurities. The structure of this GB is shown in Fig. 3.5. The S impurities in our calculations of the work of separation are added to the 4 interstitial sites on the GB0 plane, equidistant from the 3 adjacent Ni atoms as shown in Fig. 3.5. The inclusion of impurities leads to a change in the supercell volume, as described earlier. The formation energy of the GB, obtained by comparing the energies of the supercell with the GB and a supercell which has exactly the same geometry and number of Ni atoms but no GB, is $\Delta E^{GB} = 1.21$ J/m^2, which compares well with the results reported earlier for the same GB (1.19 J/m^2 [78]). The calculated energy difference includes both the energy change due to supercell volume relaxation and the structural changes introduced by the GB.

To determine the work of separation W_s, a cut is introduced at the GB between layers GB0 and GB1. Here the situation is more complicated than for the decohesion of the perfect Ni crystal discussed earlier. We consider two cases: in the first, denoted as W_s, all the atoms on the decohesion planes are held fixed; in the second, denoted as $\tilde{W}_s$, we allow relaxations on the planes on either side of the cut by fixing only one reference Ni atom in each cut plane. We discuss first the result of the case with fixed atoms, which are shown in Fig. 3.4(b). The fit using UBER allows us to extract the decohesion energy for $d \to \infty$. Table 3.2 summarizes the results. In the absence of impurities the decohesion energy of the GB is smaller than that of bulk (111) Ni by only 7%. This is reasonable since the exposed surfaces upon decohesion of the GB are the $(0\bar{2}1)$ crystal surfaces, which have higher surface energy than the (111) surface, but the reference structure in this case includes the GB, which itself is a higher energy structure than the ideal bulk crystal. When S impurities are added, W_s is lowered by 7% for $\Theta = 0.25$ (one S atom in the unit cell of the GB0 plane), and by 31% for $\Theta = 1.0$ (four S atoms in the unit cell of the GB0 plane). This is consistent with calculations for the cleavage energy reported by Sanyal *et al.* [80]. The reduction in W_s is much smaller than the corresponding reduction of the decohesion energy in the ideal Ni crystal upon the incorporation of S impurities. When surface relaxation is included, the resulting work of separation $\tilde{W}_s$ is generally lower. In the absence of S impurities the difference between W_s and $\tilde{W}_s$ is negligible. With S impurities, the effect of relaxation is stronger, and the values of $\tilde{W}_s$ are lower than that of the pure

GB by 14% and 37% for $\Theta = 0.25$ and 1.0, respectively. The relaxation of atoms on the two planes on either side of the cut is significant, especially that of the impurities: the relaxed S atoms move outwards away from the exposed surface by 0.41 Å with respect to the three Ni atoms that are allowed to relax, and by 0.18 Å with respect to the fixed reference Ni atom.

3.4.3 Generalized-stacking-fault energy for bulk Ni

For the calculations of the generalized-stacking-fault energy, care has to be taken how the atoms are relaxed on the slip planes, as the supercell vector $\mathbf{a_3}$ is changed by $\mathbf{s}$ (see Fig. 3.3). We simulate the behavior of the bulk away from the slip plane by keeping the central plane of the supercell fixed. We allow relaxations along $\mathbf{a_3}$ but keep the positions of all slip plane atoms fixed along $\mathbf{a_1}$ and $\mathbf{a_2}$, while the remaining atoms are allowed to relax freely. These restrictions are crucial to ensure a meaningful representation of slip displacements that result in run-on configurations where atoms in the slip plane are directly on top of one another [88]. The resulting γ-surface for slip on the (111) plane is shown in Fig. 3.6 (a). The (111) plane contains the minimal path between two equivalent slip points. The total slip between two such points results in a dislocation with Burgers vector $\mathbf{b}$ along the $\langle 10\bar{1}\rangle$ direction, which can split into two partial dislocations with Burgers vectors $\mathbf{b_1} = \frac{1}{6}\langle 11\bar{2}\rangle$ and $\mathbf{b_2} = \frac{1}{6}\langle 2\bar{1}\bar{1}\rangle$. Along these directions, the minimal energy barrier γ_{us} occurs at a relative displacement of $0.6\sqrt{6}a$Å (see Fig. 3.6 (a)); the slip energy along $\langle 11\bar{2}\rangle$ is shown in Fig. 3.7 (a). The

intrinsic stacking fault energy obtained from this calculation is $\gamma_{sf} = 0.143$ J/m^2, in good agreement with experimental results (0.125 J/m^2 [102]).

We performed convergence tests with respect to the size of the supercell in the $\mathbf{a_3}$ direction by increasing the size to 4 units along the $\mathbf{a_3}$ direction, which gave a difference of less than 1% to the results mentioned above. To confirm that the substitutional S atoms did not distort the supercell significantly we performed relaxations along $\langle 111 \rangle$ in the case of added impurities. This resulted in a change in $\mathbf{a_3}$ of less than 1% for both $\Theta = 0.33$ and 1.0. Table 3.2 shows the values of the unstable stacking energy, γ_{us}, for the case $\Theta = 0.0$, 0.33 and 1.0 on the slip plane: the presence of S produces a decrease in γ_{us} by 41% and 66% for $\Theta = 0.33$ and 1.0, respectively. This indicates that a slip becomes more favorable with increasing impurity concentration. In the context of Griffith cleavage, the decohesion energy results presented in section 3.4.1 suggested that the material should become more brittle since the energy barrier for creation of new surfaces decreases considerably as impurities are added. This is outweighed by the changes in the unstable stacking energy. The ductility parameter D increases by 24% and 41% for $\Theta = 0.33$ and 1.0, that is, with added S impurities bulk Ni actually should become more ductile. This is not seen in experiments when S impurities are added to Ni. These results already suggest that Ni embrittlement cannot be due to S incorporation in the bulk, but that instead other processes are dominant.

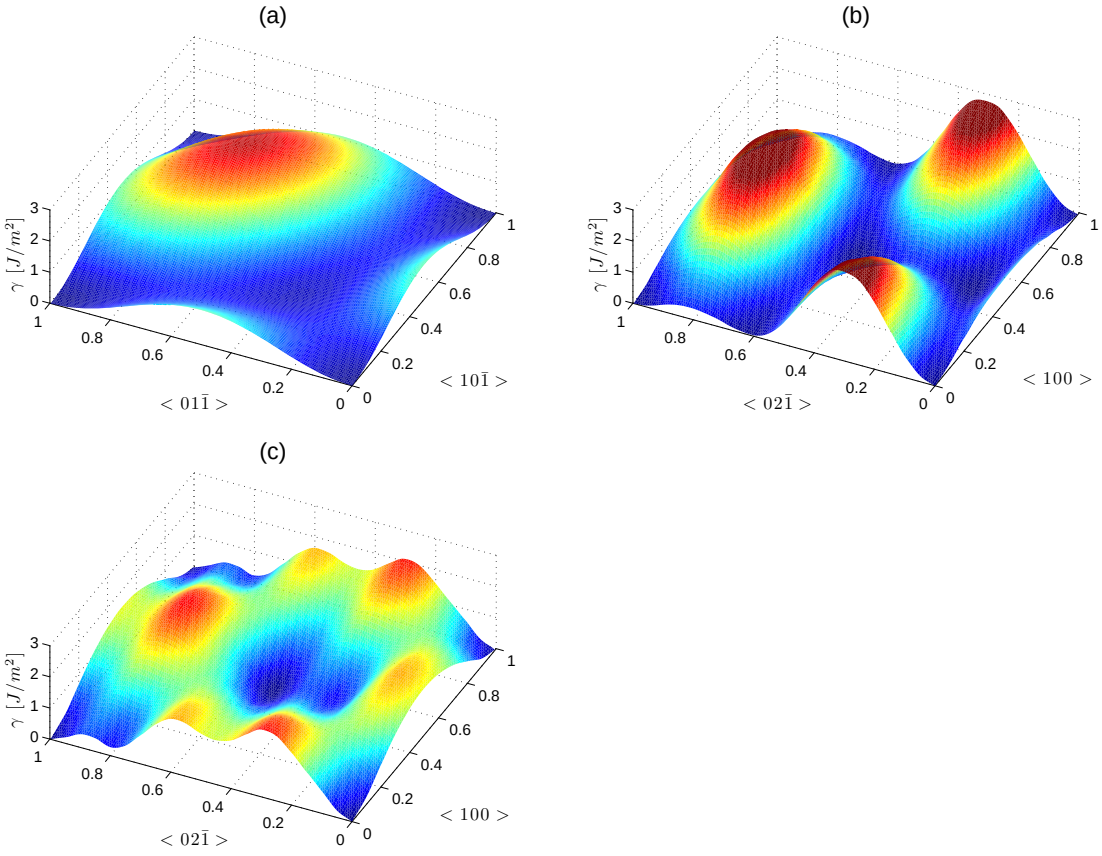

Figure 3.6: (a) Generalized-stacking-fault energy for slip on the (111) plane of bulk Ni (see text for details). The lowest energy path between equivalent points on the slip plane lies in part along the diagonal direction in the plot; a displacement along this direction results in a partial dislocation with Burgers vector $\mathbf{b} = \frac{1}{6}\langle 11\bar{2}\rangle$. (b) Generalized-stacking-fault energy for $\Sigma 5(012)$ GB in pure Ni and (c) in Ni with 4 interstitial S atoms on the GB plane (GB0), corresponding to $\Theta = 1.0$.

3.4.4 Generalized-stacking-fault energy at a grain boundary

To model the resistance of a Ni GB against shear, we calculate its generalized-stacking-fault energy. We use the same structure as in section 3.4.2, but now displace all atoms of one of the two half-crystals, defined by a cut between GB0 and GB1, by a slip vector **s** (Fig. 3.5). As in the case of the generalized-stacking-fault energy calculations for bulk Ni, we relax the atoms of the slip plane in the $\mathbf{a_3}$ direction only and keep them fixed along $\mathbf{a_1}$ and $\mathbf{a_2}$; this allows us to define the slip vector **s** properly. Note that such a slip displacement defines two interfaces under our periodic boundary conditions: the first at GB0 and the second at GB10. Accordingly S impurities were added to both these planes in a symmetrical fashion. We again simulate a bulk layer by holding the center-most two planes between the two GB's fixed.

The γ-surface of the GB without S impurities is shown in Fig. 3.6 (b). The three maxima in the energy surface correspond to run-on configurations of the Ni atoms in the GB0 and GB1 planes (compare to Fig. 3.5). A displacement by a slip vector $\mathbf{s} = \frac{a}{10}\langle 52\bar{1}\rangle$ leads to a configuration that is geometrically equivalent to the initial GB structure. The maximum energy of the minimal energy path (see Fig. 3.7 (b)) between these two geometrically equivalent points, corresponds to the unstable stacking energy $\gamma_{us} = 0.30$ J/m^2, which is almost the same as for the case of pure bulk Ni.

When impurities are added to the interstitial sites, the symmetry of the GB plane is altered and the possible slip vectors leading to minima in the γ-surface change. We

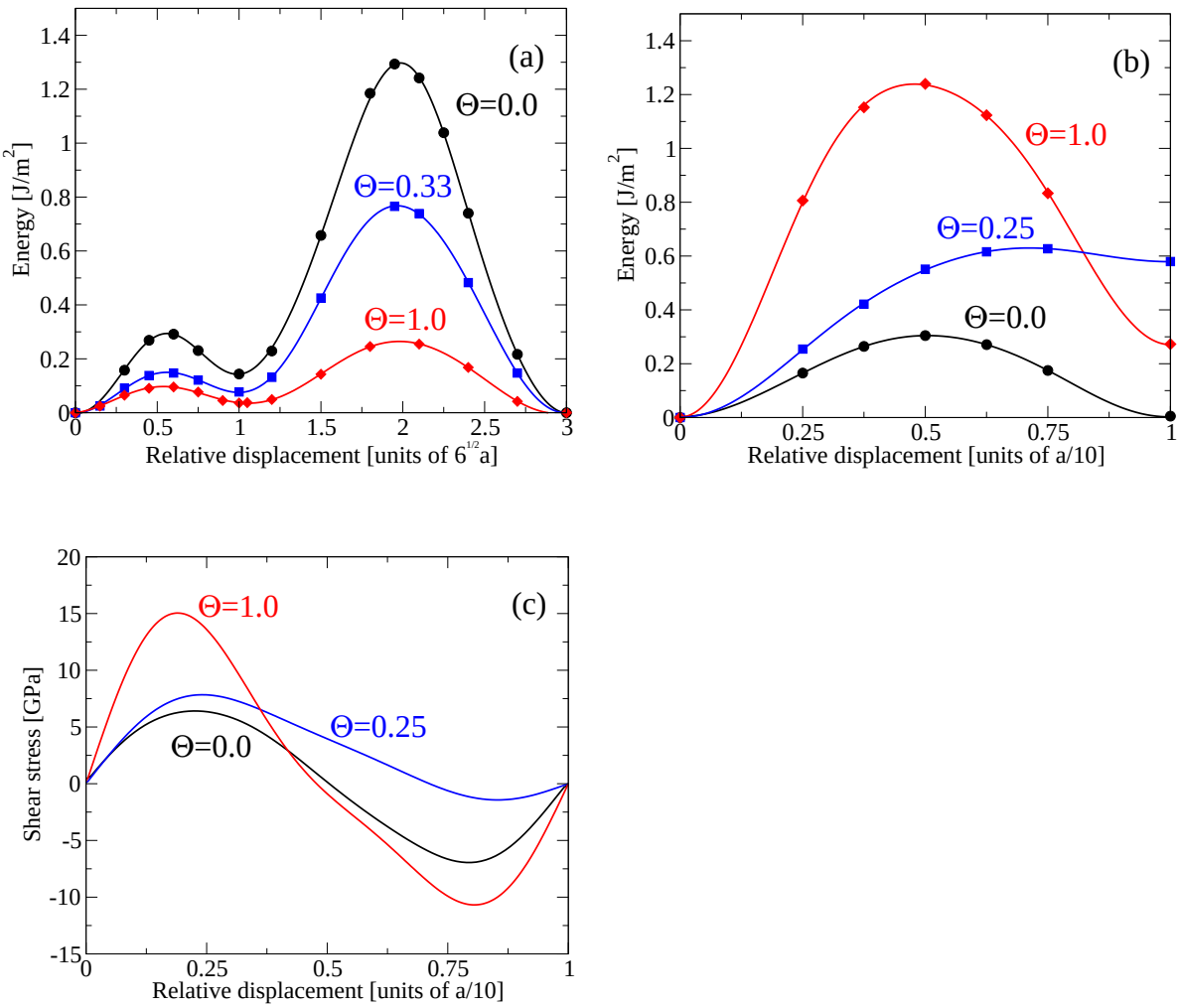

Figure 3.7: (a) The generalized-stacking-fault energy along the $\langle 11\bar{2}\rangle$ path for slip on the (111) plane of bulk Ni, without ($\Theta = 0.0$) and with ($\Theta = 0.33$ and 1.0) S impurities. The relative displacement is in units of $\sqrt{6}a$, where a is the bulk lattice constant. The unstable stacking energy, γ_{us}, occurs at a relative displacement of $0.6\sqrt{6}a$. (b) The generalized-stacking-fault energy for the $\Sigma 5(012)$ GB, without ($\Theta = 0.0$) and with ($\Theta = 0.25$ and 1.0) S impurities. The relative displacement is in units of $\frac{a}{10}$ along $\langle 52\bar{1}\rangle$ for $\Theta = 0.0$ and 0.25 and in units of $\frac{a}{10}$ along $\langle 56\bar{3}\rangle$ for $\Theta = 1.0$. (c) The corresponding shear stress for the GB.

have performed separate γ-surface calculations for structures with one ($\Theta = 0.25$) and four ($\Theta = 1.0$) interstitial S atoms on the GB plane, and determined the minimal energy path between equivalent points. For $\Theta = 0.25$, the minimal energy path follows the slip vector $\mathbf{s} = \frac{a}{10}\langle 52\bar{1}\rangle$; this is the same as for $\Theta = 0.0$. When all interstitial sites on the GB plane are filled with S impurities ($\Theta = 1.0$), the direction to the nearest local minimum changes such that the minimal energy path now occurs along $\mathbf{s} = \frac{a}{10}\langle 56\bar{3}\rangle$ (Fig. 3.6 (c)). Due to the change of geometry of the GB plane when impurities are added, the slip vectors are now associated with partial GB dislocations. The respective minimal paths are plotted for $\Theta = 0.0$, 0.25 and 1.0 in Fig. 3.7 (b). In contrast to the results for the bulk crystal, the value of γ_{us} increases with impurity inclusion (Table 3.2). We can see from these results that GBS is suppressed with S impurity inclusion at the GB. Since GBS is a dominant process of plastic deformation in nc metals, this strongly suggests that such materials would behave less ductile when S segregates to the Ni GB's. The almost two- and four-fold increase in γ_{us} for $\Theta = 0.25$ and 1.0 results in a decrease of 59% and 85%, respectively, for the value of the ratio D^{GB} between the work of separation W_s and the unstable stacking energy γ_{us} (see Table 3.2). This means that our results for the changes in W_s in combination with our findings for the shear behavior indicate that for a given individual GB interface we expect the mechanical behavior to change from a more ductile response involving GBS to a more brittle response involving cleavage along the GB.

In order to take into account changes in the minimal energy path with S inclusion,

planes	θ	$\tilde{D}_0^{GB}$	$\tilde{D}_1^{GB}$	$\tilde{D}_0^{GB}/\tilde{D}_1^{GB}$
$[(01\bar{2}),(012)]$	53.1°	0.658	0.330	2.0
$[(120),(012)]$	66.4°	2.846	0.532	5.4
$[(210),(012)]$	78.5°	0.658	0.424	1.6
$[(0\bar{2}1),(012)]$	90.0°	0.642	0.322	2.0

Table 3.3: The values of the ductility parameter $\tilde{D}^{GB}$ when the geometry change between $\Theta = 0.0$ ($\tilde{D}_0^{GB}$) and 1.0 ($\tilde{D}_1^{GB}$) is considered. The angle between the two possible Burgers vectors is $\Delta\phi = 29.21°$. θ is the dihedral angle between the slip and decohesion plane.

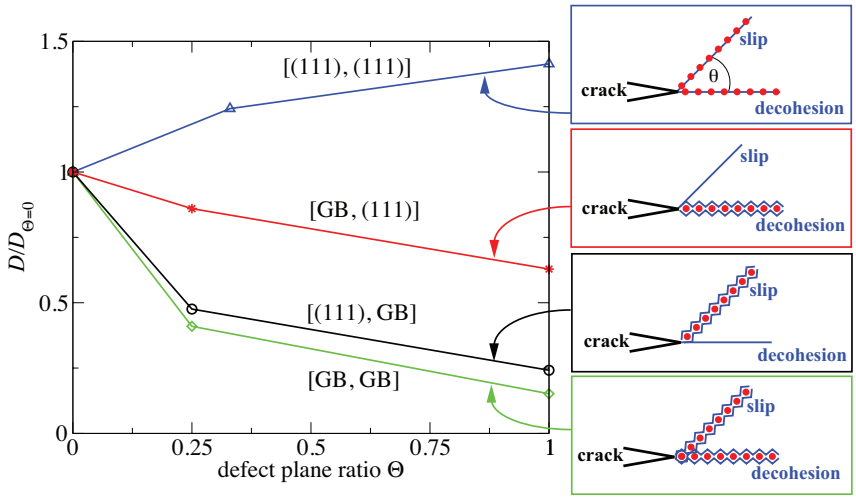

Figure 3.8: Normalized ductility parameter $D/D_{\Theta=0}$ for bulk Ni and Ni with a $\Sigma5(012)$ GB. The four data sets shown are values of D for the relevant combinations of decohesion and slip planes, with labels [decohesion plane, slip plane] and their respective schematics to the right. The lines are guides for the eye.

we calculate a ductility parameter $\tilde{D}^{GB}$ that includes geometry changes based on Eq. (3.1) by considering the possible intersections of {012} planes for the two different Burgers vectors [1]. This is presented in Table 3.3. We find that for physically realistic configurations the behavior of $\tilde{D}^{GB}$ remains unaffected and the trends are the same as for the more simplified ductility parameter D^{GB}, that is, S inclusion significantly decreases the value of D^{GB}.

It is possible that the GB may provide a relaxation mechanism in combination with the (111) planes. We plot in Fig. 3.8 the normalized ductility parameter D of such physically reasonable configurations. In this comparison, we have left out the possible combinations that have S impurities on the (111) planes together with GB slip or decohesion, since we have already seen in Section 3.4 and Table 3.1 that the thermodynamically most stable positions of the S impurity atoms are at the GB, which are energetically preferred by 1.3 to 1.6 eV, depending on S coverage, over bulk planes. We first consider that the GB could serve as a decohesion plane in combination with a clean (111) plane as the slip plane. Such a geometry would be of importance for coarse-grained systems but also for materials with heterogeneous grains. Due to the decrease in W_s of the GB with S inclusion, the ductility parameter of such a geometry also decreases. We see that therefore this mechanism also changes to more brittle behavior resulting in preferential intergranular fracture. The GB could also serve as a slip plane with decohesion on the (111) planes. Although this process would

[1] We assume here that the Poisson ratio is unchanged and takes the value $\nu = 0.276$ [102].

likely result in blunting of any emerging (111) crack in the intrinsically ductile bulk Ni, it is possible that such blunting is not a dominant effect in nc and ufc materials. This process of transgranular failure will therefore still be considered. We again see a decrease in D^{GB}, implying preferential brittle behavior, since ductile behavior in the form of GBS becomes energetically less favorable. Overall this comparison shows that S impurity segregation at the GB defects results in a decrease in the ductility parameter for all combinations involving the GB.

We have shown that for a system where GB slip and GB decohesion are considered as competing processes, S impurities segregated to the GB plane result in an overall more brittle response. The question that still remains is if our results support an increase of intergranular fracture, that is, if a crack can more easily propagate along the grains. A simple model, similar in spirit to that in Ref. [77], illustrates a possible intergranular fracture mechanism. We first calculate the shear and tensile strengths, that is, the maximum of the derivatives of the relevant energy curves of Fig. 3.4(b) and 3.7(b) with respect to displacement. This is shown in Fig. 3.4(c) and 3.7(c) and summarized in Table 3.2. We see a small decrease in the tensile strength σ_t as S impurities are added to the GB. In contrast, the shear strength σ_s increases significantly. Although decohesion of the grains is preferred for S inclusion, a crack within this model can only propagate efficiently if GBS supports this. This is illustrated by the simple schematic of Fig. 3.1. If we assume that the force perpendicular to the cracked GB is equal to the critical value of the tensile strength, we find that for

all possible $\Sigma5\,(012)$ GB geometries the parallel forces required for sliding are larger than the critical shear strength. This implies decohesion, followed by sliding, leading to easy crack propagation. In contrast, when we add impurities the critical shear strength increases, and for $\Theta = 1.0$, two out of five possible geometries of our GB are now not supporting crack propagation anymore; intergranular crack propagation, at least when it is accommodated by GBS, is suppressed. Although our results for GBS suggest that this form of plastic deformation is suppressed with impurity inclusion at the GB, indicative of a more brittle behavior, this model predicts that the expected type of fracture behavior is not intergranular fracture. Several important points have to be made regarding these results. First, in our simple crack propagation model intergranular fracture accommodated by GBS is possible for the pure GB's. This does not imply intergranular fracture for pure nc Ni; instead we are limited to conclusions based on our $\Sigma5\,(012)$ GB which is a special GB and any sample in an experiment would be made up of a variety of GB's intersecting at various angles. Treating GB properties from first-principles calculations is notoriously difficult due to the unknown structure at the GB and the large unit cells required. Thus, performing calculations over many possible GBs is not feasible. As in most similar studies, we have considered here a single GB structure and explored the implications of having impurities in it, with the expectation that this gives useful insight to the behavior of such systems. We assume that other GBs that share structural features with the one we studied, such as adequate space to accommodate the impurity atoms at low-

energy positions, will exhibit similar behavior. We investigated only changes in the behavior of such special GB's as we add S impurities. For nc grains such intergranular fracture behavior has been predicted by classical MD simulations without any impurity inclusion [20]. Second, we found that a fracture mode accommodated by GBS is suppressed. This does not preclude intergranular fracture in general, as it applies only GBS related mechanisms. Cracking along the grain will still occur once the applied forces for the perpendicular components of the GB's exceed the continuously decreasing critical tensile strength. We can therefore anticipate a behavior where initially the suppression of GBS increases brittle behavior, making both intergranular and transgranular fracture possible. For increasing S impurity concentrations, a decreasing value of W_s would eventually lead to pure intergranular fracture. In the context of the competition between trans- and intergranular fracture, it is important to note that GB decohesion for $\Theta = 1.0$ gives a value of W_s which is almost half that of the decohesion energy for the (111) planes. This clearly makes GB decohesion and hence intergranular fracture an energetically preferred pathway.

The last issue we consider is the effect of S impurities on the crystalline order around the GB, which could be important in inducing fracture. This effect was first proposed by Heuer *et al.* [76] and computationally treated by Chen *et al.* [77]. They see that an amorphized GB results in a dramatic decrease in the shear strength as impurities are added, favoring immediate intergranular crack propagation as the GB is weakened both for cleavage and shear. Our results support the argument that this

is indeed necessary to facilitate easy intergranular fracture accommodated by GBS for the Ni and S system. A more detailed analysis of a system of very high S impurity concentration that leads to amorphization of the GB region is beyond the scope of the present approach.

3.5 Conclusion

We have performed a first-principles DFT study of the mechanical behavior of fcc Ni in the presence of S impurities. The differences between bulk fcc Ni and fcc Ni with a $\Sigma5(012)$ GB defect as S impurities are added were investigated. Low energy interstitial positions for the S impurity atoms at the GB are the stable sites, versus the substitutional defect sites in the bulk fcc crystal. This already highlights the importance of GB's in chemical embrittlement and is consistent with the experimentally observed S segregation to GB's [73, 68, 69, 70, 74, 71, 72, 75, 76].

We employ Rice's theory to investigate changes in the ratio of the surface and the unstable stacking energy (the ductility parameter D) to quantify changes in the ductility. This approach is adapted to our system with a $\Sigma5\,(012)$ GB by considering the competition between GB decohesion and shear in the form of GBS. GB decohesion, indicative of brittle behavior, is quantified through the work of separation (W_s), whilst GBS, a mechanism of plastic deformation in nc metals, is quantified through γ_{us}, analogous to previous work on GB's in crystalline solids [78, 79, 80]. By considering the energy of dislocation nucleation in the bulk and of GBS for our GB, in

comparison to the decohesion energy and the work of separation, respectively, we are able to put this problem on a more complete and quantitative footing in the context of the competition between processes of cleavage and plastic deformation. Our calculations for the bulk defect-free structure indicate that an increase in ductility occurs as impurities are added. In contrast, we find that the resistance to shear, quantified by γ_{us}, increases for the GB structure. This limits plastic deformation and indicates a transition to brittle behavior, as this form of plastic deformation mechanism is removed. The effect of embrittlement persists when geometric factors are fully accounted for according to Rice's theory and when different combinations of slip and cleavage systems are considered. Although our results for the $\Sigma 5\,(012)$ GB show that GBS is suppressed with S impurity segregation, intergranular cracking facilitated by GBS in our simple geometric model does not become more preferred. We do not see the significant decrease of shear strength observed in MD calculations of amorphized GB's [77]; amorphization is important to enable easy intergranular crack propagation that is accommodated by GBS. Our results address the problem of a crystalline GB since analyzing an amorphous GB in the context of Rice's theory is not feasible. We show that even before any possible amorphization of the GB is considered, there is clear evidence for a significant decrease in ductility but not in the form of immediate intergranular fracture accommodated by GBS. This does not preclude intergranular fracture for large enough tensile forces, since the tensile strength decreases with the inclusion of S impurities. Any failure mode that relies on GBS is suppressed for the

GB system.

Chapter 4

An *ab-initio* concurrent multiscale method for metals

4.1 Overview

We present a multiscale method, coupling a small region treated by a first-principles quantum mechanical method to a larger region treated by classical atomistics, based on total energy arguments that are applicable to metals. In particular, we employ Kohn-Sham Density Functional Theory in the smaller region and couple this to the larger region which is treated with the classical Embedded Atom Method. We test the accuracy of our approach for two transition metals, Ni and Cu, with good results for both a standard fcc crystal and a more complicated system including chemical impurities at a grain boundary (GB). For the latter we study the average

interplanar strain surrounding the GB and use this as a measure of the atomic relaxation. We apply this method to investigate the chemical embrittlement of Cu by Bi and Pb impurities and compare this to the effect of Ag impurities which are known to segregate to the GB but not embrittle Cu. We find clear evidence for chemical embrittlement by Bi and Pb but not for Ag, when these atoms are added as impurities at the Cu GB, in the form of a significant decrease of both the work of separation, W_s, and tensile strength, σ_t.

4.2 Introduction

Over the last decades materials modeling has become of great importance in understanding real world systems. One of the central issues in modeling is finding the right balance between the required accuracy and the affordable computational cost. A promising avenue toward addressing this issue is the development of methods for coupling different regions of accuracy in a multiscale approach [6, 7, 8, 9, 10, 11, 12]. A prototypical example in which many length scales are important is the propagation of cracks in brittle fracture, often induced by chemical impurities. In this paper we will attempt to address a subset of issues related to this problem, that is chemical impurities at grain boundaries (GBs) of metals and how they may affect the physical and mechanical properties of the material. For systems with chemical impurities, quantum mechanical accuracy is needed to correctly capture bond breaking and formation. On the other hand, in order to gain understanding of the

large scale mechanical behavior, the region containing the impurities must be coupled effectively to a larger region where quantum mechanical accuracy is of little importance due to relatively small deviations from the ideal structure. We present here a concurrent multiscale method appropriate for such systems, in which Kohn-Sham (KS) Density-Functional-Theory (DFT) is coupled to the Embedded Atom Method (EAM), making it possible to maintain quantum mechanical accuracy where needed but keep the computational cost low. We present results that show that our model works for Nickel (Ni) and Copper (Cu) in the sense that for those metallic systems the different regions are coupled appropriately. This is achieved by comparing our multiscale results to the ideal fcc lattice to quantify how well-known structures are reproduced and by considering the vacancy formation energy as a measure of the accuracy of the energetics. We next apply our method to the more complicated system of chemical embrittlement of Cu, a metal used in a variety of technological applications that has recently gained importance particularly in the electronics industry. Cu has high thermal and electrical conductivity and is normally ductile. At the same time, it has been experimentally known for well over a century that Cu is subject to chemical embrittlement in the presence of common impurity elements, such as Bismuth (Bi) and Lead (Pb) [14]. This is thought to be related to the segregation of these impurities to GBs [13, 103, 104, 105]. The fundamental mechanism involved in chemical embrittlement of metals is in general not fully understood and has been subject to several theoretical and computational studies. Rice and Wang [106] identified

the work of interfacial separation as an important quantity to measure the potential for chemical embrittlement and proposed a competing relationship with the energy release rate of dislocation nucleation, G_{d}. They also discussed the importance of the stress *vs.* separation relation and its maximum, the tensile strength, in crack nucleation. Several recent *ab-initio* studies have addressed important issues concerning the chemical embrittlement of Cu [107, 108, 109, 110]. Schweinfest *et al.* [107] and Lozovoi *et al.* [108] investigated the effect different impurities have on the Cu GB using DFT calculations and proposed that chemical embrittlement can be explained by a theory based on size effects. They used energy arguments relying on the theoretical work of Rice and Wang [106] and Rice [84] to study a $\Sigma 5$ and $\Sigma 19$ GB to address the issue of chemical embrittlement. Geng *et al.* [111] used a first-principles based phenomenological theory and proposed that chemical contribution is also important in addition to the size effect. In the present work we employ the *ab-initio* multiscale method mentioned above to study a $\Sigma 5\,(012)$ Cu GB with Bi, Pb and Ag impurities. The multiscale approach allows us to capture long-range effects and we consider the strain behavior as we change the composition of the grain boundary. To this end we demonstrate a method to relax the system into a physically sensible state by relaxing the strain efficiently for atoms far away from the GB. This allows us to get reliable values for the GB expansion of the Cu GB system with impurities. Such GB expansion caused by impurity inclusion at the GB has been previously reported for the Cu system [107, 108] and has been identified as a sign of weakening the GB in the context of

chemical embrittlement of metals [78, 107, 108, 112]. We further address the influence that chemical impurities have on the Cu GB by considering the work of separation, W_s, and the tensile strength, σ_t, of the $\Sigma5\,(012)$ GB. Both W_s and σ_t are directly linked to the cleavage properties of the metal-impurity system since they quantify the propensity of GBs to fail via intergranular fracture [78, 84, 106, 107, 108, 112]. We show evidence of chemical embrittlement for Bi and Pb in Cu in the form of a significant decrease in both W_s and σ_t. As a reference, we also consider Ag impurities which are known to segregate to the GB but do not embrittle Cu [108]. We do not find evidence of the same type of embrittlement as for Bi and Pb impurities; instead the behavior in the presence of Ag impurities changes little in comparison to the pure Cu GB.

The chapter is organized as follows. In Section 4.3 we discuss the theoretical background of the multiscale method, coupling KS-DFT to the EAM, for metal systems with defects and discuss the specifics of our computational model. Section 4.4 presents test calculations showing the validity of our implementation of the multiscale method. This is followed by a study of chemical embrittlement due to impurities at a GB in Cu in Section 4.5. Finally, in Section 4.6 we summarize our results and discuss our conclusions.

4.3 Theoretical background

In order to address large system size effects we have implemented a multiscale method based on first-principles DFT calculations in the small region where quantum mechanical treatment is of importance, coupled to the rest of the system which is treated by the EAM. This allows us to increase the number of atoms we are able to consider from a few hundred in DFT calculations. Typical quantum-mechanical to molecular mechanics (QM/MM) methods are developed for covalently bonded structures, with the coupling relying on the presence of additional or fictitious link atoms on the MM side. Such an approach is not needed in the present formulation which is expressed in terms of different contributions to the total energy of the whole system, and its derivatives with respect to atomic positions which give the forces. This method was originally developed using Orbital-Free DFT (OF-DFT) [113]. Here, we instead implement the multiscale method using KS-DFT, where the kinetic energy is known exactly in terms of single-particle orbitals. This choice of computational method for the QM region offers several advantages over OF-DFT: First and foremost, it allows treatment of transition metals like Cu and Ni (the focus of the present study) whereas OF-DFT is often limited to main group metals [114, 115]. There have been attempts to create appropriate local pseudopotentials and special kinetic energy density functionals for transition metals recently, but these are still limited in their applicability and lack easy transferability. It is also not clear how well these very recent OF-DFT methods would perform for impurity inclusion as they are found to

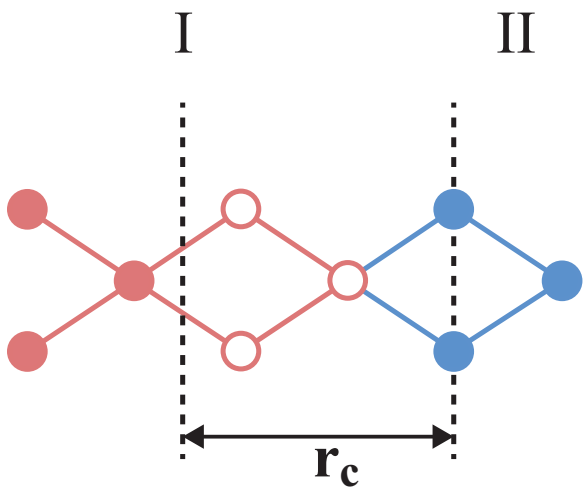

Figure 4.1: Schematic illustration of the multiscale coupling across the DFT/EAM boundary. Blue circles represent atoms in region II and are calculated using EAM only; red circles represent atoms in region I, where filled circles have a net force only from DFT calculations and empty circles have force contribution both from DFT and EAM. Forces between nearest neighbor atoms are shown as solid lines, red for DFT and blue for EAM. The sub-region contained within region I, which is within the EAM cutoff radius, r_c, of the nearest region II atom, is shown delimited by vertical dashed lines.

be of limited accuracy for alloy systems [116]. An additional complication is that the multiscale approach is best implemented with a method allowing for non-periodic boundary conditions; this will be discussed in greater detail below. Although there are non-periodic approaches to OF-DFT [117], this is not trivial. In contrast, numerous choices exist for accurate treatment of non-periodic boundary conditions within KS-DFT [118, 119, 120]. We implement our multiscale method in the framework of a well-established KS-DFT code, which offers the advantages of versatility and transferability beyond the specific systems studied in the present work.

We discuss next the theoretical basis of the multiscale approach and provide a

description of how coupling across regions is accomplished. The supercell is divided into two regions, I and II, where region I requires quantum mechanical accuracy and is coupled to region II which involves classical interaction between atoms, treated by the EAM. The total energy is in general given by

$$E\left[\mathrm{I}+\mathrm{II}\right]=E_1\left[\mathrm{I}\right]+E_2\left[\mathrm{II}\right]+E^{\mathrm{int}}\left[\mathrm{I},\mathrm{II}\right], \tag{4.1}$$

where, $E_1[\mathrm{I}]$ and $E_2[\mathrm{II}]$ are the total energies in regions I and II with their respective calculation methods 1 and 2, and E^{int} is the interaction energy associated with coupling the two regions. We can classically approximate this interaction energy by calculating each term using the EAM [113]:

$$E^{\mathrm{int}}\left[\mathrm{I},\mathrm{II}\right]=E_{\mathrm{EAM}}\left[\mathrm{I}+\mathrm{II}\right]-E_{\mathrm{EAM}}\left[\mathrm{I}\right]-E_{\mathrm{EAM}}\left[\mathrm{II}\right]. \tag{4.2}$$

Taking method 1 for region I to be KS-DFT and method 2 for region II to be the EAM, it is possible to show that the total energy of our system can be written as

$$E\left[\mathbf{R^{tot}}\right]=E_{\mathrm{EAM}}\left[\mathbf{R}^{\mathrm{tot}}\right]-E_{\mathrm{EAM}}\left[\mathbf{R^{I}}\right]+\min_{\rho^{\mathrm{I}}}E_{\mathrm{DFT}}\left[\rho^{\mathrm{I}},\mathbf{R^{I}}\right], \tag{4.3}$$

where $\mathbf{R}^{\mathrm{tot}}$, $\mathbf{R}^{\mathrm{I}}$ and $\mathbf{R}^{\mathrm{II}}$ are the coordinates in the respective regions and ρ^{I} is the electron density for the DFT calculation. The coupling between region I and II and the origin of forces on individual atoms is illustrated in Fig. 4.1. We show the different force contributions from nearest neighbor atoms only. Next-nearest neighbor interactions and those farther away are not shown for clarity, but are based on the same principles. Forces in region II are only based on the EAM, indicated as blue lines

connecting the blue filled circles representing the atoms in region II. The coupling is due to the EAM forces across the EAM/DFT boundary; this is a direct result of approximating the interaction energy classically with the EAM. For atoms in region I that are farther away than r_c (the EAM cutoff radius) from the boundary separating the two regions, the forces are based solely on DFT; these atoms are drawn as filled red circles with red lines indicating forces based on DFT. For atoms that are within a distance r_c from the nearest region II atom, the net force is the sum of DFT contributions and the interaction correction $E_{\mathrm{EAM}}[\mathbf{R}^{\mathrm{tot}}] - E_{\mathrm{EAM}}[\mathbf{R}^{\mathrm{I}}]$. This involves DFT interactions with all region I atoms, and forces based on the EAM with atoms in region II that are within r_c. These atoms are shown as empty red circles in Fig. 4.1. This approach is general and can be used for any type of system that requires quantum mechanical accuracy only in a small region of the total. Our example of a GB defect with impurity atoms is shown in Fig. 4.2.

We have chosen to employ QUICKSTEP (QS) [61] in our implementation of the multiscale code. This code, available in the suite of programs CP2K [3], is based on mixed Gaussian Plane Waves (GPW) [62]. This is well suited for our multiscale method since the isolated center region I is non-periodic. Typical plane wave (PW) based DFT codes would require that a significant portion of the supercell consists of vacuum. This is computationally expensive and can lead to spurious results due to image effects if the size of the vacuum is not carefully converged. We circumvent this problem within the GPW formalism of CP2K by specialized poisson solvers, which al-

low for fast convergence and accurate results, free of boundary effects [118, 119, 120]. The implementation is not limited to the 2D periodicity described in this work. The exact XC energy is approximated by the PBE generalized gradient approximation [28], while separable and norm-conserving GTH pseudopotentials are used to describe the interactions between the valence electrons and the ionic cores [30, 31]. Convergence for Ni and Cu requires a density cutoff of 575 and 525 Ry, respectively. An important point to highlight is that the impurity atoms in our implementation are treated by DFT only. Therefore, a classical EAM potential for the impurities is not required. This is a great advantage, since constructing classical potentials that accurately describe the interaction between different types of atoms is exceedingly difficult and time-consuming. The EAM potentials we use for our metal atoms are based on a potential by Mishin *et al.* [121] for Ni and the EAM1 potential by Mishin *et al.* [122] for Cu. In order to ensure that we minimize any adverse effects at the boundary between the EAM and DFT, we have chosen to rescale the EAM potential so that the lattice constant (a_0) and bulk modulus (B) exactly match those of the DFT calculation, which in the case of Ni and Cu were determined to be $a_0\,(\text{Ni}) = 3.54$ Å, $B\,(\text{Ni}) = 201.1$ GPa and $a_0\,(\text{Cu}) = 3.67$ Å, $B\,(\text{Cu}) = 131.3$ GPa, respectively. Table 4.1 shows the energies of important structures and the elastic constants for DFT, the EAM in its original form from references [121] and [122] and the rescaled EAM for each case. The specific shear displacements to calculate the elastic constants are reproduced in Appendix A for completeness. The rescaling did not adversely affect the

	Ni				Cu			
	DFT	r-EAM	o-EAM	Exp.	DFT	r-EAM	o-EAM	Exp.
a_0 [Å]	3.542	3.542	3.520	3.52^a	3.669	3.669	3.617	3.61^a
B [10^{11} Pa]	2.011	2.011	1.720	1.86^a	1.313	1.313	1.372	1.37^a
C_{11} [10^{11} Pa]	2.821	2.802	2.376	2.481^b	1.725	1.660	1.75	1.683^b
C_{44} [10^{11} Pa]	1.299	1.484	1.291	1.242^b	0.918	0.740	0.779	0.757^b
C_{12} [10^{11} Pa]	1.861	1.775	1.548	1.545^b	1.254	1.187	1.253	1.221^b
$\gamma_s^{(100)}$ [J/m^2]	2.271	1.956	1.884	-	1.589	1.339	1.390	-
$\gamma_s^{(012)}$ [J/m^2]	2.583	2.285	2.194	-	1.772	1.530	1.587	-

Table 4.1: Summary of the elastic constants and relevant structural energies for Ni and Cu, obtained with DFT, the EAM rescaled to fit our DFT results (r-EAM), and the EAM in its original form (o-EAM) [121, 122]. Experimental values from a :Ref. [124], b :Ref. [41].

performance of the EAM potential and for Ni changed the results for the energies and elastic constants to be closer to the DFT results. By appropriately defining the forces of our system as the derivative of the total energy, which includes contributions from the EAM and DFT regions, we can apply all the structural relaxation techniques commonly employed. In particular we employ either the conjugate gradient or the Broyden-Fletcher-Goldfarb-Shanno (BFGS) quasi-Newton method [123], and unless otherwise stated, relax all forces to a magnitude less than 0.01 eV/Å.

4.4 Test Calculations

We test the accuracy of our multiscale method using a periodic supercell which is a $4 \times 4 \times 16$ multiple of the cubic fcc cell, and contains 1024 atoms. The center-most 7 planes in this setup (see Fig. 4.2) were calculated by DFT, that is a total of 224 atoms.

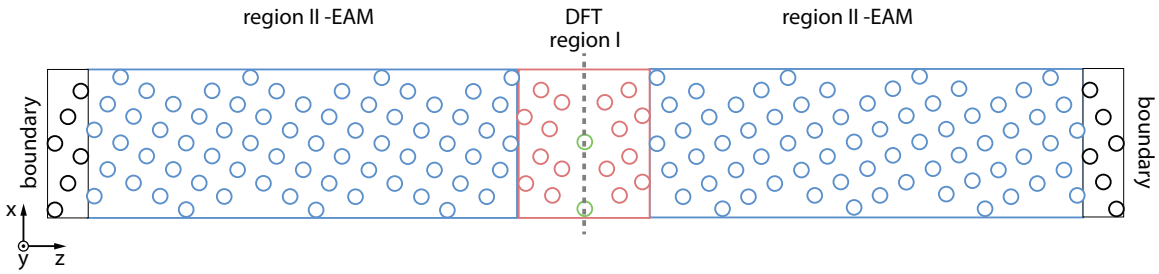

Figure 4.2: Schematic representation of the multiscale system: region I may contain defects (e.g. the $\Sigma 5\,(012)$ GB shown), impurities or just be part of the bulk crystal for test calculations. Blue circles represent metal atoms calculated using EAM only, red circles represent metal atoms treated by DFT. Green circles represent either host atoms at the GB plane or substitutional impurity atoms. The black boundary circles represent atoms that are either fixed or periodic images along z. The grey dashed line shows the position where the cell is split in two halves for the work of separation, W_s, calculations.

To quantify how well the DFT region is matched to the EAM region we consider two properties: 1) the forces before any relaxations and 2) the distance between the ideal fcc positions in comparison to their position after relaxation, with all forces smaller in magnitude than 0.0026 eV/Å. The results of this comparison are summarized in Table 4.2. For both Ni and Cu the fcc lattice is well reproduced, suggesting that the coupling between region I and II is accurate and that the forces before relaxation are small enough to guarantee physically sensible results. Table 4.2 also shows previous results by Choly *et al.* [113]; the present work is a significant improvement to this earlier work which employed OF-DFT for the quantum mechanical region.

To get a quantitative measure of how well the matching performs in terms of

System	F^I_{max} [eV/Å]	F^I [eV/Å]	d^I_{max} [Å]	d^I[Å]	d^{II}_{max}[Å]
Ni (I=7 layers/II=25 layers)	0.316	0.171	0.037	0.023	0.037
Cu (I=7 layers/II=25 layers)	0.100	0.063	0.015	0.007	0.008
Al (32 atoms - region I)	$0.45^{(a)}$	$0.33^{(a)}$	$0.12^{(a)}$	$0.07^{(a)}$	$0.05^{(a)}$

Table 4.2: Deviation from the ideal fcc positions in the multiscale method. All forces were relaxed to be smaller in magnitude than 0.0026 eV/Å. The size of the supercells for the fcc calculations and the number of DFT layers are indicated. The results quoted from Choly *et al.* [113] are based on a method that employed OF-DFT for the quantum mechanical region. (a) Values for Al from: ref [113].

energetics we considered the vacancy formation energy, $E_f^{(\mathrm{v})}$

$$E_f^{(\mathrm{v})} = E^{(\mathrm{v})}(n-1) + \frac{E_0(n)}{n} - E_0(n), \tag{4.4}$$

where $E^{(\mathrm{v})}(n)$ is the total energy with a vacancy, $E_0(n)$ is the total energy of a bulk fcc calculation and n is the number of atoms in the system. This is straightforward for a DFT calculation, the only issue being that the values for $E^{(\mathrm{v})}(n-1)$ and $E_0(n)$ should be based on the same supercell size and computational parameters. For the multiscale calculations the second term in Eq.(4.4) has to be approximated by a full DFT calculation to get the energy of a bulk atom. The results for a fixed vacancy for both Cu and Ni are summarized in Table 4.3. The aim here is to get an estimate of the error associated with energies rather than to evaluate the vacancy formation energy of Cu and Ni accurately. Long-range relaxation effects that are dependent on system size [125] may adversely affect this analysis and were hence eliminated by holding all atom fixed. We consider the level of agreement between the different results to be very satisfactory for energy comparisons of physical relevance.

		Cu	Ni
I	II	E_f^{V} [eV]	E_f^{V} [eV]
256	0	1.38	1.59
224	800	1.34	1.63
416	608	1.44	-

Table 4.3: Vacancy formation energy for Cu and Ni calculated for fixed atomic positions.

4.5 Application to chemical embrittlement

To address the issue of chemical embrittlement at GBs we study the effect that Bi, Pb and Ag impurities have on the $\Sigma 5\,(012)$ Cu GB. The impurities are placed as substitutional defects on the GB plane as in previous work with similar GB structures [107, 108]. We choose one monolayer (ML) coverage, which is consistent with experimental observations for the Cu system [13]. The geometry of the calculations is shown in Fig.4.2. Of particular importance is the long-range behavior away from the GB plane when impurities are added, which can result in GB expansion in most cases [78, 107, 108, 112]. In previous work using only DFT, relatively small supercells were employed; this approach allows the determination of the minimum energy structure using conventional methods like the Birch-Murnaghan equation [126]. In this work, we have performed calculations with 201 planes parallel to the GB and 16 atoms per plane, that is, a total of 3216 atoms. To ensure that the structure is in a physically sensible state, proper care must be taken to relax the inherent stress due to the presence of impurities or defects. Calculations that minimize the energy as a

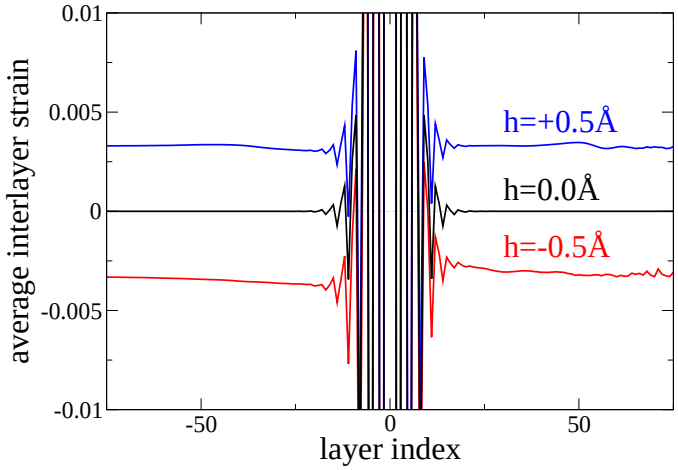

Figure 4.3: Average interplanar strain for pure Cu for different supercell sizes. The strain for compression/expansion, by 0.5 Å of the lattice vector perpendicular to the GB plane in comparison to a strain-relaxed structure is shown.

function of cell volume would be prohibitively expensive and not feasible for this case. Instead, we develop a scheme to find the physically most reasonable structure by successive strain relaxations. This has been added to the full relaxation step of region II of the method of Choly *et al.* [113] to efficiently relax the two different regions. We define the average interlayer strain,

$$\bar{\epsilon} = \frac{d - d_0}{d_0}, \tag{4.5}$$

where d is the relaxed interplanar distance and d_0 is the ideal interplanar distance for a perfect fcc structure. We relax the bulk strain by successively intergrating the strain in region II and appropriately increasing the supercell size. This method works very well for our system since we are dealing with a two-dimensional defect. We fix the

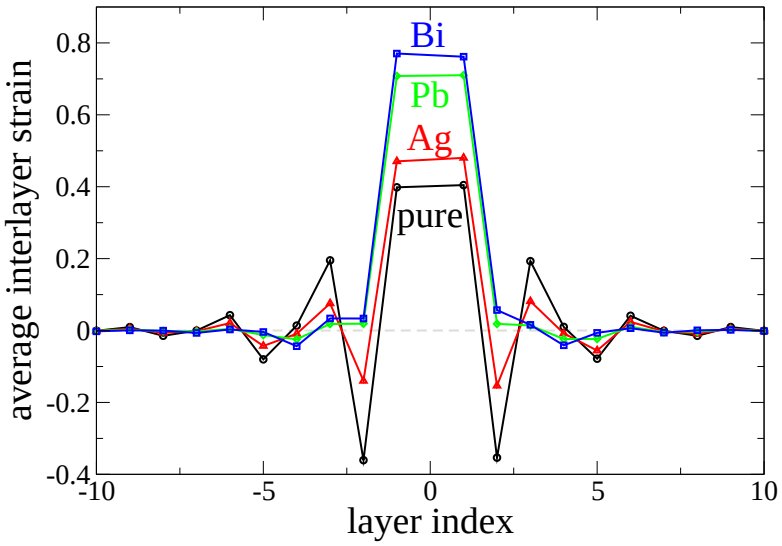

Figure 4.4: Interlayer strain of the $\Sigma 5\,(012)$ GB for Pb, Bi and Ag substitutional impurities and a clean GB. Note that the majority of the distortions with respect to the ideal fcc positions occurs very close to the GB plane for the cases of Pb and Bi, whereas it is more spread out for pure Cu and Cu with Ag.

outermost 10 layers on each end of the supercell and employ non-periodic boundary conditions for region II. This allows us to compress, expand or shear the two grains. The strain of a fully relaxed Cu GB is shown in Fig. 4.3. For compression, we also include the cases where the supercell is compressed or expanded by 0.5 Å, which shows the strain build-up over the entire cell.

The supercell contains 11 layers of DFT atoms, corresponding to a region I of size 16.41 Å ×14.68 Å ×8.48 Å. Convergence tests of up to 27 layers (16.41 Å ×14.68 Å ×21.65 Å) showed that the results change by less than 5%. As impurities are added to the GB plane the GB structure changes. We consider the distance between 30

	W_s [J/m^2]	σ_t [GPa]	d_{GB} [Å]
pure	2.65	16.2	0.0
Ag	2.45	15.5	0.263
Pb	1.52	9.1	0.820
Bi	1.38	7.7	0.940

Table 4.4: Work of separation, W_s, tensile strength, σ_t, and the GB expansion, d_{GB}, for a clean Cu $\Sigma5\,(012)$ GB with substitutional Ag, Pb and Bi impurities at the GB plane.

layers above and below the GB plane, and define the GB expansion, d_{GB}, as the change of this length as we add impurities. We list the respective values of the GB expansion in Table 4.4. The GB expansion, d_{GB}, is particularly large for Bi and Pb where we see an increase of the GB region by 0.82 Å and 0.94 Å, respectively. The GB expansion of Ag is much less, hinting at its smaller propensity to cause chemical embrittlement for the $\Sigma5\,(012)$ GB. This behavior is qualitatively similar to the GB expansion for a $\Sigma5\,(013)$ Cu GB reported by Lozovoi *et al.* [108]. Fig. 4.4 shows the associated average interlayer strain of the relaxed GB system. This illustrates why a multiscale approach with a sufficiently large number of layers parallel to the GB plane is necessary in comparison to the limited size of a DFT calculation. There is a considerable strain build-up that decays to zero over many layers away from the GB plane. Small supercells typically employed in DFT calculations may not capture this. The strain field reaches at least up to 10 layers into the bulk away from the center of the GB. That means a DFT calculation with standard periodic boundary conditions would require a supercell of 40 layers to effectively decouple the GB and its periodic

image, which would be computationally prohibitive. Our multiscale approach uses non-periodic boundary conditions and hence the size of region I does not have such strict size requirements. The strain build-up at the center of the GB for Bi and Pb impurities is significantly greater than for Ag impurities in comparison to the pure Cu GB and most of the strain and corresponding GB expansion occurs near the center of the GB for Bi and Pb.

This difference in the structural changes for the different impurities can be quantified further by considering the energetics of cleavage. We simulate cleavage by separating the GB at the center and rigidly displacing the two grains by a given distance, δ. Relaxations are allowed for all atoms except the cleavage plane atoms, which were held fixed. The cell size perpendicular to the GB plane is appropriately relaxed. Interlayer relaxations are dominant, whilst in-plane relaxations of the cleavage plane atoms are negligible and hence not included in calculations for the decohesion energy as a function of grain separation. In Fig. 4.5 (a) we show the decohesion energy as a function of δ for four systems, the pure Cu GB, Cu GB with Ag, Bi and Pb impurities. This set of results shows different behavior for the Bi and Pb impurities in comparison to the pure Cu GB or the Cu GB with Ag impurities. To quantify the potential of the different systems to fail in an intergranular fashion, we consider the work of separation, W_s, defined as,

$$W_s = E_\infty - E_0, \tag{4.6}$$

where E_∞ and E_0 are the total energies of the separated grains and the intact GB,

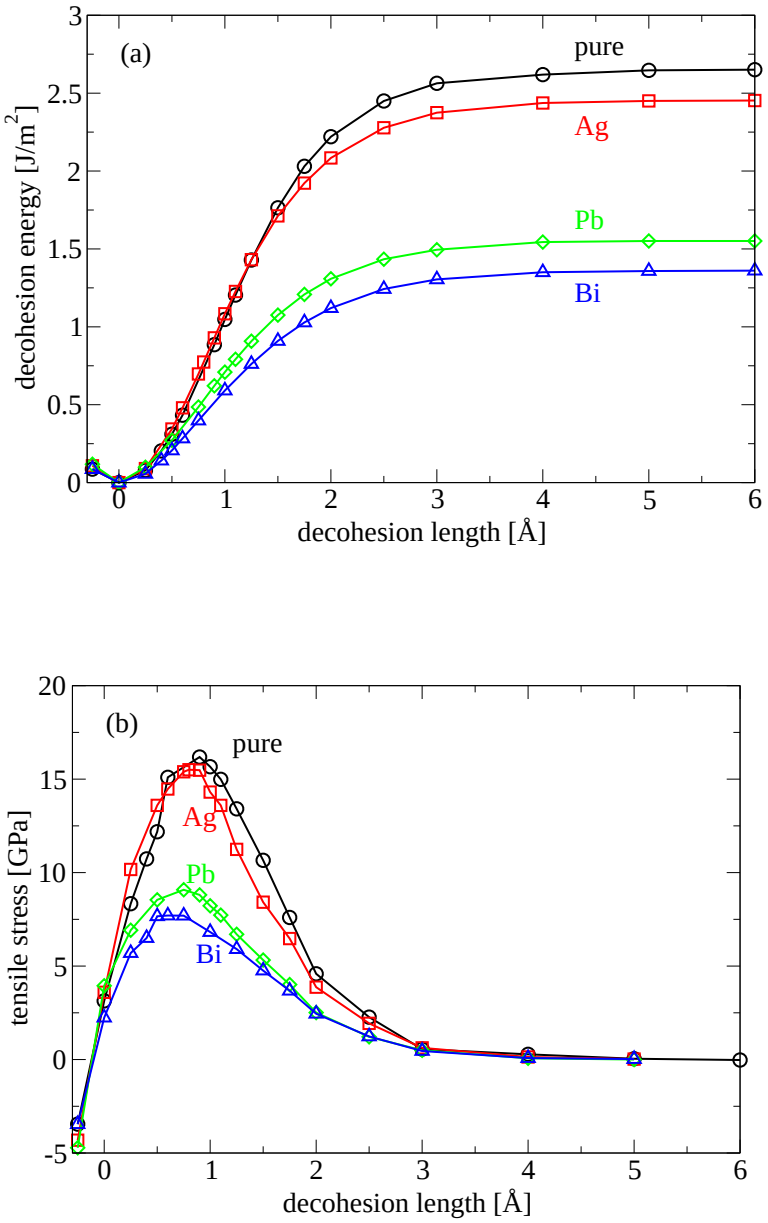

Figure 4.5: (a) Decohesion energy as a function of the decohesion length for the pure Cu GB (black circles), the Cu GB with Ag (red squares), Pb (green diamonds) and Bi (blue triangles) impurities (lines are guides to the eye). (b) Stress as a function of decohesion length for the pure Cu GB, the Cu GB with Ag, Pb and Bi impurities.

respectively. Pb and Bi induce a significant decrease of the work of separation in comparison to the pure Cu GB, by 1.13 J/m^2 and 1.27 J/m^2 or 43% and 48%, respectively. For Ag this decrease is only 0.2 J/m^2 or 7.5%. Since the work of separation is directly related to how easily a crack can spread along the GB interface [106], we conclude that intergranular embrittlement is greatly enhanced by the segregated Bi and Pb impurities, whereas Ag impurities have a negligible effect. The energy release rate for dislocation nucleation, G_{disl} [106, 84] for a typical Cu GB system lies in the range of $1 - 2$ J/m^2 [127]. Thus, the pure GB and that with Ag impurities has $G_{\text{cleave}} = W_s > G_{\text{disl}}$, whereas the addition of Bi or Pb impurities causes G_{cleave} to decrease leading to embrittlement.

As a second measure of intergranular fracture we consider the tensile strength, σ_t, as a function of impurity addition at the GB plane. This allows us to determine how easily a crack can nucleate at stress concentrations in the otherwise ductile Cu [106]. We calculate the stress, $\sigma(\delta)$, based on the decohesion energy curves of Fig 4.5(a) as the derivative with respect to the separation of the two grains. This is shown in Fig 4.5(b) with the tensile strength listed in Table 4.4. The tensile strength decreases by a very small amount, 4.3%, when Ag impurities are added, but Pb and Bi impurities reduce σ_t by 44% and 52%, respectively. We therefore see that both crack nucleation and the spreading of such a crack along the GB interface becomes easier when Bi and Pb are added to the GB. In contrast Ag impurities have only a minimal effect on either quantity.

4.6 Discussion and Conclusion

We have demonstrated a multiscale method based on a classical approximation of the interaction energy to efficiently couple the region treated by KS-DFT with the region surrounding it which is treated by the classical EAM. We have only dealt so far with geometry optimization based on CG and BFGS but our implementation in its current form also allows for ab-initio molecular dynamics (MD) and Car-Parrinello-like MD [128]. The method was tested for the bulk fcc structure and the vacancy formation energy for both Ni and Cu. We show that the strain behavior at a defect such as a GB can reach far into the bulk and hence larger supercells with a multiscale approach are necessary to properly capture the properties of the system and provided a method for efficiently relaxing the strain to obtain a physically sensible structure. We use our method to study the chemical embrittlement of Cu by impurity segregation at the GB plane. We find that the GB expansion observed for Bi and Pb is significantly greater than that for Ag impurities. This is further quantified by considering the work of separation, W_s, which decreases significantly for both Bi and Pb. This indicates that the likelihood that an existing crack spreads along the interface increases when Bi and Pb are added to the GB. In contrast, our calculations for Ag, do not show this dramatic decrease in W_s. The work of separation for Ag impurities remains such that $W_s = G_{\text{cleave}} > G_{\text{disl}}$, the energy release rate for dislocation nucleation, whereas $G_{\text{cleave}} \approx G_{\text{disl}}$ when Pb and Bi impurities are added to the Cu GB. We also consider the stress as a function of grain separation, $\sigma(\delta)$, and the

tensile strength, σ_t. The tensile strength of the pure Cu GB and the Cu GB with Ag impurities is very similar in magnitude. In contrast the tensile strength for Pb and Bi decreases by 44% and 52%, respectively, relative to the pure case. This suggests that cracks are more likely to nucleate at stress concentrations when Bi and Pb are present at the GB plane.

Chapter 5

The physics of impurities at copper grain boundaries

5.1 Overview

We investigate the changes in the mechanical properties of copper (Cu), when bismuth (Bi), lead (Pb) and silver (Ag) substitutional impurity atoms are added to the $\Sigma 5\,(012)$ symmetric tilt grain boundary (GB). We employ a concurrent multiscale approach, coupling a small region containing the GB with the impurities, calculated with density functional theory (DFT), to a large region containing the bulk metal around the GB, calculated with the embedded atom method (EAM). We first study the segregation behavior of the impurities by determining the impurity formation energy in the vicinity of the GB and find the energetically most beneficial sites are

on the center GB plane. We study grain boundary sliding (GBS) and intergranular decohesion as mechanisms of plasticity and brittle cleavage, respectively. All impurities are found to strongly inhibit GBS. Mechanical size effects are found to be of great importance when Bi and Pb are included at the GB. Ag is found to be the strongest inhibitor of GBS; this can be traced back to chemical effects that play a more significant role. For intergranular decohesion different contributions to the work of separation and the electronic charge density are being considered. We find further evidence that mechanical size effects are dominant for Bi and Pb. The ratio of the energy barrier for GBS and the work of separation, called the ductility parameter, D, can be determined. For Bi and Pb this measure of ductility decreases, due to a combination of inhibiting GBS and enhancing decohesion. Ag does not significantly decrease the work of separation, but due to the reduced propensity for GBS, the ductility parameter decreases significantly with Ag inclusion, to a similar value as that of Bi and Pb. This highlights the very different mechanical behavior Ag is expected to display for nanocrystalline Cu.

5.2 Introduction

It is well known that the mechanical properties of metals can change dramatically as they are exposed to chemical impurities [14, 15]. Extensive experimental and computational work has addressed this in the past and it was possible to identify many important effects resulting from impurity inclusion into metals. In this work we

will focus on two important parts of mechanical behavior of metals, grain boundary sliding (GBS) and intergranular decohesion. These are two important mechanical processes in their own right but can also be considered as competing mechanisms for systems such as nanocrystalline metals; this was discussed in detail in chapter 3 and ref. [112] for the case of nickel. In this work we aim to investigate the direct effects impurities have on the mechanical behavior of copper (Cu). At the same time the underlying mechanisms for the change of the behavior will be addressed in detail. In depth knowledge of the underlying mechanisms involved is not just an interesting theoretical curiosity but improving our understanding will benefit many industrial applications.

Grain boundary sliding (GBS) is an important process determining the mechanical properties of metals. It has been known to be of importance for the plastic flow in polycrystalline materials at high temperatures ($T > 0.4T_m$) for a long time [15, 16, 17] and was suggested to play a major role in recent experiments of nanocrystalline Cu where superplasticity was found at low temperatures [129]. The importance of GBS as a deformation mechanism in nanocrystalline metals has been studied directly [19, 20, 21, 22, 23, 24]. Several molecular dynamics (MD) studies have considered specifically nanocrystalline Cu [23, 24] and were able to observe a cross-over with decreasing grain size from a regime where plasticity is dominated by dislocation mediated activity, to a regime where GBS is the dominant process. In their work Schiøtz and co-workers [23, 24, 130] proposed that GBS, as an alternative deformation mechanism, can explain

the apparent break-down of the Hall-Petch relation observed in many nanocrystalline metals [131, 132]. We study GBS in Cu with a $\Sigma 5\,(012)$ GB and address the influence three impurities, bismuth (Bi), lead (Pb) and silver (Ag) have. These are the same impurities as treated before in chapter 4. They are common impurity elements in Cu and in particular the former two are known to cause embrittlement [14]. Ag is known to segregate to the GBs in Cu but, at least in coarse-grained materials, is not known to embrittle it. This is consistent with computational results on the integranular decohesion properties when Bi, Pb and Ag are added to the Cu GB (see section 4.5).

The mechanical properties of Cu with GBs have recently been studied from first principles [107, 108, 109, 110, 133]. Most computational and experimental work to date has addressed the mechanical properties of the Cu GB in the context of coarse-grained structures and hence only intergranular decohesion was considered. To address novel materials where grain sizes can be on the nanoscale, we also consider GBS. Little is known to date of the changes in mechanical properties as impurities are added to nanocrystalline metals; hence this work partly serves as a predictive study of the effect of impurities.

In our study of GBS we find that both Bi and Pb inhibit GBS and GB migration, resulting in an increase of brittle behavior. The effect of Ag is unexpected: although not known to embrittle coarse-grained Cu it strongly inhibits GBS. We will try to elucidate the underlying mechanisms for the changes in the energy landscape for sliding the grains of the GB. This is based on a Gedanken experiment originally

proposed in ref. [108] to study GB decohesion. We are able to distinguish different mechanisms involved in the changes of the sliding energies as we add impurities and find that these carry different importance for different impurities.

To gain a complete picture of the involved processes, we revisit intergranular decohesion of the same $\Sigma5$ (012) GB. Our previous work on the Cu GB in section 4 has so far only dealt with the effects the impurities have on the intergranular decohesion, in the form of changes in the work of separation and the tensile strength. Impurities expected to embrittle the Cu GB were shown to lower the work of separation and tensile strength. This did not yet address the underlying physical reasons for these changes to occur, which will be addressed here and compared to the mechanisms involved in GBS.

We also compare the GBS results to our results for intergranular decohesion to find the ductility parameter, D, the ratio of the work of separation, W_{sep} and the sliding energy, $\gamma^{(b)}$, defined as the energy barrier for GBS. The ductility parameter is found to decreases for all impurities, implying overall less ductile behavior. This includes Ag, which shows a marked increase in the energy for sliding, $\gamma^{(b)}$. This suggests that Ag, though believed to not cause brittle behavior in coarse-grained Cu, may have a deleterious effect on plastic deformation in the form of GBS for nanocrystalline Cu. This illustrates the great differences in the mechanical behavior one may encounter at the nanoscale.

This chapter also includes a discussion of the energetically beneficial positions of

the three impurities near the GB. We find that the substitutional sites near the GB are energetically more stable than in the bulk, which is consistent with experiments on segregation to GBs [13].

The calculations in this chapter are performed using the multiscale approach. The same computational method has previously been used to study the decohesion properties of a Cu GB in chapter 4. The method is based on coupling a small region containing the GB and the impurities, treated with density functional theory (DFT), to the bulk, treated by the embedded atom method (EAM). The concurrent multiscale approach allows us to achieve quantum mechanical accuracy near the GB and the segregated defects. It can therefore account for bond breaking and forming. At the same time it is possible to keep the computational cost at a minimum such that large systems can be considered.

The chapter is organized as follows. Section 5.3 reviews our multiscale approach and we discuss our computational method. In Section 5.4 we present results for the impurity formation energy near the GB and compare this to impurity segregation. The results for GBS of the pure Cu GB and of the Cu GB with Bi, Pb, and Ag are presented in Section 5.5 and the underlying mechanisms for the observed changes are discussed for each impurity. Section 5.6 contains a comparison to the mechanisms relevant in GB decohesion. We discuss the decohesion and GBS results in the context of the ductility parameter, D, in Section 5.7 and conclude this work in Section 5.8.

5.3 Computational Method

To be able to study large system sizes and appropriately capture any long-range effects we use the multiscale method previously discussed in detail in chapter 4. Many previous computational reports on GBS have employed small supercells, both perpendicular to and in the same plane as the GB plane [112, 134, 135, 136]. This can in principle implicitly fix atoms or at least result in constrained geometries and hence may not allow for proper relaxation.

In this implementation the quantum mechanical region of the multiscale method is described using a single-ζ basis, optimized in molecular calculations (m-SZV) to become approximately equivalent to a DZVP basis [137]. Convergence requires a density cutoff of 320 Ry for Cu. We find for the lattice constant $a_0 = 3.70$ Å and for the bulk modulus $B = 114.2$ GPa. This compares well with experiments for which the lattice constant is found to be $a_{\text{exp.}} = 3.61$ Å and the bulk modulus $B_{\text{exp.}} = 137$ GPa [124].

We study the $\Sigma 5\,(012)$ symmetric tilt GB in Cu, which is the same structure as in section 4.5. The multiscale supercell consists of 3216 Cu atoms, with appropriate substitutions by impurity atoms. The structure has 201 planes parallel to the GB plane, with 16 atoms per plane; of these, 27 planes are DFT atoms. All our structures are relaxed to account for GB expansion as described previously in section 4.5. Structural relaxations are performed using either the conjugate gradient or limited-memory Broyden-Fletcher-Goldfarb-Shanno (L-BFGS) quasi-Newton method [123].

All forces are relaxed to a magnitude of less than 0.01 eV/Å.

5.4 Impurity formation energy near the grain boundary

Impurities in Cu are known to segregate to GBs under equilibrium [13]. Experiments indicate that the highest concentration of impurities occurs around the center of the GB and then falls off exponentially toward the bulk of the grains [13]. These results are mostly based on Auger Electron Spectroscopy (AES). The experimental procedure involves exposing the Cu structures with impurities, followed by segregation normally encouraged by changing the temperature conditions appropriately. The AES analysis and the concentration behavior is then based on cleaved samples that fail via intergranular fracture. This therefore assumes that no significant diffusion occurs after the grains are decohered. We are not bound by such limitations to cleaved or otherwise altered structures and can determine the impurity formation energy and segregation energy of the relaxed GB. This first of all serves the purpose of establishing the preferential segregation sites of the impurities near the GB and secondly helps in assessing our results for GBS in section 5.5. It has been shown that some GBs support GB migration accommodated by GBS. This causes the impurities to change their position with respect to the GB plane. Hence knowledge of the impurity formation energy in the vicinity of the GB is important to understand GBS in the

context of indirectly migrating impurities.

We calculate the impurity formation energy, ε_f^X, as in eq. 5.1, reproduced here for completeness:

$$\varepsilon_f^X = \frac{1}{n_i}\left[E_{tot}^X(n_i, n_h) - E_{tot}\left(n_h^0\right) - n_i\mu_i - \left(n_h - n_h^0\right)\varepsilon_h\right], \tag{5.1}$$

where $E_{tot}\left(n_h^0\right)$ is the energy of the system with no impurities and n_h^0 host atoms, $E_{tot}^X(n_i, n_h)$ is the energy of the system with n_i impurities of type X, and n_h host atoms, ε_h is the energy per atom of the metal matrix host in its ideal structure and μ_i is the chemical potential of the impurities. For typical DFT calculations ε_h would normally be based on the same parameters and similar structures as the calculations for $E_{tot}^X(n_i, n_h)$ and $E_{tot}\left(n_h^0\right)$. This is not possible here, as the latter two are based on multiscale calculations. The former needs to be approximated by a separate DFT or EAM calculation, depending on whether the removed host atom is located in region I or region II. As an approximation for removing a DFT atom from the multiscale structure we therefore base ε_h on a calculation using DFT with periodic boundary conditions of a $5 \times 5 \times 5$ supercell with a 4 atom basis. This is close to the number of atoms used in the multiscale approach (432 DFT atoms), and reasonably converged with respect to the supercell size. The energy ε_h for a calculation based on a $4 \times 4 \times 4$ supercell and otherwise the same parameters is different by only 0.01 eV (see Fig. 5.1). The chemical potential, μ_i, of the impurities is determined by considering the energy of a single impurity surrounded by a large amount of vacuum. The calculations are based on the same parameters as the calculation used to determine ε_h.

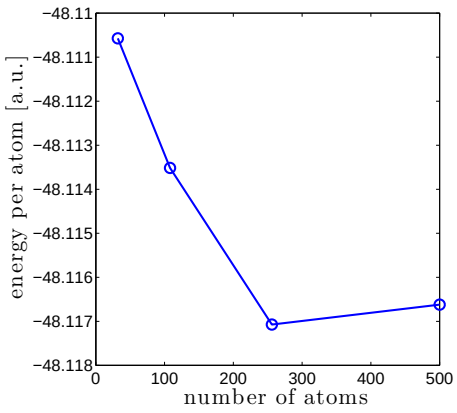

Figure 5.1: Energy per atom for Cu, ε_h, for different supercell sizes.

The structures for the calculations of the segregation energy are based on a Cu GB with all atomic positions relaxed. Care was taken to relax all bulk strain as described in section 4.5. We place substitutional impurities at different lattice sites. Our supercell has 16 atoms per plane, and we place only one impurity atom into the supercell. All atomic positions are fully relaxed after impurities are added. No explicit strain relaxations were performed, that is changes in the supercell size were neglected, since this was found to be negligible when substituting only one atom in a plane of 16. The results are shown as individual data points in Fig. 5.2 (a), (b) and (c) for Bi, Pb and Ag, respectively. Energies were shifted by the bulk impurity formation energy to show the GB segregation energy with respect to a bulk solute atom. The bulk impurity formation energy is based on a calculation of a $5 \times 5 \times 5$ supercell with a 4 atom basis. This DFT calculation was performed with fully periodic boundary conditions. We immediately see that the energies near the GB are lower than the

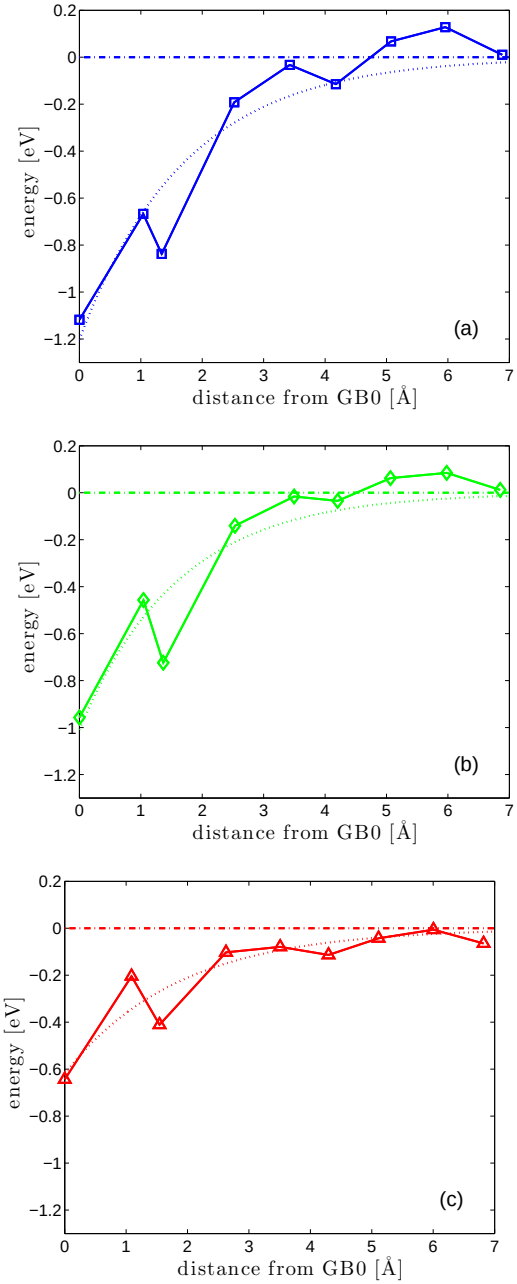

Figure 5.2: Segregation energy as a function of distance to the center GB plane at GB0 for (a) Bi, (b) Pb and (c) Ag. For each case, one impurity is placed on a substitutional site on a plane with otherwise 16 Cu atoms. An exponential fit to illustrate the exponential behavior of the impurity concentration near a GB is shown as a dotted line. Solid lines connecting individual data points are guides for the eye only.

bulk value for all three impurities. The lowest energy position for all three impurities is on the GB0 layer, with impurities at the GB1 layer being greater in value than those at the GB2 layer. The energy recovers to the bulk value at around four to eight layers away from the center plane of the GB. The variation of the segregation energy for layers four to eight is not surprising, as the GB sets up a perturbation that can still be felt at that distance. We also show an exponential fit as a dotted line to illustrate the expected exponential behavior of the impurity concentration. The greatest segregation energy was found for Bi, closely followed by Pb. The segregation energy of Ag is almost half that of Bi.

5.5 Grain boundary sliding

We begin our treatment of the mechanical properties of Cu by considering GBS to assess how the ductility changes as we add impurities. This was previously discussed in the context of plastic deformation mechanisms for nanocrystalline metals in chapter 3. Based on our fully relaxed GB structures we slide the two half crystals against each other along $\langle 012 \rangle$, which is a vector of the coincidence site lattice (CSL) . All calculations are based on simulating sliding quasistatically, that is the two grains are shifted rigidly against each other. After sliding, all slip plane atoms are held fixed in the in-plane directions but allowed to relax freely perpendicular to the GB plane. This is to ensure that the slip plane vectors can be appropriately defined. All other atoms are allowed to fully relax. The results are shown in Fig. 5.3 for the pure GB

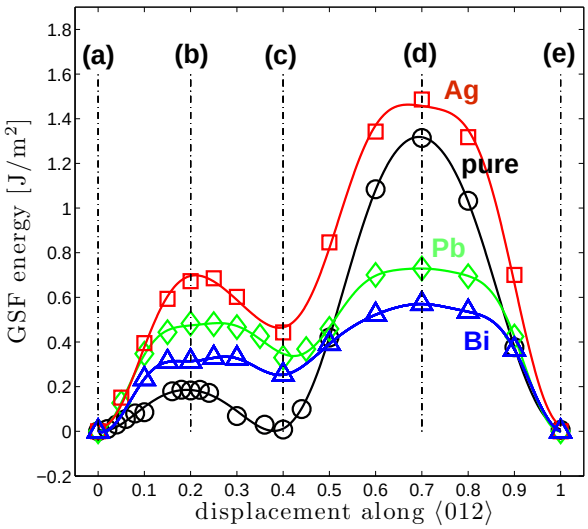

Figure 5.3: Sliding energy along the slip vector ⟨012⟩ for the Σ5 (012) GB without impurities (black circles) and with Bi (blue triangles), Pb (green diamonds) and Ag (red squares) impurities. The impurities were placed as substitutional defects as one ML on the GB0 plane. Solid lines are Fourier series fits. We indicate important points along the slip displacement by dash-dotted vertical lines labeled (a) through (e). The corresponding atomic structures are shown in Fig.'s 5.4, 5.5, 5.6 and 5.7 with corresponding label convention of the important positions for the clean GB and with Bi, Pb, and Ag impurities, respectively.

and the GB with a monolayer (ML) of substitutional impurities (Bi, Pb, and Ag). The lowest energy positions at the GB0 sites are chosen for the initial positions of all impurities before the grains are displaced.

5.5.1 Pure system

We first discuss GBS for the pure Σ5 (012) GB, plotted as black circles with a solid black line fit in Fig. 5.3. Several distinct points of extrema can be seen, occurring at slip displacements of approximately $s = 0.0$, 0.2, 0.4, 0.7 and 1.0 times

the periodic displacement along ⟨012⟩. These are labeled as (a),(b),(c),(d) and (e) in Fig. 5.3, respectively. The atomic positions of these slip displacements are shown in Fig. 5.4 (a)-(d), with important energies labeled $\gamma^{(a)-(d)}$ listed in Table 5.1. We indicate atoms in the adjacent parallel {001} planes with filled and unfilled circles in Fig. 5.4. The first of these structures, labeled (a), is the lowest energy GB with no slip displacements. The GB plane is indicated as a dashed black line, and remains centered on the same atoms in the series of images to clearly show the initial position of the GB plane as sliding proceeds. We have included the characteristic diamond shapes across the GB plane, showing the GB in the traditional way. Point (e) in Fig. 5.3 is just a periodic displacement of the structure of point (a) and equivalent in its atomic positions. It is therefore not reproduced in the series of structural schematics in Fig. 5.4. As the grains are slid by a factor of $s = 0.2$ of the full sliding distance to position (b), we observe a local maximum in Fig. 5.3. This maximum is a result of a run-on configuration as illustrated in Fig. 5.4 (b). This puts slip plane atoms of adjacent {001} planes at the same coordinate along ⟨012⟩, and therefore results in an increased energy. The maximum at $s = 0.7$ times the slip displacement along ⟨012⟩ is also caused by a run-on configuration across the slip plane. In this case, as shown in Fig. 5.4 (d), slip plane atoms in the same (001) planes share the same in-plane coordinates. This causes the global maximum of this curve and a significant expansion around the GB plane as seen in Fig. 5.4 (d). This maximum provides with an energetically unfavorable pathway. Due to symmetry the GB can slide under the

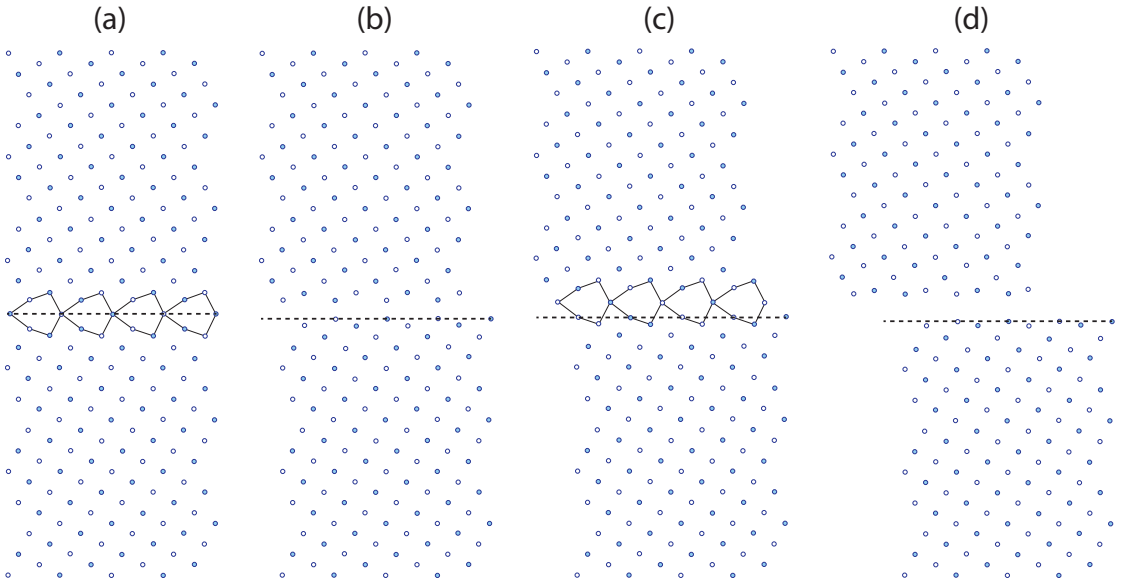

Figure 5.4: Atomic positions for the slip displacements as indicated in Fig. 5.3 for the clean Cu $\Sigma 5\,(012)$ GB, where (a) is for $s = 0.0$ the original relaxed GB with no slip displacement, (b) for $s = 0.2$, (c) for $s = 0.4$ and (d) for $s = 0.7$ times along the periodic slip displacement along $\langle 012 \rangle$. Light blue empty circles represent Cu atoms on the (001) plane with light blue filled circles representing Cu atoms on the adjacent (002) plane. The original GB plane as for position (a) is indicated by a dashed black line. For slip displacements the characteristic diamond shapes across the GB indicate the GB plane where possible.

same applied shear stress using the lower energy path symmetrically on the opposite side of the GB plane. That is, for a given applied shear stress the GB can always slide such that the path leads it across the lower energy run-on configuration of Fig. 5.4(b).

Fig. 5.3 also shows a minimum at $s = 0.4$. This is a geometrically equivalent structure as the initial GB. However, as shown in Fig. 5.4 (c) the GB plane migrates one layer as a sliding event from (a) to (c) or (e) to (c) takes place. This is indicated by the dashed line which lies on the atoms of the original GB0 layer, and the diamond shapes that now indicate that the GB plane migrated up by one layer. On shearing the

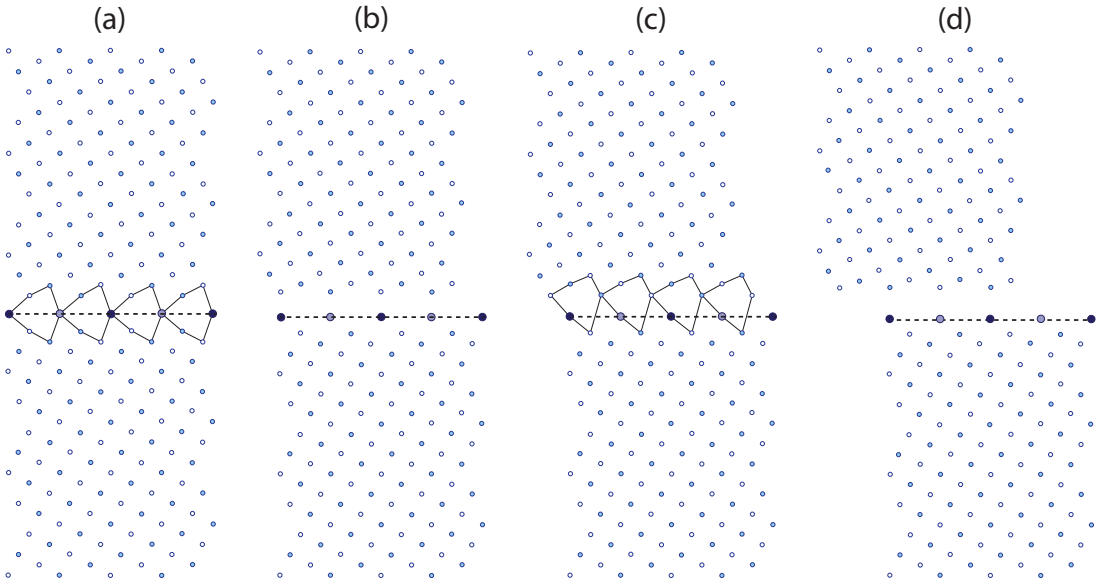

Figure 5.5: Same as in Fig. 5.4, but for the Cu $\Sigma5\,(012)$ GB with Bi impurities. Bi impurities are represented by large circles in dark blue. Empty dark blue circles represent Bi atoms on the (001) plane and filled dark blue circles represent Bi atoms on the adjacent (002) plane.

$\Sigma5\,(012)$ Cu GB, one may therefore envisage how the GB may migrate, accommodated by repeated GBS between GB0 and GB1 (or GB-1) planes.

5.5.2 Impurity system

We now consider GBS as we add 1 ML of impurities to the GB0 plane. We first discuss Bi and Pb shown as blue triangles and green diamonds in Fig. 5.3, respectively. Both show a similar change in behavior. This is consistent with the similarity of the two impurities already seen in Section 4.5 when we considered the work of separation and tensile strength. We saw that both Bi and Pb impurities embrittle the GB by enabling easier intergranular failure. We now study if they have

a similarly detrimental effect on plasticity in the form of GBS for nanocrystalline metals. The maximum for $s = 0.20$ increases by a factor of 1.7 and 2.6 for Bi and Pb, respectively, meaning that this lowest local maximum that connected two geometrically equivalent structures for the pure system becomes energetically less beneficial as a pathway. This in turn means that GBS along this direction is inhibited by the inclusion of Bi and Pb impurities. It is important to note that whereas position (c) was geometrically equivalent to position (a) for the clean GB, this is not the case for the impurity systems. Instead, since the GB plane migrates by one (012) plane, the impurities are now on the GB1 plane instead of at the GB0 plane as for position (a). This can be seen for Bi and Pb in Fig. 5.5 (c) and Fig. 5.6 (c), respectively. This explains why the sliding energy curve has a local minimum at position (c) that is greater than the minimum at zero slip displacement at position (a). As we discussed earlier in Section 5.4 the GB0 planes provide lower energy positions in comparison to GB1 sites, with the GB0 sites providing the lowest energy sites in comparison to all others.

The second maximum, for direct run-on configurations at point (d), sees a marked decrease in comparison to a clean GB. This decrease still provides a larger barrier than for position (b) and hence should not be a preferential pathway of slip behavior, since with the same shear stress applied, a slip over the smaller maximum is supported by planes symmetrically on the other side of the GB plane. It is important to note that we find that the distortions to the GB for impurities at GB1 at (c) are quite large,

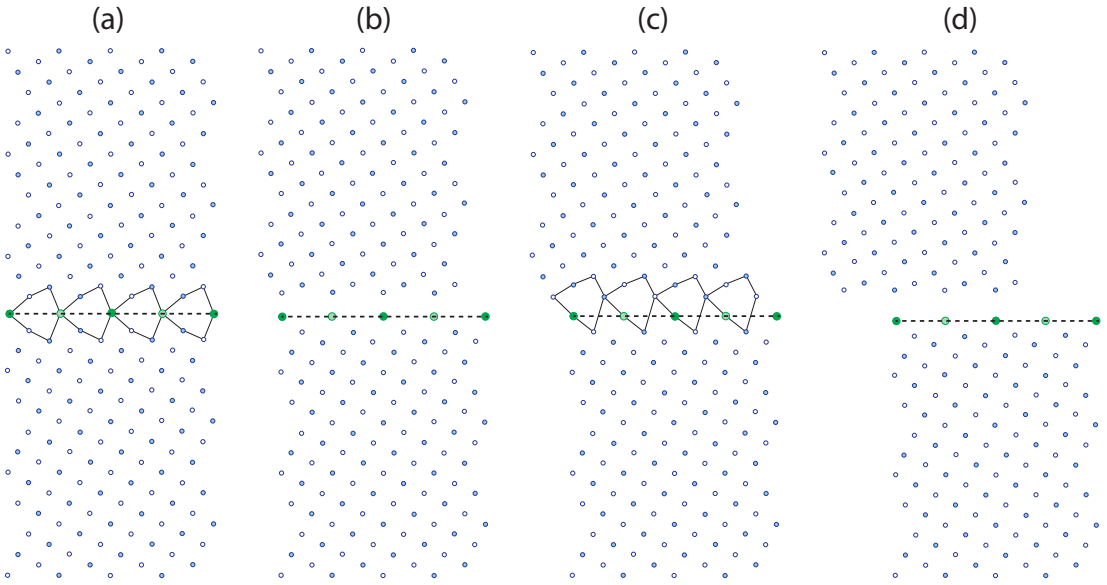

Figure 5.6: Same as in Fig. 5.4, but for the Cu $\Sigma 5\,(012)$ GB with Pb impurities. Pb impurities are represented by large circles in green. Empty dark green circles represent Pb atoms on the (001) plane and filled green circles represent Pb atoms on the adjacent (002) plane.

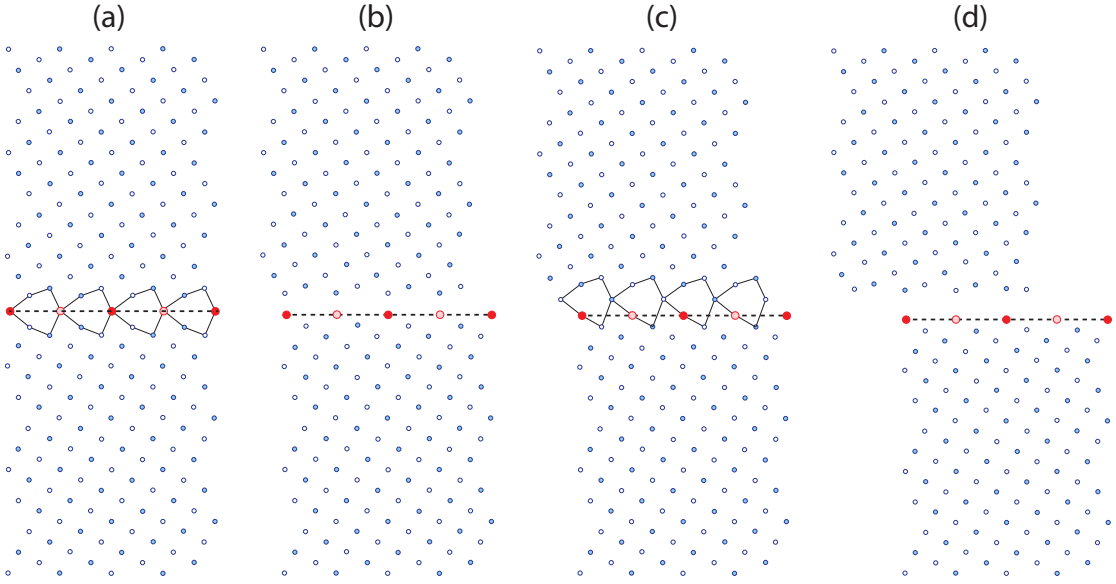

Figure 5.7: Same as in Fig. 5.4, but for the Cu $\Sigma 5\,(012)$ GB with Ag impurities. Ag impurities are represented by large circles in red. Empty red circles represent Ag atoms on the (001) plane and filled red circles represent Ag atoms on the adjacent (002) plane.

and the usual diamond shape to identify the GB plane is distorted. This difference and how it relates to the significant changes in the sliding energies will be discussed in greater detail in Section 5.5.3.

We see that for both Bi and Pb the energy barrier to go from (c) to (a) via (b) decreases dramatically because the impurities at (c) are at the higher energy GB1 position. The relevant energies are shown in Table 5.1. This shows that a higher concentration of impurities at GB1 sites could very easily migrate to GB0 via sliding induced GB migration. This is particularly so because the barrier decreases to a value significantly lower than for the clean GB. The impurities that migrated from GB1 to GB0 would then be effectively trapped at GB0 because both the formation energy is significantly lower at the center of the GB for Bi and Pb, making diffusion away from the GB unlikely (see Fig. 5.2) and further sliding is inhibited by the overall increase in the energy barrier at position (b) with respect to (a). For the particular $\Sigma5\,(012)$ symmetric tilt GB, one may imagine a scenario where an initially clean GB could pick up impurities in the bulk by successive GBS and GB migration events. This may then pin the GB plane, leading to potential embrittlement due to a decrease in plasticity. This does not address the potentially different time-scales of GBS and diffusion of impurity atoms to the GB.

We now move our attention to the effects Ag has on GBS. For our results of the work of separation we have previously seen that Ag had only a small effect on the embrittlement of the Cu GB. That is, the work of separation and the tensile

system	$\gamma^{(b)}$ [J/m^2]	$\gamma^{(b)} - \gamma^{(c)}$ [J/m^2]
pure	0.186	0.175
Ag	0.699	0.229
Pb	0.485	0.153
Bi	0.314	0.061

Table 5.1: Sliding energy differences of important paths. The first column shows the energy difference of going from (a) to (b), previously defined as $\gamma^{(b)}$ for GBS. The second column shows the energy difference between positions (c) and (b). This quantifies the propensity of the system to slide from (c) to (a) via (b).

strength decreased by only a very small amount in comparison to Bi and Pb. This is expected, as Ag is not known to embrittle coarse-grained Cu. We are not aware of any experimental work on the behavior of Ag in nanocrystalline metals. It should therefore not be expected that Ag necessarily does not affect the GBS behavior, since the experimental knowledge that Ag does not embrittle or otherwise significantly affect Cu GBs is purely based on coarse-grained materials under normal conditions, where GBS should not be of importance. This study should therefore be viewed as making predictive statements as to the behavior of Ag, rather than confirm experimentally established knowledge.

The sliding energy curve for one ML Ag is shown as red squares in Fig. 5.3. We see that the changes to the sliding behavior are even more significant than for Bi and Pb. The energy at position (b), $\gamma^{(b)}$, increases by a factor of almost 4 in comparison to the clean GB. This means that GBS becomes energetically very unfavorable. In turn this also inhibits GB migration for the $\Sigma5\,(012)$ GB. The energies of positions (c) and (d) also increase in comparison to the clean GB. Again, as for the Bi and Pb system, the

increase in the energy for position (c) is due to the impurities migrating with the GB to layer GB1, which is energetically higher (Fig. 5.2 (c)). It is interesting to note that the structural changes in comparison to the clean GB are not as significant as for Bi or Pb. This can be seen by comparing Fig. 5.4 and Fig. 5.7. Especially the structure at position (c), where the impurities are at GB1 sites are significantly less distorted than for Pb and Bi in Fig. 5.6 (c) and Fig. 5.5 (c). Hence the underlying physics of the increase of the GSF sliding energy for Ag and the Bi and Pb systems should be expected to be different. This difference will be addressed further in Section 5.5.3, where we try to elucidate the mechanisms that result in the different behavior seen for the clean GB and the impurity systems.

5.5.3 Grain boundary sliding mechanism - Gedanken experiment

We have seen in the previous section that the effect of impurities on GBS and the sliding energies can be dramatic. We did not address yet the underlying physical mechanisms involved and how these are different for the different impurities and the clean GB. To this end we adapt a method recently proposed by Lozovoi *et al.* [108] to address intergranular decohesion. The aim is to disentangle the different mechanisms involved by splitting the sliding event into different steps in a Gedanken experiment. We will consider three different mechanisms involved in GBS with impurities, 1) that of breaking of bonds of host matrix atoms by replacing them with substitutional impu-

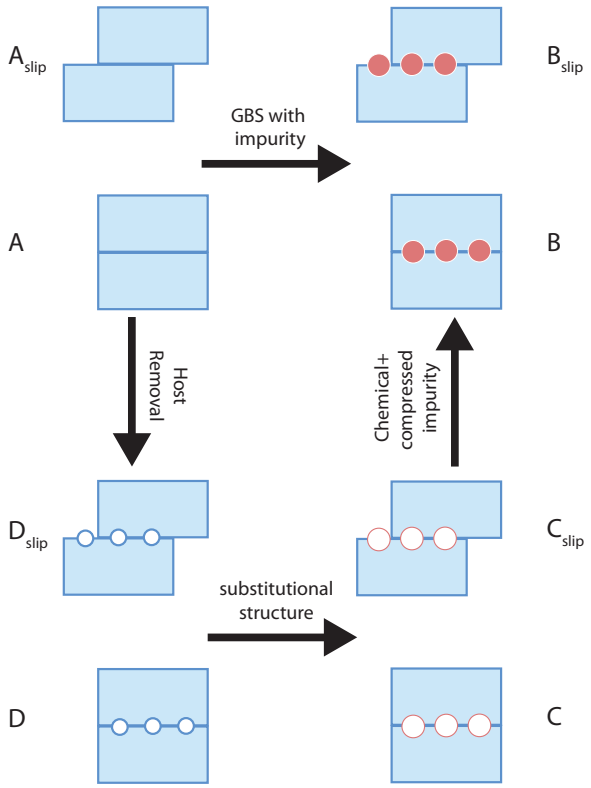

Figure 5.8: Schematic illustrating the calculations to elucidate the different mechanisms involved in inhibiting GBS for impurity inclusion. Configuration A is for no impurities and allows relaxations. Similarly configuration B has impurities at the GB and also allows for relaxations. Configuration C is based on the structures of configuration B, but all impurity atoms are removed, no further relaxations are allowed. Similarly configuration D is based on configuration A, but all Cu atoms that would be replaced by impurities in configuration B are removed, with no further relaxations.

rity atoms, 2) that of a change in the atomic structure surrounding the substitutional impurities and 3) that of chemical effects in combination with the impurity being mechanically compressed. The latter combined effect cannot be further disentangled in this approach. We will follow here the same labeling convention as in ref. [108] and will forthwith call these three processes the host removal (HR), substitutional structure (SS) and chemical and compressed impurity (CC) process, respectively.

A schematic illustration of the different mechanisms and how their contribution to the overall GBS effect can be calculated is shown in Fig. 5.8. Four different separate GBS energies will be calculated, labeled as A, B, C and D. The calculations for A and B are simply the GBS energies for the clean GB and those with impurities. These calculations allow for atomic relaxations as per section 5.5. The difference between A and B hence just gives the increase or decrease of the sliding energy as we add impurities. To investigate the HR process and its contribution to the overall change of the GBS energy, we calculate structures D. These are based on the relaxed structures of the clean GB, that is structure A, but with the Cu atoms that are replaced by substitutional impurities in B removed. The energy difference between A and D hence gives a measure of how much the loss of host bonds contributes to the overall energy change. Similarly, to address how much the substitutional impurities change the structure of the surrounding host matrix, we calculate the difference between D and C. Structure C is based on the relaxed structures of B, but now with the impurities removed. This hence gives a measure of how much the Cu matrix is distorted upon impurity addition, but without including the chemical effects of the impurities added by bonding in a different fashion than the Cu atoms. The two processes we have discussed so far, the HR and SS process, are purely mechanical processes that account for the size effect of substitional impurity atoms. To capture the chemistry of the impurities we compare structures C and B. This includes all the bonds introduced by the impurities, but also any mechanical compression the

impurities may suffer from. We calculate the following quantities based on the above ideas. For the host removal process,

$$\mathrm{HR} = \gamma\left(\mathrm{D}\right) - \gamma\left(\mathrm{A}\right), \tag{5.2}$$

the substitutional structure process,

$$\mathrm{SS} = \gamma\left(\mathrm{C}\right) - \gamma\left(\mathrm{D}\right), \tag{5.3}$$

and for the chemical and compressed impurity process,

$$\mathrm{CC} = \gamma\left(\mathrm{B}\right) - \gamma\left(\mathrm{C}\right), \tag{5.4}$$

where $\gamma\left(x\right)$ is the sliding energy at a given slip displacement position for a given system $x = \mathrm{A} - \mathrm{D}$.

We start our discussion of the mechanisms involved in changing the GBS behavior as impurities are added by considering the effect Bi has. We will consider the three different mechanisms for the three important sliding displacements of $s = 0.2, 0.4$ and 0.7 along $\langle 012 \rangle$, that is positions (b), (c) and (d). This is summarized in Tables 5.2, 5.3 and 5.3, respectively. For configuration (b), which gives the energy barrier for sliding and hence is the most important energy to quantify resistance against slip, we see an overall increase when Bi impurities are added. The dominant terms in this increase are the SS and HR mechanisms. The chemical contributions in the form of the CC mechanism is very small and negligible in comparison. This implies that most of the change in $\gamma^{(b)}$ comes from mechanical effects related to the size of the Bi impurity.

The chemical term is of little importance. This behavior is matched for position (c), where the SS term increases relative to the HR term, resulting in an overall increase in the slip energy. The situation changes slightly for the most extreme run-on configuration, that of position (d). Here we see that the substitutional effect is significantly smaller than the host removal effect, leading to an overall significant decrease in the slip energy. This decrease in the importance of the substitutional structure change may be related to the fact that the Cu matrix is only affected by a small amount by the impurities in this special configuration, where the two grains are pushed apart for both impurities and the clean GB, since atoms on the slip plane are positioned right on top of one another. It is important to point out that the chemical and compressed impurity effect for Bi is very small for all configurations.

For Pb the behavior is very similar as for Bi. For configuration (b) the substitutional structure change is very similar to that of Bi. Again for both configuration (b) and (c) the dominant terms are the SS and HR mechanism. The main difference for Pb in comparison to Bi is that the chemical and compressed impurity term becomes more important. This results in an overall increase in the slip energy for both configuration (b) and (c) and a smaller decrease in the slip energy for configuration (d).

We have already discussed in section 5.5.2 that of the three impurities, Ag increases the sliding energy for all positions by the greatest amount. This at first seems counterintuitive with respect to our earlier results for intergranular decohesion, where

system	Total [J/m^2]	SS [J/m^2]	HR [J/m^2]	CC [J/m^2]
Ag	0.489	0.614	-0.539	0.414
Pb	0.300	0.715	-0.539	0.124
Bi	0.131	0.707	-0.539	-0.037

Table 5.2: GBS mechanisms - slip position (b). Total stands for the total change with respect to the clean Cu system, SS stands for substitutional structure process, HR stands for the host removal process and CC stands for the chemical and compressed impurity process.

system	Total [J/m^2]	SS [J/m^2]	HR [J/m^2]	CC [J/m^2]
Ag	0.435	0.446	-0.405	0.394
Pb	0.322	0.607	-0.405	0.120
Bi	0.245	0.619	-0.405	0.031

Table 5.3: GBS mechanisms - slip position (c). Label convention as in Table 5.2.

system	Total [J/m^2]	SS [J/m^2]	HR [J/m^2]	CC [J/m^2]
Ag	0.172	0.470	-0.925	0.627
Pb	-0.585	0.199	-0.925	0.141
Bi	-0.743	0.149	-0.925	0.032

Table 5.4: GBS mechanisms - slip position (d). Label convention as in Table 5.2.

Ag does not act strongly as an embrittling impurity and influences the structure only by a small amount. We may therefore expect that it should also not increase the GBS energy, and not affect any plastic deformation accommodated by GBS. It is even more surprising that the changes are even greater than for Bi or Pb. By considering the different mechanisms of Tables 5.2, 5.3 and 5.4 the origin of this difference to Bi and Pb becomes more apparent. For Bi and Pb the SS and HR terms were dominant and the CC term was small in comparison for all configurations. In contrast, Ag has a much larger chemical and compressed impurity contribution. This is positive, and binds more strongly than Bi or Pb, and almost as strongly as a Cu atom, at least for configuration (b) and (c). All terms are similar order of magnitude for Ag, implying that chemical effects become more important in comparison to the purely mechanical effects of Bi and Pb. As expected from Fig. 5.5, 5.6 and 5.7, the substitutional structure contribution for Ag impurities is lower than that for Bi and Pb.

5.6 Intergranular decohesion mechanism

5.6.1 Work of separation - revisited

We have previously considered the work of separation as a measure for intergranular embrittlement in Section 4.5. We found a significant decrease of the work of separation when Bi and Pb impurities are included into the Cu GB structure. Instead Ag was found to only cause a minor decrease, not consistent with embrittlement.

In this section we wish to further understand the underlying mechanism involved in embrittlement by impurities of the $\Sigma5\,(012)$ Cu GB used in this work. We will employ the Gedanken experiment introduced in section 5.5.3 and extend it by explicitly considering the electronic charge densities of relevant structures.

Intergranular decohesion is of great importance in understanding the chemical embrittlement of metals. There are generally two schools of thought of the underlying physical reasons as for the cause of embrittlement by impurity inclusion at GBs. The first is that of electronic effects and was first proposed by Losch *et al.* [138] followed by several studies [139, 140, 110, 141] with similar conclusions alluding to electronic effects. Several theories exist that address the problem using explanations based on electronic effects. The first proposed that impurities may deplete the surrounding metal matrix of electronic charge and thereby weaken the interface [138, 141]. The second theory considers the changes in the bonding between the metal and impurity atoms and it is proposed that the impurities result in stiffer bonds that are more likely to break [139, 140]. Recently, Duscher *et al.* [110] proposed an altogether different idea, where the dominant process is that charge is donated by the impurities resulting in a weakened interface, though questions have been raised as to the validity of their arguments [107, 108].

An alternative explanation of the effect impurities have on the cohesion of the GBs can be generally classified as a size effect issue. This was proposed in several studies [107, 108, 109, 142, 143, 144, 145] and has recently been subject to a detailed

study by Lozovoi *et al.* [108] for the Cu system. They develop a Gedanken experiment that allows for a single path to identify the underlying mechanism for different impurity systems. We extend the method by explicitly considering the electron charge densities to make a direct connection with the ideas of the theories based on electronic effects. By studying the $\Sigma5\,(012)$ Cu GB, we come to similar conclusions as in ref. [108], but it will be highlighted that the GB character can have a significant influence on the exact results.

The work of separation results of Section 4.5 were determined by comparing the energy of a fully relaxed GB with a separated structure of two grains where the impurities were placed such that one ML was kept on one grain and the other grain was a clean Cu surface. It is known experimentally that after cleavage fracture, approximately equal levels of impurity concentration are measured on each fractured surface [13]. However, this is based on AES experiments which means that it inherently represents an average over several ML's. To investigate this further we perform calculations where the final impurity concentration is half on each grain, as depicted in Fig. 5.9. There are many other possible configurations but we choose this configuration to maximize the distance between impurity atoms. One could also envisage clusters forming, but this will not be addressed in this work. The results for the clean GB and the GB with one ML of Ag, Bi and Pb impurities are summarized in Table 5.5. The difference in values in comparison to chapter 4, can be traced back to the different parameters and structures used. The most important quantity, the

change of the work of separation for impurity inclusion, is very similar and if the size change of region I is accounted for, we find that the results for the change in W_{sep} differ by only $1-2\%$ for Bi and Ag and 6% for Pb. Employing the computationally more efficient implementation is appropriate for the analysis presented in this work and well within the accuracy limits required.

We see for both the clean GB and the GB with Ag, that the work of separation is lower for the case where the ML stays intact on a given separated grain. This is expected for pure Cu, as the energy for cleaving along a perfect weak plane (here the GB plane) is lowest in comparison to situations where a plane of atoms is unevenly separated. The half concentration configuration leaves atoms on the top of a surface that are not optimally bonded and hence has a higher energy. The Ag impurity atoms seem to behave very similar to Cu in this sense. This may be expected, since Ag behaves similar in terms of binding as chemically they are from the same group and were already found to behave very similar in terms of the chemical contribution for GBS (section 5.5.3) and intergranular decohesion (section 4).

For Bi and Pb we find that structures with half concentrations on the surfaces after decohesion are energetically more beneficial. This is similar to previous results of Bi with a different Cu GB [108]. The difference is particularly significant for Bi. We will therefore use these energetically more beneficial structures for Bi and Pb in the following analysis and discussion.

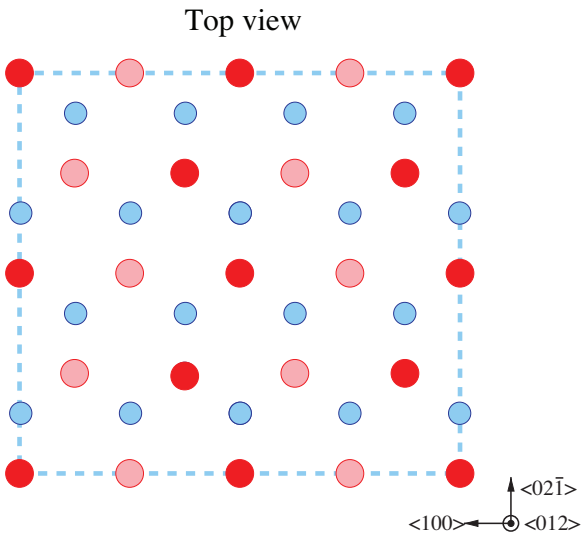

Figure 5.9: Impurity configuration for half occupancy of surfaces after decohesion. Light blue atoms are Cu atoms on the GB-1 plane. Red circles represent impurity atoms on the GB0 plane, where light and dark red circles represent atoms that stay on the bottom grain with GB-1 and atoms that get cleaved and attach to GB1 with the top grain, respectively.

system	W_{sep} [J/m^2]	$W_{sep}^{(1/2)}$ [J/m^2]	$W_{sep} - W_{sep}^{(1/2)}$ [J/m^2]
pure	2.10	2.15	-0.05
Ag	1.92	1.99	-0.07
Pb	1.42	1.30	+0.12
Bi	1.15	0.921	+0.23

Table 5.5: Work of separation for half ($W_{sep}^{(1/2)}$) and full (W_{sep}) occupancy on surface after decohesion of the GB0 plane.

system	Total [J/m^2]	SS [J/m^2]	HR [J/m^2]	CC [J/m^2]
Ag	-0.174	-0.061	-1.171	1.058
Pb	-0.854	-0.222	-1.170	0.590
Bi	-1.230	-0.372	-1.170	0.365

Table 5.6: Work of separation mechanisms. Total stands for the total change with respect to the clean Cu system, SS stands for substitutional structure process, HR stands for the host removal process and CC stands for the chemical and compressed impurity process.

5.6.2 Underlying mechanisms

We have seen that the work of separation for Bi and Pb decreases considerably, especially for half coverage after decohesion, whereas Ag has only a small effect on W_{sep}. We wish to study this difference in behavior with the same method as presented in section 5.5.3. This method was previously used to study a $\Sigma5\,(013)$ Cu GB with Bi, Na and Ag impurities [108] and we will compare these findings to our results for the $\Sigma5\,(012)$ Cu GB with impurities. The results for the $\Sigma5\,(013)$ Cu GB showed significant substitutional structure effects and these were identified as the driving force to decrease the work of separation for increasing impurity concentration. It was also concluded that any electronic effects are not important, based on comparing the energies for the three different impurities studied. No explicit study of the electronic charge density was performed.

The summary of the different contributions of the relevant mechanisms involved in decohesion of the $\Sigma5\,(012)$ GB are shown in Table 5.6. We see that for Bi the dominant term is the HR term, with the SS and CC term approximately canceling one another

and the magnitude is approximately one third of that of the HR term. Although these results are for one ML coverage as in ref. [108] we do not see the strong substitutional structure effect they were able to observe. This is because the $\Sigma5\,(012)$ GB has perfectly symmetric substitutional positions at the GB0 plane, whereas the $\Sigma5\,(013)$ has two geometrically different positions, of which one has tighter confinement than the other. This results in the greater substitutional structure effect as their GB is deformed much more significantly than the GB studied here. This illustrates that even the small differences within the same type of GB, both are high-angle $\Sigma5$ GBs, can be significant. The smaller substitutional changes result in a smaller propensity to cause embrittlement. For the same Bi impurity concentration, that is 1 ML coverage, the work of separation of the $\Sigma5\,(012)$ was reduced by 56%, whereas the $\Sigma5\,(013)$ GB suffers from a 71% decrease of the work of separation and 36% for half the concentration of 0.5 ML coverage [108].

Given the controversy of whether impurities that embrittle Cu result in charge transfer to deplete the charge of Cu atoms surrounding the impurities, it is instructional to explicitly study the electronic charge density in addition to the above analysis. We show in Fig. 5.10(a) the electronic charge density for the pure Cu GB. This should be compared to Fig. 5.10(c) for substitutional Bi atoms at the center GB plane. Both electronic charge density plots show the (001) plane which perpendicularly intersects the GB plane. These figures show in particular the bonds of the Bi or GB0 Cu atoms with the GB1 and GB-1 atoms, but also the Cu-Cu bonds of

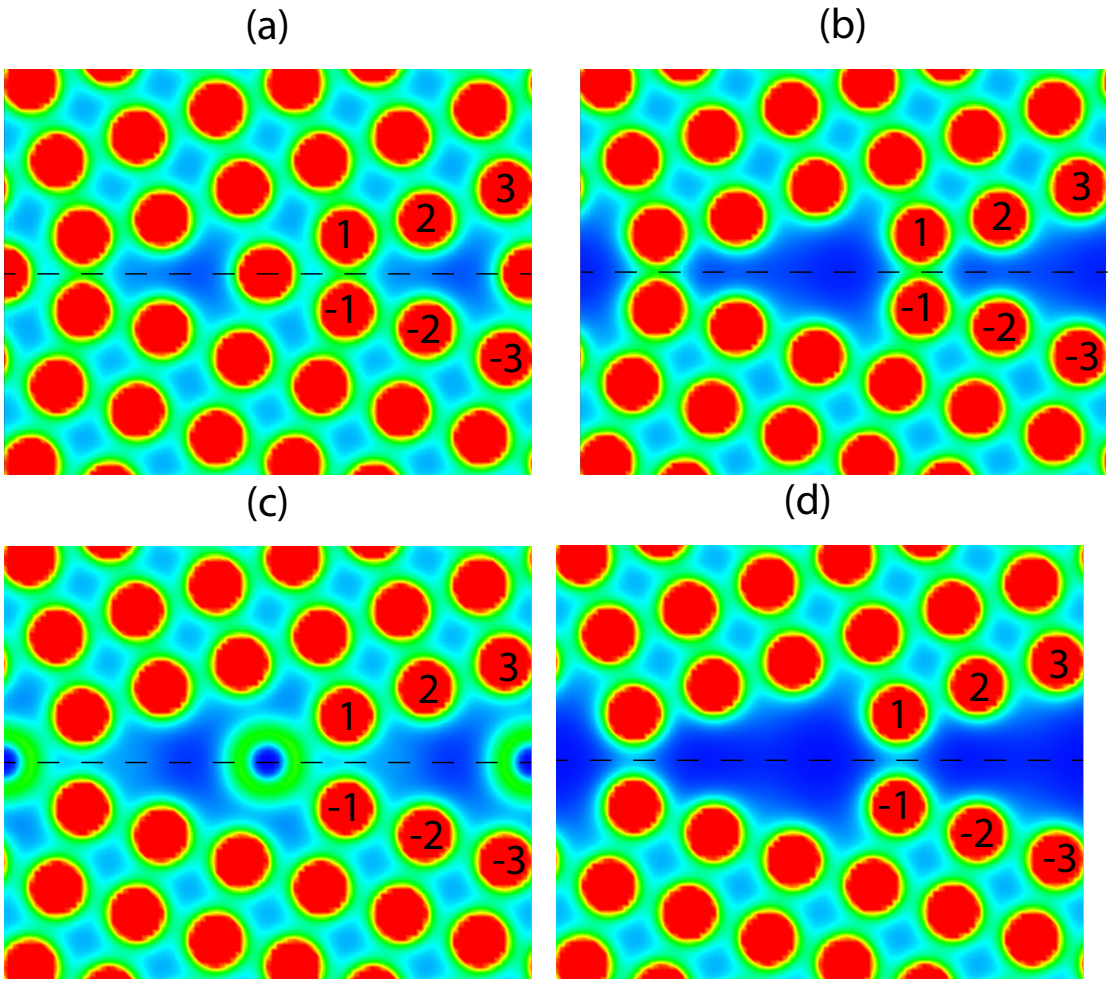

Figure 5.10: Electronic charge density on the (001) plane intersecting the GB for (a) the $\Sigma 5\,(012)$ Cu GB, (b) the GB without Cu atoms on the GB0 plane, same as structure D in Fig. 5.8, (c) the Cu GB with Bi impurities at the center GB0 plane, (d) the Cu GB structure as for Bi impurities, but with all Bi removed same as structure C in Fig. 5.8. The center GB plane (GB0) is indicated by a dashed black line. Atoms in the first three sets of symmetric planes away from the center GB plane are label $-3, \ldots, 3$. Red areas are regions of large electronic charge density, blue areas are regions of small electronic charge density.

the GB1 and GB-1 Cu atoms across the interface. Of these two different bonds, the former does not change significantly, whereas the latter shows a significant depletion of electronic charge on Bi inclusion. At first glance this may lead to the conclusion, that based on the difference in chemical character of the included Bi atoms, charge redistribution has occurred in the context of electronic effect theories, thereby weakening the Cu-Cu bond between atoms GB1 and GB-1 across the interface. On closer inspection this change in electronic charge distribution is a result of the substitutional structure changes. This can be seen by comparing Fig. 5.10(b) and (d). These show the electronic charge density for structures where the Cu atoms at the GB0 plane and the Bi impurity atoms have been removed but with no further relaxations as for structures D and C in Fig. 5.8, respectively. The electronic charge density between Cu atoms in the GB1 and GB-1 planes, that take crucial roles in bonding across the GB interface and hence its cohesion, remain approximately unchanged in comparison to the structures with all atoms on the GB0 planes. This means that adding or removing Bi atoms does not significantly affect the electronic charge density of the Cu-Cu bond across the GB interface. It is instead purely the GB expansion caused by adding the large Bi atoms, that is, the dominant changes in the electronic charge density are a mechanical effect and not due to the chemical character of the Bi impurities. If anything, one can see that the electronic charge density between the Cu atoms increases as Bi atoms are added, albeit this is not a strong effect.

The behavior of Pb is very similar to that of Bi except that the chemical con-

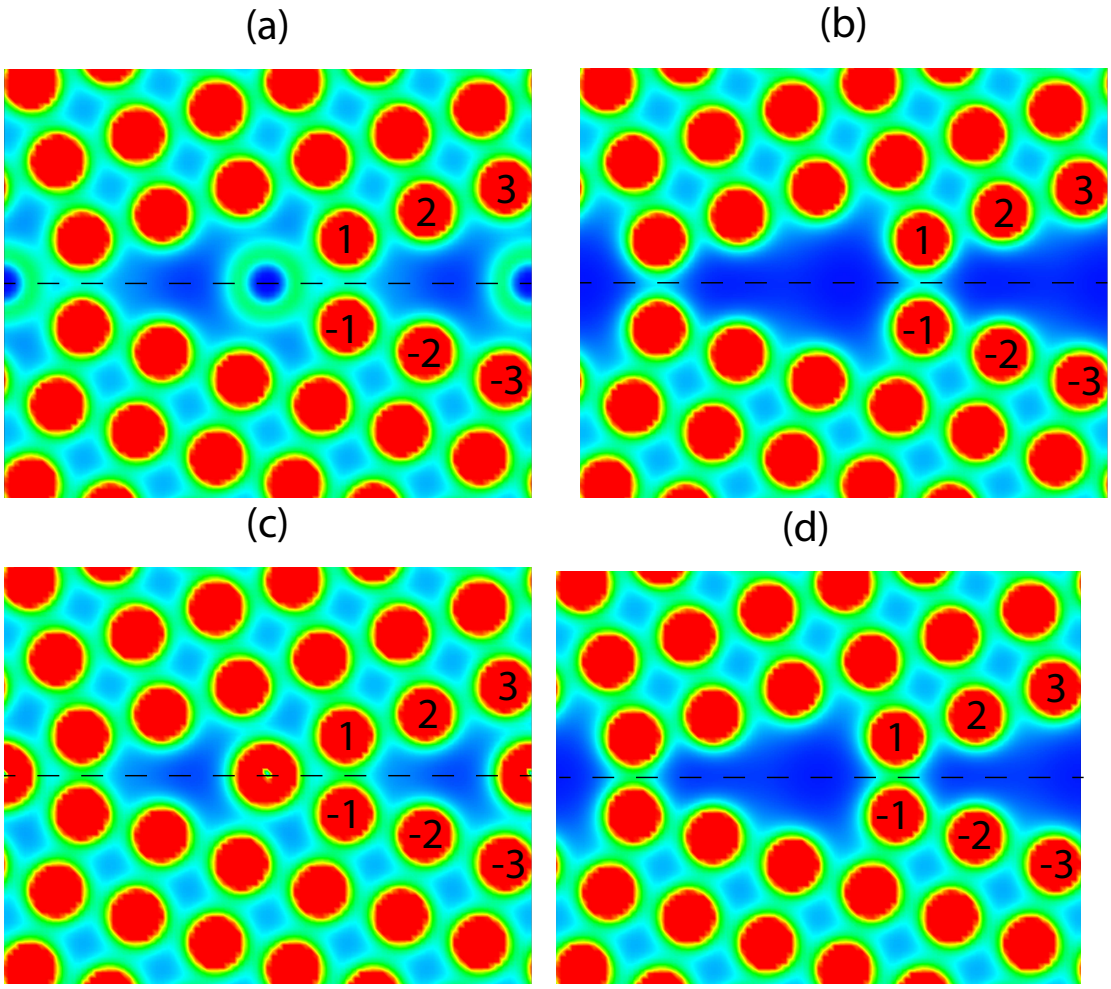

Figure 5.11: Electronic charge density on the (001) plane intersecting the GB for (a) the $\Sigma 5\,(012)$ Cu GB with Pb impurities, (b) the Cu GB structure as for Pb impurities, but with all Pb removed same as structure C in Fig. 5.8, (c) the Cu GB with Ag impurities at the center GB0 plane, (d) the Cu GB structure as for Ag impurities, but with all Ag removed same as structure C in Fig. 5.8. The center GB plane (GB0) is indicated by a dashed black line. Atoms in the first three sets of symmetric planes away from the center GB plane are label $-3, \ldots, 3$. Red areas are regions of large electronic charge density, blue areas are regions of small electronic charge density.

tributions in the form of the CC term become greater and at the same time the substitutional structure contribution becomes less important. The behavior of the CC term for Pb is consistent with our previous results for GBS. The electronic charge densities for Pb are shown in Fig. 5.11(a). Fig. 5.11(b) shows the charge distribution for the structure without Pb atoms at the GB0 plane but with otherwise unchanged structure. In the same way as for Bi, one can see that the decreased electronic charge density across the GB plane is due to the GB expansion and not the chemical character of the Pb impurity atoms.

The behavior of Ag changes more dramatically. Now the CC term becomes dominant, together with the HR term. There are almost no substitutional structure effects. We therefore see very similar behavior for this as for the $\Sigma 5$ (013) Cu GB [108]. However again the substitutional structure contribution is smaller in our case, almost negligible because our GB structure allows for a symmetric addition of the impurities, leading to a more symmetric expansion with less substitutional structure effects. The electronic charge density for the structures with Ag added to the GB and the unrelaxed structure without Ag atoms are shown in Fig. 5.11(c) and (d), respectively. There is a significant similarity to the electronic charge density of the pure Cu GB. Overall, we find that Ag has a strong chemical and compressed impurity contribution, much more than Pb and Bi where pure mechanical effects are more dominant.

system	W_{sep} [J/m^2]	$\gamma^{(\text{b})}$ [J/m^2]	$D = W_{\text{sep}}/\gamma^{(\text{b})}$ [J/m^2]
pure	2.10	0.186	11.3
Ag	1.92	0.699	2.75
Pb	1.30	0.485	2.68
Bi	0.92	0.314	2.93

Table 5.7: Work of separation (W_{sep}), the energy barrier for GBS ($\gamma^{(\text{b})}$) and the corresponding ductility paramter for the pure Cu GB and with Ag, Pb, and Bi impurities.

5.7 Discussion

We have established that GBS is inhibited by Bi, Pb and Ag impurities at the GB. This alone already indicates that we should expect a more brittle behavior for nanocrystalline metals with impurity addition as GBS is an important mechanism of plastic deformation for these. We have seen that of the three impurities Ag has the strongest effect on GBS, followed by Pb and Bi. This is in reverse order for their effect on GB decohesion and hence direct intergranular fracture. It is therefore instructional to calculate the ratio of the sliding energy, $\gamma^{(b)}$, quantifying the resistance to GBS, versus the work of separation, W_{sep}, quantifying the resistance against grain decohesion. This ratio is called the ductility parameter and its significance was previously discussed in detail in section 3 and ref. [112]. This is summarized in Table 5.7. We immediately see that the ductility parameter decreases significantly for all impurities. We first of all see that the initial value of $D = 11.3$ is greater than the critical value identified by Rice [84] for transition from ductile to brittle behavior. Once impurities are added the value of D drops well below the range where the critical value for duc-

tile to brittle behavior is expected to be. The ductility parameter for the clean GB is approximately a factor of 4 greater than those with 1 ML of impurities added to the GB plane. This is particularly interesting for Ag, as it is traditionally considered to have little effect on the mechanical properties of Cu. We hence predict that for nanocrystalline Cu, Ag may have a strong effect, since it removes GBS as a plastic deformation mechanism. The unique behavior of Ag is important for two reasons. First of all, given its strong effect on GBS with at the same time little influence on the intergranular decohesion behavior, it may be an ideal candidate to connect the results from MD calculations on nanocrystalline Cu showing GBS, to experiments for which it is difficult to observe the GBS process directly. Another point is, that since Ag does not affect the intergranular decohesion, it may provide a path to increase the hardness of Cu in the context of the Hall-Petch behavior for nanograined Cu, which is believed to be limited by GBS for small grains.

The effect of Pb and Bi on the resistance against GBS is weaker than for Ag, but in combination with the dramatic decrease of the work of separation when these impurities are added, the ductility parameter decreases to a value very similar to that when Ag impurities are added.

5.8 Conclusion

In this work we studied the $\Sigma 5$ (012) GB in Cu and addressed the physical changes this GB experiences as different impurities are added to the GB. We used a multiscale

method based on coupling a large EAM region to a small DFT region to ensure appropriate coupling of the GB region with the impurities to the bulk. We first investigated the lowest energy positions of the impurities and established that the preferential sites for Bi, Pb and Ag are at the center of the GB, the GB0 plane, and approximately follow the exponential decay behavior expected for impurity segregation near GBs. To assess the mechanical properties of nanocrystalline Cu we consider GBS and how this is affected by adding one ML of either Bi, Pb or Ag. We find that both Bi and Pb inhibit GBS and any GB migration associated with the sliding events. Ag is found to be an even stronger GBS inhibitor than Bi or Pb. This was traced back to the stronger chemical interaction of Ag with Cu. Bi and Pb were found to have an insignificant chemical interaction with Cu and most of the changes in the GBS behavior in comparison to pure Cu could be traced to pure mechanical size effect issues.

We also revisited the issue of intergranular decohesion, a process that can be expected to be of importance for both nanocrystalline and coarse-grained Cu. We use a Gedanken experiment to determine the underlying physical reasons for a decrease of GB cohesion for Bi and Pb for the $\Sigma5\,(012)$ GB and investigate the differences to the behavior seen with Ag inclusion. Similar to the $\Sigma5\,(013)$ GB studied previously [108] the $\Sigma5\,(012)$ here is subject to embrittlement due to a size effect of Bi and Pb, whereas the chemical interactions of Ag with Cu ensure that it does not embrittle the Cu GB by means of a significant decrease in cohesion. It is noteworthy to point out

that the $\Sigma5\,(012)$ GB is found to be more resistant against Bi embrittlement than the $\Sigma5\,(013)$ GB, even though they are both similar $\Sigma5$ GBs and hence expected to behave in a similar manner. This is a direct result of the greater symmetry of the $\Sigma5\,(012)$ GB. This strongly hints at the importance even small differences in the GB character can have in determining the resistance against embrittlement and highlights how computational treatment may allow for identifying GBs particularly suitable for novel applications.

To investigate further that embrittlement of Cu by Bi or Pb is indeed a mechanical size effect instead of an electronic effect where the impurities affect the electronic charge density and may cause a depletion of charge of the Cu-Cu bonds in the neighborhood of the impurities and at the GB interface, we directly study the electronic charge density of the $\Sigma5\,(012)$ Cu GB with and without impurities. Although clear changes in the electronic charge density are observable in the neighborhood of the Bi and Pb impurities, and in particular for the Cu-Cu bonds across the interface, we find strong evidence that this is a direct result of the GB expansion rather than the chemical character of the impurity. This is therefore in direct contrast to any pure electronic effect theories that neglect mechanical effects as underlying reasons for the changes in the electronic charge densities.

Finally, we consider intergranular decohesion and GBS in competition by considering the ductility parameter D. This was used previously to study the change in mechanical behavior for nanocrystalline metals [112]. We find that both Bi and Pb

are expected to strongly embrittle the Cu GB; this is consistent with experiments. For Ag we find an overall decrease in ductile behavior, primarily in the form of removal of GBS as a form of plastic behavior. This is very different from the behavior of Ag in coarse-grained Cu and may enable connecting the MD results for nanocrystalline Cu with experiments. Furthermore, Ag inclusion may enable extending the Hall-Petch relation for nanocrystalline Cu by suppressing GBS. In general, this highlights how different the behavior of metals at the nanoscale can be expected to be and that generalizations based on findings for coarse-grained materials are potentially misleading.

Chapter 6

Influence of vacancies on grain boundary sliding in Copper

6.1 Overview

We study grain boundary sliding in the context of plasticity of a copper grain boundary with and without a mono-vacancy. The vacancy formation energy is determined for positions near a $\Sigma 5\,(012)$ symmetric tilt grain boundary and we find that there are preferential sites in the vicinity of the GB in comparison to the bulk. Grain boundary migration coupled to grain boundary sliding, previously observed for the otherwise defect-free grain boundary, is not stopped by the mono-vacancy near the grain boundary. The energy barrier quantifying resistance against sliding decreases by 0.04 J/m^2, or 22%, for the mono-vacancy, resulting in an increase in the propensity

for plastic deformation accommodated by grain boundary sliding

6.2 Introduction

Grain boundaries (GBs) play a crucial role in the mechanical behavior of metals. It has been known for a long time that grain boundary sliding (GBS) can become of importance for the mechanical properties of polycrystalline metals at elevated temperatures [15, 16, 17]. More recently it has been shown that even at low temperatures GBS can become an important mechanism of plasticity in nanocrystalline (nc) metals [19, 20, 21, 22, 23, 24]. Another important type of defect that is known to affect the physical and mechanical behavior of materials are vacancies. Vacancies are important for the mechanical properties of metals and these have been studied extensively in the past using a variety of experimental techniques [146], classical atomistics [136, 147, 148, 149] and first-principles atomistics methods [125, 134, 135, 150, 151, 152, 153, 154, 155]. The majority of the early first-principles work on vacancies has considered them independent from other defects [150, 151, 152], yet more recently interactions with other defects have become the subject of several studies [134, 135, 153, 154, 155, 155]. In real materials the interaction of different defects can often lead to new types of behavior and interesting effects. In this work we address the collective effect GBs and vacancies may have on the mechanical properties in copper (Cu) by considering the effect of a vacancy on GBS. We have previously addressed the issue of other defects, in the form of impurities in the vicinity of GBs and

how these can affect the GBS properties of a $\Sigma 5\,(012)$ symmetric tilt GB in Cu (section 5). We were able to show that impurities can significantly alter the mechanical behavior by inhibiting GBS.

Vacancies near Cu GBs have been studied in the past [136, 148, 149]. This work was primarily based on the classical embedded atom method (EAM) and tried to address elevated temperature effects using simulated annealing Monte Carlo techniques to study the coupling of GB migration and GBS in combination with vacancies. Ballo *et al.* [136] have gone beyond a purely classical treatment and also addressed the system of a Cu GB with a vacancy using first-principles density functional theory (DFT). Their method neglects force relaxations based on DFT and instead was based on calculations first relaxed purely by the EAM followed by a reduction of the size of the supercell and static calculations using DFT [136]. Other first-principles studies on the collective behavior of GBs and vacancies were performed for Al [135] and Fe [134]. Lu and Kioussis [135] found that vacancies increase the barrier of the energy for GBS in fcc Al of a $\Sigma 5\,(012)$ GB. Zhou *et al.* [134] studied the $\Sigma 5\,(310)$ tilt GB and found the opposite behavior for bcc Fe. Similarly as in the work of Ballo *et al.* [136] the inherently large computational cost of most DFT methods meant that relatively small supercells were employed for both studies, thus resulting in atomic structures of either lines of vacancies or vacancies separated by only very few atomic layers [134, 135, 136]. This may introduce significant error and can only serve as a first approximation to real physical systems with vacancies near GBs. To circumvent this

problem we employ here a multiscale approach coupling a small region treated with DFT to the bulk treated with the EAM. This was described in detail in chapter 4 and applied to the system of a GB with impurities in chapter 5. This allows us to employ large supercells perpendicular to the GB to decouple the vacancy from its periodic images. At the same time we use large supercells parallel to the GB plane, enabling treatment of individual mono-vacancies. Efficiently isolating the vacancy from its periodic images is particularly important in light of work by Gavini *et al.* [125] showing a slow convergence with system size of the formation energy of a mono-vacancy in aluminum.

We find evidence for vacancy segregation near the GB structure, showing that vacancies are preferentially located near the GB in comparison to the bulk Cu, with the lowest energy position one plane away from the center GB. By sliding the grains with a vacancy placed near the GB plane, we show a decrease of the GBS energy with a vacancy, resulting in overall easier GBS. In the context of mechanical properties this hence may lead to an increase in the propensity for plastic deformation as opposed to brittle behavior.

The chapter is organized as follows. Section 6.3 reviews the computational method and the GB structure will be described. This also includes an assessment of the expected error using the multiscale method for vacancy calculations. Section 6.4 contains a discussion of our results for GBS with a vacancy, followed by our conclusions in section 6.5.

6.3 Computational Method

We employ a multiscale method coupling a small region treated with DFT to the bulk metal treated with the EAM. This is implemented using QUICKSTEP [61] as part of the suite of programs CP2K [3]. The specific details of the methodology and implementation were discussed in detail in chapter 4. We use here the same conditions and settings as in chapter 5. The same relaxation procedure and force criterion is also being used. The supercell, described in detail in chapter 4 and 5, takes the form of a structure of 3216 Cu atoms with 201 planes parallel to the GB. On removal of one atom to form a mono-vacancy the structure has 15 Cu atoms remaining in the plane. This means that the vacancy is isolated, with an approximate distance of 14.8 Å to its closest periodic image, allowing for appropriate in-plane relaxation of the vacancy. Unless otherwise stated, 27 layers of atoms perpendicular to the GB plane (14.8 Å $\times$ 16.6 Å $\times$ 21.8 Å) were used for region I within the multiscale approach.

From previous work on GBS involving vacancies, it is known that the energy differences involved in GBS with and without a mono-vacancy can be expected to be small, less than 0.1 J/m^2 [136, 148, 149]. We therefore carefully check the convergence with respect to the DFT cell size in the multiscale approach. To this end we show in Fig. 6.1 (a) and (b) the energy for a fixed and relaxed vacancy, respectively, in a supercell of 3126 atoms with 16 atoms per layer with no other defects as a function of the DFT cell size. The energy difference considered in Fig. 6.1 is the difference between the energy of a perfect fcc structure and the energy of the same structure with

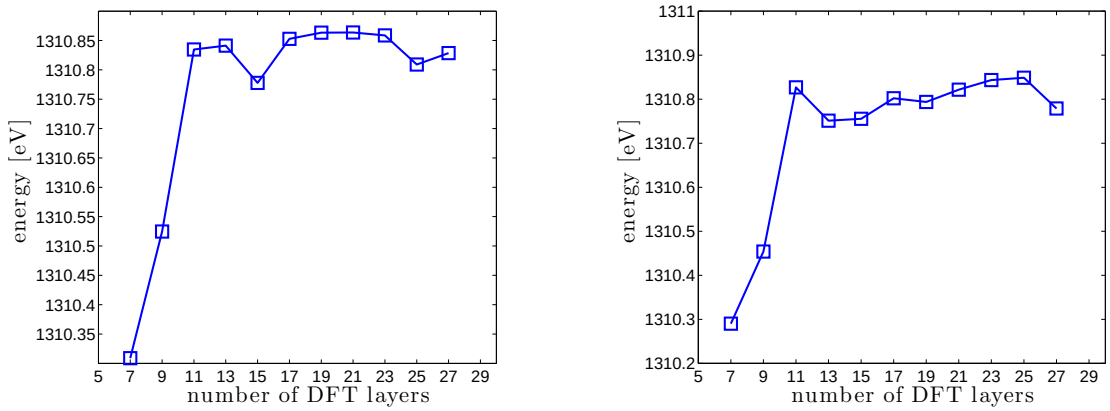

Figure 6.1: Energy difference of the fcc structure of Cu with and without a single vacancy for the multiscale method as a function of the number of DFT layers, where in (a) all atoms are held fixed and (b) all atoms are allowed to fully relax.

a mono-vacancy in the DFT region. We do not include the energy of the removed Cu atom into the energy difference, since this would have to be calculated for each DFT cell size as an approximation. This further complication would not aid in the analysis in the expected error. Our results show that for a fixed or relaxed structure the variation in energy is very similar and, in units particular to the supercell employed here, the energy difference involving a vacancy, for region I sizes greater than 13 layers, has a standard deviation of $\sigma = 0.0025$ J/m^2. This is well below the energy differences for GBS found in section 6.4, and should therefore not influence our final results and conclusions.

6.4 Results and discussion

6.4.1 Vacancy formation energy near the grain boundary

We first consider where the mono-vacancy is preferentially located. To this end we remove a single Cu atom from different positions in the relaxed supercell near the GB. There are 16 atoms per plane, however each one is symmetrically equivalent in the $\Sigma 5\,(012)$ tilt GB. It is therefore sufficient to only consider one vacancy per plane. After removal of the Cu atom the ionic positions are relaxed and we calculate the vacancy energy defined in eq. 4.4. We approximate the energy of a bulk DFT Cu atom by considering the energy of a Cu atom based on a DFT calculation of a fully periodic fcc supercell without defects. The results are shown in Fig. 6.2 as black squares as a function of the layer index away from the center of the GB (where 0 is the center of the GB). Also shown is the bulk vacancy energy based on a DFT calculation using periodic boundary conditions of a $5 \times 5 \times 5$ supercell with a 4 atom basis.

We first note that the vacancy energy for all positions near the GB except the center plane is lower than the bulk vacancy energy. This shows that a mono-vacancy is preferentially located in the vicinity of the GB as opposed to the bulk. This is qualitatively consistent with previous results for Cu based on the classical EAM, however we do not observe the feature of two distinct deep local minima Ballo *et al.* observed in their EAM study of Cu in ref. [149]. Table 6.2 summarizes the vacancy

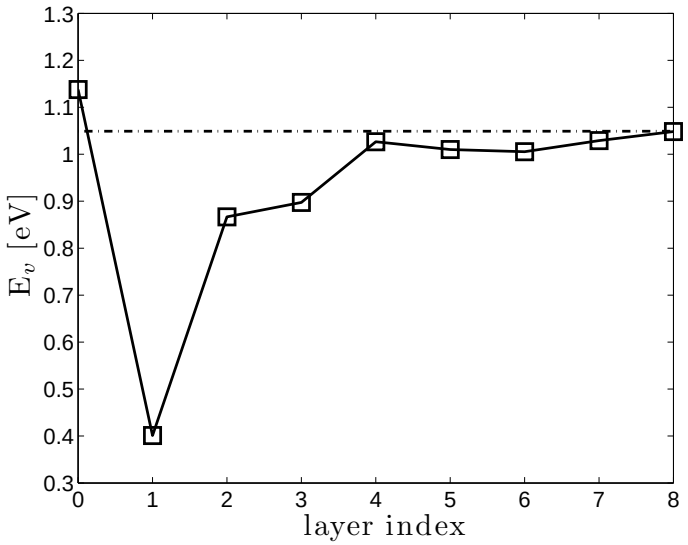

Figure 6.2: Vacancy formation energy for different positions near the GB, where the layer index refers to the layer number away from the center of the GB; the center plane is labeled by the layer index 0, with successive parallel layers away from the center GB plane labeled 1 through 8. Black squares are individual data points based on the multiscale methods; the solid black lines are guides for the eye only. The dash-dotted horizontal line shows the bulk vacancy formation energy.

formation energies for a mono-vacancy on the five nearest layers (GB1 to GB5) to the GB and the center plane (GB0). The table also shows relevant geometric values of the Cu atoms for individual layers. This illustrates that the coordination and average distances of the atoms in the vicinity of the vacancy play an important role and can assist in explaining the behavior seen in Fig. 6.2. Table 6.2 also lists the average relaxation distance of the nearest-neighbor atoms. The lowest vacancy energy position is found to be on layer 1 (GB1). A Cu atom in this layer can be seen to be under-coordinated with only 10 nearest-neighbors, as opposed to 12 nearest-neighbors as expected for the bulk fcc structure. This layer also has the smallest average distance, $\bar{d}$, to the respective nearest-neighbor atoms with $\bar{d} = 2.57$ Å, compared to the bulk value of $d_0 = 2.62$ Å. The geometry of the structure surrounding the mono-vacancy is such that it allows for maximal relaxations of the nearest-neighbor Cu atoms. This explains the low energy position of the vacancy on GB1. A mono-vacancy at the center of the GB has a higher energy than the bulk vacancy energy and also a significantly higher energy than for all other positions near the GB. Cu atoms on the central GB plane (GB0) have a coordination of 12, but the average distances to the nearest-neighbors of $\bar{d} = 2.73$ Å is significantly greater than d_0. On removal of a Cu atom a much greater free volume is therefore created. The geometry around the mono-vacancy on the center GB plane does not allow for any significant relaxation, overall resulting in a very high vacancy formation energy. For atoms beyond two layers away from the GB the average distance to the nearest-neighbors has approximately

	GB0	GB1	GB2	GB3	GB4	GB5
$\bar{d}$ [Å]	2.73	2.57	2.64	2.63	2.62	2.62
coordination	12	10	11	12	12	12
δd [Å]	0.020	0.145	0.075	0.072	0.039	0.041
$E_f^{(\mathrm{v})}$ [eV]	1.14	0.40	0.87	0.90	1.03	1.01

Table 6.1: Vacancy formation energy for different layers near the GB. Also listed are the average distance ($\bar{d}$) to the nearest neighbors, the coordination for Cu atoms of different planes near the GB, and the average relaxation distance of nearest-neighbor atoms (δd). The label convention is such that GB0, GB1, ..., GB5 stands for the center GB plane, one plane from the center plane, ..., five planes from the center plane, respectively.

recovered to the bulk value. These atoms are however still influenced by the geometry of the nearest-neighbors and the long-range strain field of the GB. A mono-vacancy at GB2 or GB3 has nearest-neighbors that allow for significant relaxations, thus giving rise to lower vacancy formation energies. It takes up to 8 layers for the mono-vacancy to recover to a similar value as the bulk energy, but already closely approaches that value at around 4 layers away from the center region. The variations of the vacancy formation energy between layers GB4 to GB8 can be expected due to the long-range strain field of the GB. This influence on the mono-vacancy is not as significant beyond approximately 4 layers, or 3.53 Å away from the center plane of the GB, at least in comparison to the immediate vicinity of the GB. The most stable lowest energy position for the mono-vacancy, one layer away from the center plane of the GB, will be used in the following study on GBS.

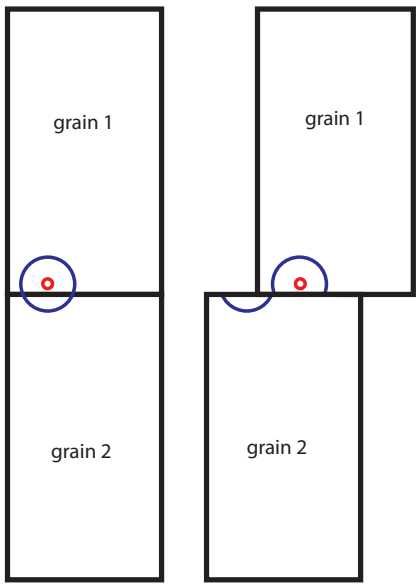

Figure 6.3: Schematic illustration of nearest-neighbor behavior for a single vacancy during slip displacement, where the left-hand and right-hand side show the two grains before and during sliding, respectively. The vacancy is represented by the red circle, surrounded by a perturbation field in blue. During sliding the perturbed atoms surrounding the vacancy would be moved in an unphysical fashion as only a single mono-vacancy is being treated. Atoms in run-on configurations with the mono-vacancy should be allowed to relax.

6.4.2 Grain boundary sliding with a mono-vacancy

We perform GBS quasi-statically by rigidly displacing the two grains of the $\Sigma 5$ (012) symmetric tilt GB against one another. The direction along which slip is performed is the coincidence site lattice (CSL) vector $\langle 012 \rangle$. All atoms except those at the two slip planes are fully relaxed. The relaxation of slip plane atoms has to be considered more carefully in order to properly define the slip vector $\boldsymbol{s}$, but at the same time to not artificially constrain the system. All atoms in the two slip planes are allowed to relax perpendicular to the slip plane. At the same time the relaxations parallel to the slip plane have to be restricted, otherwise the slip vector cannot be defined properly near maxima in the GSF energy landscape. Such maxima appear for run-on configurations where atoms in opposite slip planes are displaced such that they have the same co-ordinates along the $\langle 012 \rangle$ direction, either in the same (001) plane or adjacent $\{001\}$ planes. Not allowing relaxations in the slip plane directions is therefore a necessity to ensure that atoms in such run-on configurations do not relax back to their initial local minima positions, thereby not allowing a clear definition of $\boldsymbol{s}$. Run-on configurations however do not exist for atoms on the opposite side of a vacancy in the slip-plane. It therefore would be unphysical to restrict the in-plane relaxation of atoms that would have a run-on configuration with a vacancy. We therefore allow in-plane relaxations of all nearest-neighbor atoms of the vacancy in the opposite slip plane. This is an important requirement; if not enforced, it was found to give rise to results that would lead to wrong conclusions. The single vacancy causes a perturbation in its vicinity,

which for a vacancy positioned one layer away from the center GB cuts through the slip plane. This is schematically illustrated in Fig. 6.3. Any slip would result in an unphysical displacement of the perturbation. In particular, we find that the vacancy introduces rearrangements of the nearest-neighbor atoms and displaces them by an average of 0.14 Å parallel to the slip plane. Restricting these atoms to these rearranged positions during sliding would give spurious results due to unphysical run-on configurations. We also checked the influence on next nearest-neighbors and found those to be negligible for the GBS results.

We have previously discussed GBS in pure Cu in chapter 5.5.1. It was possible to show that the lower local maximum of the sliding energy at approximately $\boldsymbol{s} = 0.2$ is the most relevant energy barrier to quantify the resistance of the GB against sliding. At $\boldsymbol{s} = 0.4$ GB migration by one layer occurs and results in an equivalent geometry for the vacancy-free structure. The relevant GBS energy for the vacancy-free system is shown in Fig. 6.4 as black circles.

Next, we discuss the results for GBS with a vacancy one layer away from the center plane of the GB. The relevant sliding energies are shown as red diamonds in Fig. 6.4. The overall shape of the energy curve remains similar. A decrease in energy for the two maxima at $\boldsymbol{s} = 0.2$ and 0.7 and an increase in energy for the minimum at $\boldsymbol{s} = 0.4$ occurs. The slip displacement of $\boldsymbol{s} = 0.7$ results in run-on configurations of atoms in the same (001) plane. This is an energetically not preferential pathway for sliding, even with the small decrease due to the introduction

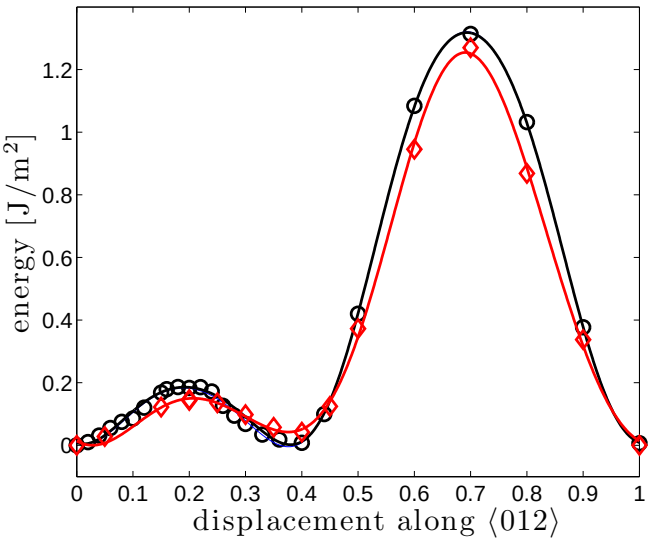

Figure 6.4: Energy for GBS of the $\Sigma 5\,(012)$ symmetric tilt Cu GB along the $\langle 012 \rangle$ direction, with and without a mono-vacancy depicted as red diamonds and black circles, respectively. Lines are Fourier fits.

of the vacancy. The barrier for the energetically preferential sliding pathway remains at a slip displacement along $\langle 012 \rangle$ of $\boldsymbol{s} = 0.2$ as for the defect-free GB. The structure of such a slip displacement is shown in Fig. 6.5(b). The barrier height for the defect-free GB and for the GB structure with a mono-vacancy are shown in Table 6.2 and we can see a decrease in the GSF energy by 0.04 J/m^2 or 22%. Previous first-principles work on GBS in Al, another fcc metal, showed a significant increase of the barrier for GBS by a factor of three [135]. It is not clear whether this is a material dependent property, or the significant difference is a result of employing a larger in-plane supercell and thereby treating an isolated mono-vacancy instead of a line of vacancies. This significant difference for the behavior of GBS with a mono-vacancy warrants further

	defect free GB	GB with vacancy
$\gamma^{\boldsymbol{s}=0.2}$ [J/m^2]	0.186	0.145

Table 6.2: Energy for GBS with a displacement of $\boldsymbol{s} = 0.2$ along $\langle 012 \rangle$ with and without a vacancy at the GB interface.

investigations with larger in-plane supercells for Al in the future.

The energy decrease of the GBS barrier is an order or magnitude greater than the range of energies identified in section 6.4 in the comparison of different supercell sizes. To ensure no error occurred by relaxing the nearest-neighbor atoms of the vacancy, we compare our results of GBS with and without nearest-neighbor relaxations for the defect-free GB. We found a difference of only 0.001 J/m^2, well below the value that has to be resolved. This is a direct result of the large in-plane supercell and the high symmetry of the $\Sigma 5\,(012)$ GB.

Finally, we can consider the changes for a slip vector of $\boldsymbol{s} = 0.4$. This resulted in GB migration for the defect-free GB. We see the same behavior for GBS with a vacancy, only now the energy at $\boldsymbol{s} = 0.4$ increases. This increase is a direct result of the vacancy migrating from a position one layer away from the GB, to the center plane, which is a higher energy position. The GB plane and position of the vacancy are shown in Fig. 6.5(c).

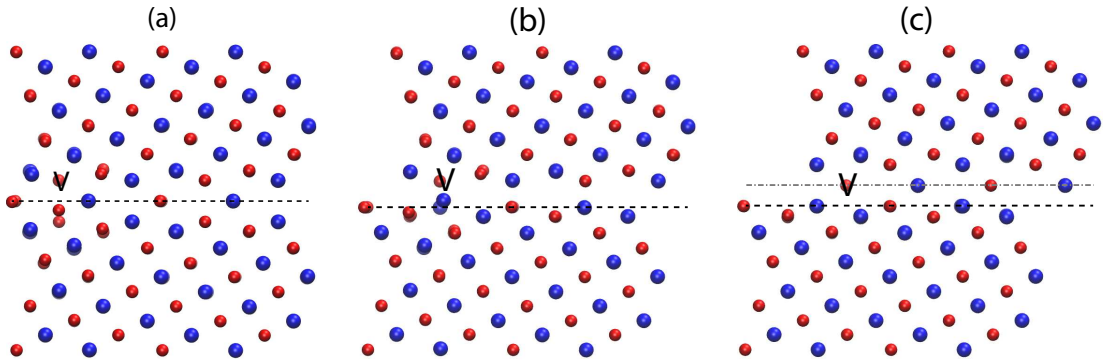

Figure 6.5: Atomic positions for the slip displacements for the Cu $\Sigma 5\,(012)$ GB with a vacancy, where (a) is for $\boldsymbol{s} = 0.0$, (b) for $\boldsymbol{s} = 0.2$ and (c) for $\boldsymbol{s} = 0.4$ along the $\langle 012 \rangle$ direction. Large blue spheres represent Cu atoms on the (001) planes with small red spheres representing Cu atoms on the adjacent (002) plane; all eight layers of $\{001\}$ planes in the supercell are used in generating the illustrations. The original GB plane as for position (a) is indicated by a dashed black line. For a slip displacements of $\boldsymbol{s} = 0.4$ in (c) the migrated GB plane is indicated by a dash-dotted grey line. The position of the mono-vacancy is indicated by the symbol 'V'.

6.5 Conclusion

We have studied GBS of a $\Sigma 5\,(012)$ symmetric tilt GB in Cu with and without a mono-vacancy. We employed a multiscale method and are able to treat large supercells allowing us to effectively isolate the vacancy. This is in contrast to previous first-principles work that was limited to consider small supercells due to the inherent cost of standard DFT approaches [136, 135, 134]. We were able to show that the vicinity of the GB offers energetically preferential positions in comparison to the bulk metal. This shows that we expect mono-vacancies to segregate at the GB. The central GB plane was found to not be energetically beneficial, due to the large free volume created and because the high symmetry of the GB does not allow for any significant

relaxations of the nearest-neighbor atoms. In our study of GBS we have considered a vacancy one layer away from the center GB plane. We found that this vacancy does not stop GB migration or GBS, instead it makes GBS energetically more likely to occur. The relevant energy barrier for sliding was found to decrease by 22%. This implies that a mono-vacancy enhances GBS for the $\Sigma 5\,(012)$ GB in Cu, and hence results in an increase in any associated plastic behavior.

Bibliography

[1] P. Hohenberg and W. Kohn, Phys. Rev. B **136**, 864-867 (1964)

[2] W. Kohn and L. Sham, Phys Rev. A **140**, 1133-1138

[3] http://cp2k.berlios.de/

[4] G. Kresse and J. Furthmüller, Phys. Rev. B **54**, 16, 11169 (1996)

[5] J. M. Soler, E. Artacho, J. D Gale, A. García, J. Junquera, P. Ordejón and D Sánchez-Portal, J. Phys.: Condens. Matter **14** 2745 (2002)

[6] G. Lu and E. Kaxiras, in *Handbook of Theoretical and Computational Nanotechnology*, Vol. X, pp. 1-33, edited by M. Rieth and W. Schommers (American Scientific Publishers, 2005).

[7] D. D. Vvedensky, J. Phys.: Condens. Matter **16**, 50 R1537-R1576 (2004)

[8] G. Makov, C. Gattinoni and A. De Vita, Modelling Simul. Materi. Sci. Eng. **17**, 084008 (2009)

[9] N. M. Ghoniem, E. P. Busso, N. Kioussis and H. Huang, Phil. Mag. **Vol. 83**, Nos. 31-34, 3475-3528 (2003)

[10] J. Q. Broughton, F. F. Abraham, N. Bernstein and E. Kaxiras, Phys. Rev. B **60**, 4, 2391 (1999)

[11] N. Bernstein, J. R. Kermode and G. Csányi, Rep. Prog. Phys. **72**, 026501 (2009)

[12] K. Nomura, Y.-C. Chen, W. Weiqiang, R. K. Kalia, A. Nakano, P. Vashishta and L. H. Yang, J. Phys. D: Appl. Phys. **42**, 214011 (2009)

[13] M. P. Seah, J. Phys. F: Metal Phys. **10**, 1043 (1980).

[14] W. Hampe, Zeitschrift für das Berg-, Hütten- und Salinenwesen in dem Preussischen Staate **22**, 93-138 (1874)

[15] A. P. Sutton and R. W. Balluffi, *Interfaces in Crystalline Materials* (Oxford University Press, Oxford, UK, 1995)

[16] F. R. N. Nabarro and H. L. de Villiers, *The Physics of Creep* (Taylor & Francis, London, 1995)

[17] P. Haasen, *Physical Metallurgy* (Cambridge University, Cambridge, UK, 1986)

[18] H. Gleiter, Prog. Mater. Sci., **33**, pp. 223-315 (1989)

[19] H. Van Swygenhoven and P. M. Derlet, Phys. Rev. B **64** 224105 (2001)

[20] D. Farkas, H. Van Swygenhoven and P. M. Derlet, Phys. Rev. B **66** 060101(R) (2002)

[21] D. V. Bachurin and P. Gumbsch, Acta Mater., **58** 5491 (2010)

[22] K. S. Kumar, H. Van Swygenhoven and S. Suresh, Acta Mater. **51** 5743 (2003)

[23] J. Schiøtz, F. D. Di Tolla and K. W. Jacobsen, Nature, **391** 561 (1998)

[24] J. Schiøtz, T. Vegge, F. D. Di Tolla and K. W. Jacobsen K W, Phys. Rev. B **60** 11 971 (1999)

[25] T. Watanabe, Res. Mech., **11**, 47 1984

[26] V. Randle, Mater. Sci. Tech. Ser., **26** 53 (2010)

[27] M. R. Sørensen, Y. Mishin and A. F. Voter, Phys. Rev B, **62**, 3658 (2000)

[28] J. P. Perdew, K. Burke and M. Ernzerhof, Phys. Rev. Lett. **77**, 3865 (1996)

[29] G. Kresse and D. Joubert, Phys. Rev. B **59** 3 1758 (1999)

[30] S. Goedecker, M. Teter, and J. Hutter, Phys. Rev. B **54**, 1703 (1996)

[31] M. Krack, Theor. Chem. Acc. **114**, 145 (2005)

[32] M. Born and R. Oppenheimer, Ann. der Physik, **389**, Issue 20, pages 457484 (1927)

[33] C. Eckart, Phys. Rev. **46**, 383387 (1934)

[34] D. R. Hartree, Math. Proc. Cambridge, **24**, Issue 1, pp. 89-110 (1928), D. R. Hartree, Math. Proc. Cambridge, **24**, Issue 1, pp. 111-132 (1928), D. R. Hartree, Math. Proc. Cambridge, **24**, Issue 3, pp. 426-437 (1928)

[35] V. Fock, Z. Phys. A-Hadron Nucl., **61**, Numbers 1-2, 126-148 (1930)

[36] J. C. Slater, Phys. Rev. **35**, 210211 (1930)

[37] L. H. Thomas, Math. Proc. Cambridge, **23**, Issue 5, pp 542-548 (1927)

[38] E. Fermi, Z. Phys. A-Hadron Nucl., **48**, Numbers 1-2, 73-79 (1928)

[39] P. A. M. Dirac, Math. Proc. Cambridge, **26**, Issue 3, pp. 376-385 (1930)

[40] J. C. Slater, Phys. Rev. **81**, 385 (1951)

[41] E. Kaxiras, *Atomic and Electronic Structure of Solids* (Cambridge University Press, Cambridge, UK, 2003)

[42] R. M. Martin, *Electronic Structure: Basic Theory and Practical Methods* (Cambridge University Press, Cambridge, UK, 2004)

[43] J. Kohanoff, *Electronic Structure Calculations for Solids and Molecules* (Cambridge University Press, Cambridge, UK, 2006)

[44] R. G. Parr and W. Yang, *Density Functional Theory of Atoms and Molecules* (Oxford University Press, Oxford, UK, 1989)

[45] D. M. Ceperley and B. J. Alder, Phys. Rev. Lett. **45**, 7, 566 (1980)

[46] J. P. Perdew and A. Zunger, Phys. Rev. B **23** 10, 23 (1981)

[47] D. C. Langreth and M. J. Mehl, Phys. Rev. B **28**, 18091834 (1983)

[48] A. D. Becke, Phys. Rev. A **38**, 30983100 (1988)

[49] C. Lee, W. Yang and R. G. Parr, Phys. Rev. B **37**, 785789 (1988)

[50] A. D. Becke, J. Chem. Phys. **84**, 4524 (1986).

[51] J. C. Phillips and L. Kleinman, Phys. Rev. **116**, 287294 (1959)

[52] N. Troullier and Jos Luriaas Martins, Phys. Rev. B 43, 19932006 (1991)

[53] A. M. Rappe, K. M. Rabe, E. Kaxiras and J. D. Joannopoulos, Phys. Rev. B **41**, 12271230 (1990)

[54] C. Hartwigsen, S. Goedecker and J. Hutter, Phys. Rev. B **58**, 3641 (1998)

[55] P. E. Blöchl, Phys. Rev. B, **50**, 17 953 (1994)

[56] J. Ihm, A. Zunger and M. L. Cohen, J. Phys. C: Solid State Phys., **12** 4409 (1979)

[57] S. F. Boys, Proc. R. Soc. Lond. A **200**, 542 (1950)

[58] J. C. Slater, Phys. Rev. **36**, 5764 (1930)

[59] K. Cho, T. A. Arias, J. D. Joannopoulos and P. K. Lam, Phys. Rev. Lett. **71**, 18081811 (1993)

[60] B. Delley, J. Chem. Phys. **92**, 508 (1990)

[61] J. VandeVondele, M. Krack, F. Mohamed, M. Parrinello, T. Chassaing and J. Hutter, Comp. Phys. Comm. **167**, 103 (2005).

[62] G. Lippert, J. Hutter and M. Parrinello, Mol. Phys. **92**, 477 (1997).

[63] M. Krack and M. Parrinello, "*Quickstep: Make the atoms dance*", Forschungszentrum Jülich, NIC Series, Vol. 25, 29 (2004).

[64] M. S. Daw and M. I. Baskes, Phys. Rev. Lett. **50**, 1285 (1983)

[65] M. S. Daw and M. I. Baskes, Phys. Rev. B **29**, 6443 (1984)

[66] P. Mitev, G A Evangelakis and Efthimios Kaxiras, Modelling Simul. Mater. Sci. Eng. **14**, 721731 (2006)

[67] P. Mitev, G A Evangelakis and Efthimios Kaxiras, Modelling Simul. Mater. Sci. Eng. **15**, 691 (2007)

[68] C. Loier and J.-Y. Boos, Metall. Trans. A **12** 1223 (1981)

[69] S. Floreen and J. H. Westbrook, Acta Metall. **17** 1175 (1969)

[70] W. C. Johnson, J. E. Doherty, B. H. Kear and A. F. Giamei, Scr. Metall. **8** 971 (1974)

[71] J. E. Doherty, A. F. Giamei and B. H. Kear, Can Metall. Q. **13** 229 (1974)

[72] M. G. Lozinskiy, G. M. Volkogon and N. Z. Pertsovskiy, Russ. Met. **5** 65 (1967)

[73] S. Kobayashi, S. Tsurekawa, T. Watanabe and G. Palumbo, Scr. Mater. **62** 294 (2010)

[74] D. H. Lassila and H. K. Birnbaum, Acta Metall **35** 1815 (1987)

[75] S. M. Bruemmer, R. H. Jones, M. T. Thomas and D. R. Baer, Metall. Trans. A **14** 223 (1983)

[76] J. K. Heuer, P. R. Okamotoa, N. Q. Lam and J. F. Stubbins, Appl. Phys. Lett. **76** 23 3403 (2000)

[77] H.-P. Chen, R. K. Kalia, E. Kaxiras,G. Lu, A. Nakano, K. Nomura, A. C. T. van Duin, P. Vashishta and Z. Yuan, Phys. Rev. Lett. **104** 155502 (2010)

[78] M. Yamaguchi, M. Shiga and H. Kaburaki, Science **307** 393 (2005)

[79] H. H. Kart, M. Uludogan and T. Cagin, Comp. Mater.Sci. **44** 1236 (2009)

[80] S. Sanyal, U. V. Waghmare, P. R. Subramanian and M. F. X. Gigliotti, Appl. Phys. Lett. **93** 223113 (2008)

[81] R. W. Armstrong, Mater. Sci. Engin. **1** 251 (1966)

[82] A. Kelly, W. R. Tyson and A. H. Cottrell, Phil. Mag. **15** 567 (1967)

[83] J. R. Rice and R. Thomson, Phil. Mag **29** 73 (1974)

[84] J. R. Rice, J. Mech. Phys. Solids **40** 239 (1992)

[85] R. E. Peierls, Proc. Phys. Soc. **52** 34 (1940)

[86] Y. M. Sun, G. E. Beltz and J. R. Rice, Mater. Sci. Engin. A **170** 67 (1993)

[87] E. Kaxiras and M. S. Duesbery, Phys. Rev. Lett. **70** 3752 (1993)

[88] Y. M. Juan and E. Kaxiras, Phil. Mag. A **74** 1367 (1996)

[89] Y. M. Sun and E. Kaxiras, Phil. Mag. A **75** 1117 (1997)

[90] V. V. Bulatov and E. Kaxiras, Phys. Rev. Lett. **78** 4221 (1997)

[91] U. V. Waghmare, E. Kaxiras, V. V. Bulatov and M. S. Duesbery, Modelling Simul. Mater. Sci. Eng. **6** 493 (1998)

[92] U. V. Waghmare, E. Kaxiras and M. S. Duesbery, Phys. Stat. Sol. B **217** 545 (2000)

[93] R. Thomson, Phys. Rev. B. **52** 19 14245 (1995)

[94] V. Vitek, Phil. Mag. **18** 773 (1968)

[95] M. Methfessel and A. T. Paxton, Phys. Rev. B **40** 6 3616 (1989)

[96] H. J. Monkhorst and J. D. Pack, Phys. Rev. B **13** 5188 (1976)

[97] M. J. Mehl and D. A. Papaconstantopoulos, Phys. Rev. B **54** 7 4519 (1996)

[98] G. Lu, D. Orlikowksi, I. Park, O. Politano and E. Kaxiras, Phys. Rev. B **65** 064102 (2002)

[99] R. C. Evans, An Introduction to Crystal Chemistry, (Cambridge University Press, Cambridge, 1964)

[100] Y. Udagawa, M. Yamaguchi, H. Abe, N. Sekimura and T. Fuketa, Acta Mater. **58** 3927 (2010)

[101] J. H. Rose, J. R. Smith, F. Guinea and J. Ferante, Phys. Rev. B **29** 2963 (1984)

[102] J. P. Hirth, *Theory of Dislocations* (John Wiley & Sons, 2nd edition, 1982)

[103] W.R. Warke in ASM Handbook Vol. 11, Failure Analysis and Prevention 861-867, ASM International, Ohio (2002)

[104] A. Joshi and D. F. Stein, J. Inst. Metals **99**, 2635 (1971).

[105] U. Alber, H. Müllehans and M. Rühle, Acta Mater. **47**, 4047 (1999).

[106] J. R. Rice and J.-S. Wang, Mater. Sci. Eng. A **107**, 23 (1989).

[107] R. Schweinfest, A. T. Paxton and M. W. Finnis, Nature **432**, 1008 (2004)

[108] A. Y. Lozovoi, A. T. Paxton and M. W. Finnis, Phys. Rev. B **74**, 155416 (2006)

[109] A. Y. Lozovoi and A. T. Paxton, Phys. Rev. B **77**, 165413 (2008)

[110] G. Duscher, M. F. Chisholm, U. Alber and M. Rühle, Nature **3**, 621 (2004)

[111] W. T. Geng, A. J. Freeman and G. B. Olson, Mater. Trans. **47**, 2113 (2006)

[112] G. Schusteritsch and E. Kaxiras, accepted for publication in Modelling Simul. Materi. Sci. Eng. (2012)

[113] N. Choly, G. Lu, W. E and E. Kaxiras, Phys. Rev. B **71**, 094101 (2005)

[114] B. Zhou and E. A. Carter, J. Chem. Phys. **122**, 184108 (2005)

[115] I. Shin, A. Ramasubramaniam, C. Huang, L. Hung and E. A. Carter, Phil. Mag. **89**, 34 1 (2009)

[116] C. Huang and E. A. Carter, Phys. Rev. B **85**, 045126 (2012)

[117] N. Choly and E. Kaxiras, Solid State Comm. **121**, 281 (2002)

[118] L. Genovesea, T. Deutsch and S. Goedecker, J. Chem. Phys. **127**, 054704 (2007)

[119] L. Genovesea, T. Deutsch, A. Neelov, S. Goedecker and G. Beylkin, J. Chem. Phys. **125**, 074105 (2006)

[120] P. E. Blöchl, J. Chem. Phys. **103**, 7422 (1995); doi: 10.1063/1.470314

[121] Y. Mishin, D. Farkas, M. J. Mehl and D. A. Papaconstantopoulos, Phys. Rev. B **59**, 3393 (1999)

[122] Y. Mishin, M. J. Mehl, D. A. Papaconstantopoulos, A. F. Voter and J. D. Kress, Phys. Rev. B **63**, 224106 (2001)

[123] W. H. Press, S. A. Teukolsky, W. T. Vetterling and B. P. Flannery, *Numerical Recipes. The Art of Scientific Computing* (Cambridge University Press, Cambridge, UK, 3rd Edition 2007)

[124] C. Kittel, *Introduction to Solid State Physics* (John Wiley & Sons, Hoboken, NJ, USA, 1996)

[125] V. Gavini, K. Bhattacharya and M Ortiz, J. Mech. Phys. Solids **55**, 697 (2007)

[126] F. D. Murnaghan, Proc. Natl. Acad. Sci. USA **30**, 244247 (1944)

[127] P. M. Anderson and J. R. Rice, Scr. Metall. **20**, 1467 (1986).

[128] T. D. Kühne, M. Krack, F. R. Mohamed and M. Parrinello, Phys. Rev. Lett. **98**, 066401 (2007)

[129] L. Lu, M. L. Sui and K. Lu, Science **287**, 1463 (2000)

[130] J. Schiøtz and K. W. Jacobsen, Science, **301**, 1357 (2003)

[131] E. O. Hall, Proc. Phys. Soc. **B 64**, 747 (1951)

[132] N. J. Petch, J. Iron Steel Inst. London, **174** , 25 (1953)

[133] G. Schusteritsch, T. D. Kühne, Z. X. Guo and E. Kaxiras, (submitted 2012)

[134] H.-B. Zhou, Y.-L. Liu, C. Duan, S. Jin, Y. Zhang, F. Gao, X. Shu and G.-H. Lu, J. Appl. Phys. **109**, 113512 (2011)

[135] G. Lu and N. Kioussis, Phys. Rev. B **64**, 024101

[136] P. Ballo, J. Degmová and V. Slugeň, Phys. Rev. B **72**, 064118 (2005)

[137] J. VandeVondele and J Hutter, J. Chem. Phys. **127**, 114105 (2007)

[138] W. Losch, Acta Metall **27** 1885 (1979)

[139] R. Haydock, J. Phys. C: Solid State Phys **14**, 3807 (1981)

[140] L. Goodwin, R. J. Needs and V. Heine, Phys Rev Lett **60**, 2050 (1988)

[141] R.P. Messmer and C.L. Briant, Acta Metall. **30** 457 (1982)

[142] M. P. Seah, Proc. R. Soc. Lond. A **349** 535 (1976)

[143] M. P. Seah, Acta Metall. **28**, 955 (1980)

[144] A. P. Sutton and V. Vitek, Acta Metall. **30** 2011 (1982)

[145] J. S. Braithwaite and P. Rez, Acta Mater. **53** 2715 (2005)

[146] P. Ehrhart, P. Jung, H. Schultz and H. Ullmaier, in *Atomic Defects in Metals*, edited by H. Ullmaier, Landolt-Börnstain, New Series, Group II, Vol. 25 (Springer-Verlag, Berlin, 1991)

[147] P. Ballo, N. Kioussis and G. Lu, Phys. Rev. B **64**, 024104 (2001)

[148] P. Ballo and V. Slugeň, Phys. Rev. B, **65**, 012107 (2001)

[149] P. Ballo and V. Slugeň, Comp. Mater. Sci., **33**, 491498 (2005)

[150] P. A. Korzhavyi, I. A. Abrikosov, B. Johansson, A. V. Ruban and H. L. Skriver, Phys. Rev. B **59**, 18 (1999)

[151] T. Korhonen, M. J. Puska and R.M. Nieminen, Phys. Rev. B **51**, 15 (1995)

[152] B. Drittler, M. Weinert, R. Zeller and P. H. Dederichs, Phys. Rev. B **79**, 31 (1991)

[153] G. Lu and E. Kaxiras, Phys. Rev. Lett. 94, 155501 (2005)

[154] G. Lu and E. Kaxiras, Phys. Rev. Lett. **89**, 105501 (2002)

[155] V. Gavini, K. Bhattacharya and M. Ortiz, Phys. Rev. B **76**, 180101 (2007)

[156] M. Finnis, *Interatomic Forces in Condensed Matter* (Oxford University Press, Oxford, UK, 2003)

Appendix A

Calculation of elastic constants

A.1 Method - Elastic Constants

I follow here the notation and method outlined in [156]. It can be shown that for a cubic crystal the only independent elastic constants are C_{11}, C_{12} and C_{44}. The elastic energy per unit volume is given by

$$E_{elastic} = \frac{1}{2}C_{11}\left(\epsilon_1^2 + \epsilon_2^2 + \epsilon_3^2\right) + C_{12}\left(\epsilon_1\epsilon_2 + \epsilon_2\epsilon_3 + \epsilon_3\epsilon_1\right) + C_{44}\left(\epsilon_4^2 + \epsilon_5^2 + \epsilon_6^2\right), \quad \text{(A.1)}$$

where we follow the standard Voigt notation. The procedure for determining the elastic constants for instance for C_{11} is as follows: we apply a strain ϵ_1 to our supercell and determine the total energy per volume as a function of this strain, $E_{tot}\left(\epsilon_1\right)$ in the range of for instance $\pm 2\%$. The volume, V_c, is based on the supercell of no strain. We then fit a fifth order polynomial to the points and determine the curvature at the minimum. We use a higher order polynomoal rather than a simple 2nd order fit, since

it is known that higher order effects can become important for small strains [156]. We use the curvature at the minimum to consistently calculate the elastic constant.

To easily calculate the appropriate strain for each atom in the supercell we introduce here the transformation matrix T in the same manner as in [156]:

$$\epsilon_{\alpha\beta} = \gamma T_{\alpha\beta}, \tag{A.2}$$

where separating γ from the transformation matrix makes it easy to strain the system by a scalar. The original basis $\mathbf{a_i}$ of our supercells is then transformed to the new basis $\mathbf{a_i'}$ such that,

$$\mathbf{a_i'} = \mathbf{a_i} + \gamma \mathbf{T} \mathbf{a_i}. \tag{A.3}$$

The elastic energy per volume from equation A.1 then becomes:

$$E_{elastic} = \frac{1}{2} C_{11} \left(T_{xx} + T_{yy} + T_{zz}\right)^2 \gamma^2 \tag{A.4}$$

$$+ C_{12} \left(T_{xx}T_{yy} + T_{yy}T_{zz} - T_{zz}T_{xx}\right) \gamma^2 \tag{A.5}$$

$$+ 2C_{44} \left(T_{yz}^2 + T_{zx}^2 + T_{xy}^2\right) \gamma^2. \tag{A.6}$$

It is convenient for the discussion below to rewrite this expression in the following form,

$$E_{elastic} = \frac{1}{6} \left(C_{11} + 2C_{12}\right) \left(T_{xx} + T_{yy} + T_{zz}\right)^2 \gamma^2 \tag{A.7}$$

$$+ \frac{1}{3} \left(C_{11} - C_{12}\right) \left(T_{xx}^2 + T_{yy}^2 + T_{zz}^2 - T_{yy}T_{zz} - T_{zz}T_{xx} - T_{xx}T_{yy}\right) \gamma^2 \tag{A.8}$$

$$+ 2C_{44} \left(T_{yz}^2 + T_{zx}^2 + T_{xy}^2\right) \gamma^2. \tag{A.9}$$

The following sections outline the appropriate steps and equations for the 3 different elastic constants for cubic symmetry.

A.1.1 C_{11} for cubic crystal

Determining C_{11} involves straining the supercell by for instance ϵ_{xx}, i.e. setting $T_{xx} = 1$ and $T_{\alpha\beta} = 0$ for all other α, β except $\alpha = \beta = 1$. From equation A.4 we then immediately see that,

$$C_{11} = \frac{\partial^2 E_{elastic}}{\partial \gamma^2} = \frac{1}{V_c} \frac{\partial^2 E_{tot}}{\partial \gamma^2}, \tag{A.10}$$

if we assume that the supercell volume is approximately constant $V_c(\gamma) = V_c$.

A.1.2 C_{12} for cubic crystal

We can calculate C_{12} via the quantity $C' = \frac{1}{2}(C_{11} - C_{12})$, a shear modulus like C_{44}, by using the transformation matrix

$$\mathbf{T}^{C'} = \begin{pmatrix} 1 & 0 & 0 \\ 0 & -0.5 & 0 \\ 0 & 0 & -0.5 \end{pmatrix}, \tag{A.11}$$

which leads to an expression for C' of

$$C' = \frac{1}{3V_c} \frac{\partial^2 E_{tot}}{\partial \gamma^2} \tag{A.12}$$

A.1.3 C_{44} for cubic crystal

We calculate C_{44} for two different transformation matrices. The first involves shearing the system along [111]:

$$\mathbf{T}^{C_{44}} = \begin{pmatrix} 0 & 0.5 & 0.5 \\ 0.5 & 0 & 0.5 \\ 0.5 & 0.5 & 0 \end{pmatrix}, \tag{A.13}$$

with and expression for C_{44},

$$C_{44} = \frac{1}{3V_c}\frac{\partial^2 E_{tot}}{\partial \gamma^2}. \tag{A.14}$$

An alternative transformation consists of a shear along a (001) plane:

$$\mathbf{T}^{C_{44}} = \begin{pmatrix} 0 & 1 & 0 \\ 1 & 0 & 0 \\ 0 & 0 & 0 \end{pmatrix}. \tag{A.15}$$

The relevant expression to calculate C_{44} then is given by,

$$C_{44} = \frac{1}{4V_c}\frac{\partial^2 E_{tot}}{\partial \gamma^2}. \tag{A.16}$$